FZD-493

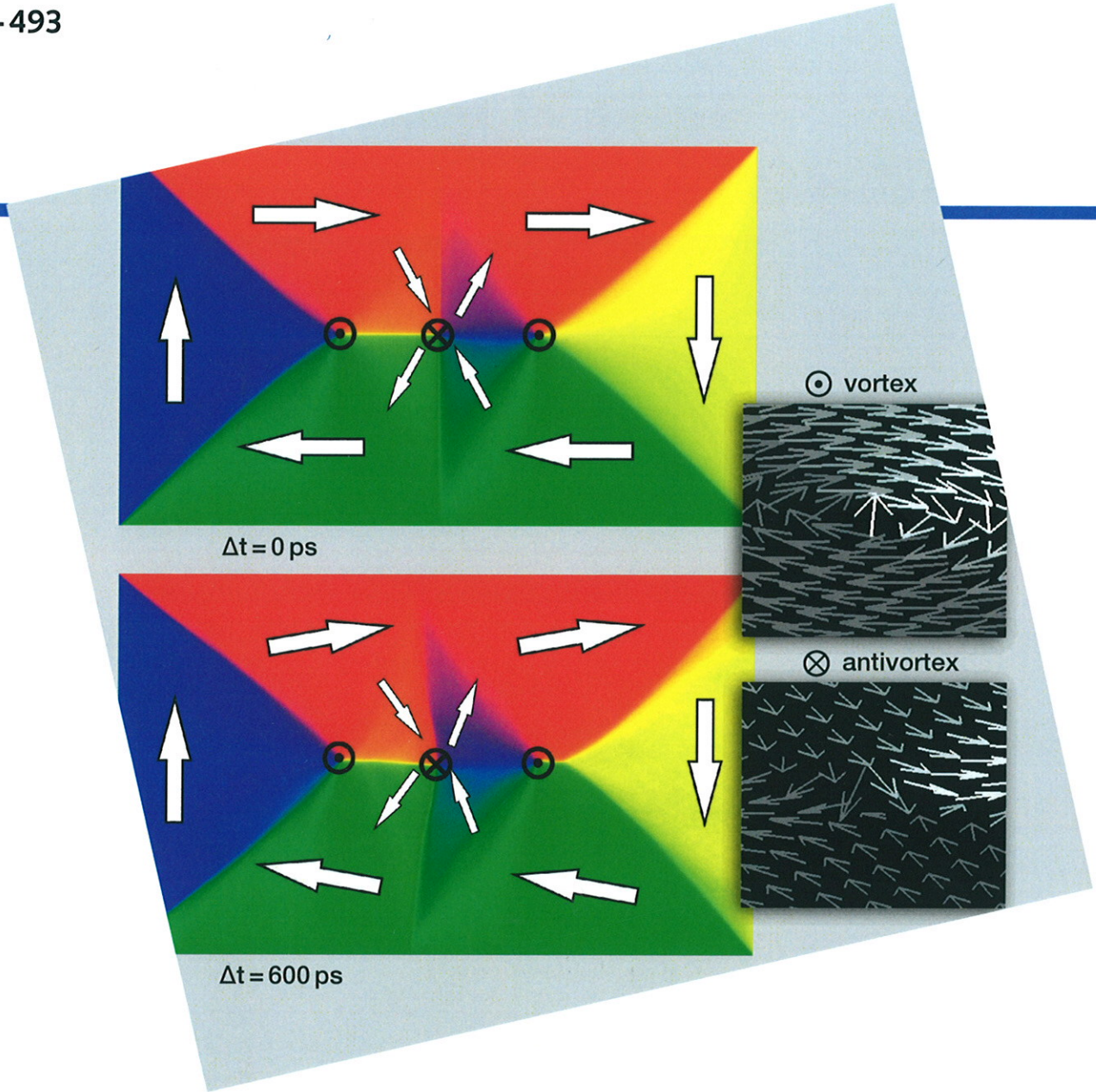

Wissenschaftlich-Technische Berichte
FZD-493 2008 · ISSN 1437-322X

ANNUAL REPORT 2007

INSTITUTE OF ION BEAM PHYSICS AND MATERIALS RESEARCH

Forschungszentrum
Dresden Rossendorf

Wissenschaftlich-Technische Berichte
FZD – 493
2008

Annual Report 2007

Institute of Ion Beam Physics and Materials Research

Editors:

J. von Borany, V. Heera,
M. Helm, W. Möller

Forschungszentrum Dresden Rossendorf

Cover Picture:

The top coloured image shows a magnetic domain configuration of a rectangular ferromagnetic platelet (5 µm × 3 µm × 20 nm) exhibiting a single cross-tie wall. This cross-tie wall consists of two clockwise magnetization curls indicated by the arrows. The centre of each magnetization curl exhibits a vortex core with the magnetization pointing either upwards or downwards (see sketches at the right). In the example shown here both vortex cores point upwards. In the centre of the structure an antivortex is located. Also here a singularity in magnetization (pointing upwards/downwards) is obtained. Although only a few nanometer in size these singularities govern the overall magnetization dynamics of the whole element.

The bottom coloured image shows the magnetization configuration after excitation by a pulsed magnetic field (20 Oe, 500 ps) after 600 ps. As a result in the upper and lower domains the magnetization is tilted upwards and the vertical domain wall in the centre is bended to the right. After several nanoseconds the domain, domain wall and vortex excitations are decayed and the equilibrium state (upper image) is re-established.

The micromagnetic simulations shown here are used to interpret the magnetization dynamics in thin magnetic films fields which has been studied by time-resolved photoelectron microscopy using Synchrotron radiation at the Swiss Light Source.

For detail see the contribution of K. Küpper at al.; pp. 20 – 23.

Forschungszentrum Dresden - Rossendorf e.V.
Institut für Ionenstrahlphysik und Materialforschung
Postfach 51 01 19
D-01314 Dresden
Bundesrepublik Deutschland

Direktoren	Prof. Dr. Manfred Helm	Prof. Dr. Wolfhard Möller
Telefon	+ 49 (351) 260 2260	+ 49 (351) 260 2245
Telefax	+ 49 (351) 260 3285	+ 49 (351) 260 3285
E-mail	m.helm@fzd.de	w.moeller@fzd.de
Homepage	http://www.fzd.de/FWI	

Preface by the Directors

The "Structure of Matter" program activities of Forschungszentrum Dresden-Rossendorf (FZD) are to a large fraction delivered by the Institute of Ion Beam Physics and Materials Research (IIM) in the fields of semiconductor physics and materials research using ion beams. The institute operates a national and international Ion Beam Center (IBC), which, in addition to its own scientific activities, makes available fast ion technologies to universities, other research institutes, and industry. Parts of its activities are also dedicated to exploit the infrared/THz free-electron laser at the 40 MeV superconducting electron accelerator ELBE for condensed matter research. For both facilities the institute holds EU grants for funding access of external users. Cooperation with colleagues from the High Magnetic Field Laboratory Dresden (HLD), another institute of the FZD, is increasing as well.

In 2007, the process of staff rejuvenation upon retirements continued at the institute. A new research group dealing with magnetic semiconductors was established under the leadership of Dr. Heidemarie Schmidt as a young scientist. A substantial increase in particular of the number of young scientists and students resulted in a total IIM staff of more than 150 at the end of 2007.

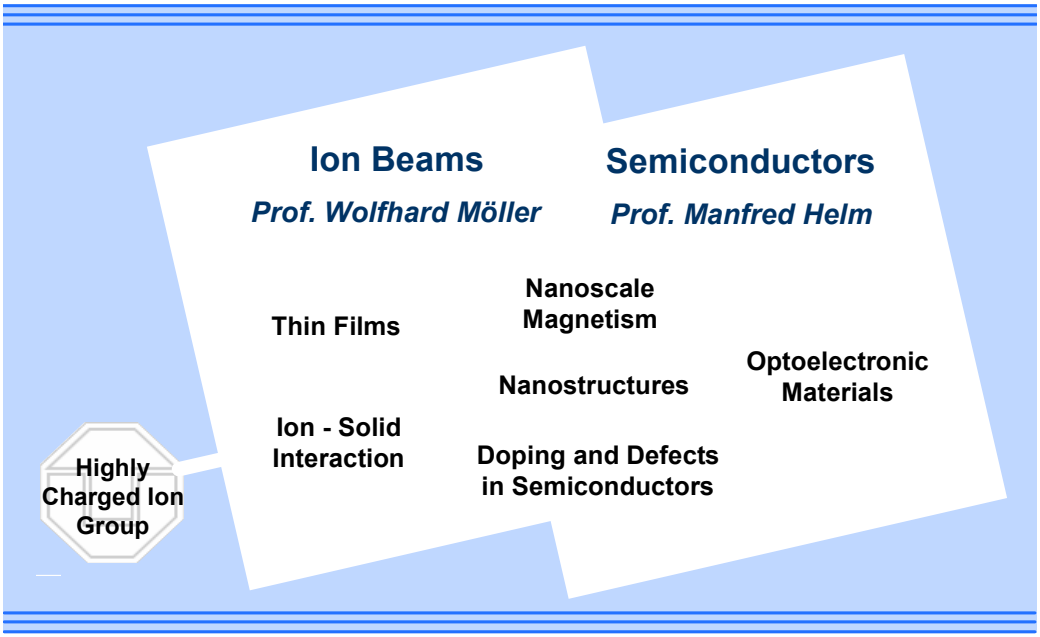

The diagram displays the presently six R&D topics of the institute, together with the associated Highly Charged Ion (HCI) Group of the TU Dresden. Our research activities span a wide range of topics relevant for future information processing and energy technology, be it in the realm of nanoelectronics, optoelectronics, magnetoelectronics, spintronics and solar technology. Highlights of last year's research are presented in this Annual Report through reprints of short papers that were published in leading international journals. IIM staff published more than 150 papers in peer-reviewed journals in 2007, thereof about 40 contributions to high-impact journals (impact factor larger > 3). The scientific achievements of IIM have also been honored internally at FZD, by awarding the 2007 Research and PhD Student Prizes to Dr. Karsten Küpper and Dr. Dominik Stehr, respectively.

We are also pleased that we can report on a stable level of third-party funding, in spite of the ever-tougher competition. In particular, funding the by German Science Foundation (DFG) has taken another steep increase. Here we would especially like to mention the participation of several IIM scientists in a National Research Group "Self-Organized Nanostructures by Low-Energy Ion-Beam Erosion" funded by DFG. A good part of funding comes through contracts with industrial companies,

including also local microelectronics and other high-tech industry. Thus also our funding spectrum reflects our scope from more basic to more applied research.

Recalling the events of the year, IIM contributed essentially to the FZD Open Laboratory Day on May 12, which focused on materials research, and to the Dresden Long Night of Science on June 29. Quite an effort went into the preparation of the evaluation of FZD by the German Wissenschaftsrat (Science Council) which took place at the end of November. There are no official statements available so far, but we are quite optimistic about the outcome. IIM organized the 4th Int. Workshop on High-Resolution Depth Profiling Using Ion Beams at Radebeul near Dresden, acted as co-organizer of the 9th Int. Workshop on Plasma Based Ion Implantation and Deposition at Leipzig/Germany and the 15th Int. Summer School on Vacuum, Electron and Ion Technologies at Sozopol/Bulgaria.

We sincerely thank all partners, friends, and organizations who supported our progress in 2007. Special thanks are due to the Executive Board of the Forschungszentrum Dresden-Rossendorf, the Minister of Science and Arts of the Free State of Saxony, and the Minister of Education and Research of the Federal Government of Germany. Numerous partners from universities, industry and research institutes all around the world contributed essentially, and play a crucial role for the further development of the institute. Last but not least, the directors would like to thank all IIM staff for their efforts and excellent contributions in 2007.

Prof. Wolfhard Möller

Prof. Manfred Helm

Contents

Selected Publications

Statistics

Selected Publications

Copyright Remarks

The following journal articles are reprinted with kind permission from

D. Kost, S. Facsko, W. Möller, R. Hellhammer, and N. Stolterfoht
Physical Review Letters, Vol. **98**, Issue 22, Art.No. 225 503, 2007

D. Güttler, R. Grötzschel, and W. Möller
Applied Physics Letters, Vol. **90**, Issue 26, Art.No. 263 502, 2007

B. Abendroth, H.-U. Jäger, W. Möller, and M. Bilek
Applied Physics Letters, Vol. **90**, Issue 18, Art.No. 181 910, 2007

K. Küpper, M. Buess, J. Raabe, C. Quitmann, and J. Fassbender
Physical Review Letters, Vol. **99**, Issue 16, Art.No. 167 202, 2007

M. O. Liedke, B. Liedke, A. Keller, B. Hillebrands, A. Mücklich,
S. Facsko, and J. Fassbender
Physical Review B, Vol. **75**, Issue 22, Art.No. 220 407(R), 2007

K. Potzger, S. Zhou, H. Reuther, K. Küpper, G. Talut, M. Helm,
J. Fassbender, and J. D. Denlinger
Applied Physics Letters, Vol. **91**, Issue 6, Art.No. 062 107, 2007

L. Röntzsch, K.-H. Heinig, J. A. Schuller, and M. L. Brongersma
Applied Physics Letters, Vol. **90**, Issue 4, Art.No. 044 105, 2007

S. Prucnal, J. M. Sun, W. Skorupa, and M. Helm
Applied Physics Letters, Vol. **90**, Issue 18, Art.No. 181 121, 2007

H. Schmidt, M. Wiebe, B. Dittes, and M. Grundmann
Applied Physics Letters, Vol. **91**, Issue 23, Art.No. 232 110, 2007

F. Peter, S. Winnerl, S. Nitsche, A. Dreyhaupt, H. Schneider, and M. Helm
Applied Physics Letters, Vol. **91**, Issue 8, Art.No. 081 109, 2007

H. Schneider, T. Maier, M. Walther, and H. C. Liu
Applied Physics Letters, Vol. **91**, Issue 19, Art.No. 191 116, 2007

C. Villas-Boas Grimm, M. Priegnitz, S. Winnerl, H. Schneider, M. Helm,
K. Biermann, and H. Künzel
Applied Physics Letters, Vol. **91**, Issue 19, Art.No. 191 121, 2007

PRL 98, 225503 (2007) PHYSICAL REVIEW LETTERS week ending 1 JUNE 2007

Channels of Potential Energy Dissipation during Multiply Charged Argon-Ion Bombardment of Copper

D. Kost, S. Facsko, and W. Möller*

Institute of Ion Beam Physics and Materials Research, Forschungszentrum Dresden-Rossendorf, 01314 Dresden, Germany

R. Hellhammer and N. Stolterfoht

Division of Structure Research, Hahn-Meitner Institute, 14109 Berlin, Germany

(Received 8 January 2007; published 1 June 2007)

The dissipation of potential energy of multiply charged Ar ions incident on Cu has been studied by complementary electron spectroscopy and calorimetry at charge states between 2 and 10 and kinetic energies between 100 eV and 1 keV. The emitted and deposited fractions of potential energy increase at increasing charge state, showing a significant jump for charge states $q > 8$ due to the presence of L-shell vacancies in the ion. Both fractions balance the total potential energy, thus rendering former hypotheses of a significant deficit of potential energy obsolete. The experimental data are reproduced by computer simulations based on the extended dynamic classical-over-the-barrier model.

DOI: 10.1103/PhysRevLett.98.225503 PACS numbers: 61.80.Jh, 41.75.Ak, 52.50.Gj, 79.20.Rf

In 1983, Datz stated [1] that ''our community is almost certainly on the verge of discovering new phenomena that occur in multiply charged ion (MCI) interaction with solids.'' Since then, research is continuously verifying this statement by demonstrating not only new aspects of atomic physics which occur during the approach of an MCI to a solid surface, but also characteristic new effects of ion-solid interaction (for reviews, see Refs. [2–4]). The latter include enhanced secondary-electron emission, enhanced sputtering, and desorption of adatoms, pointing to promising prospects of MCI applications in materials science. These include surface analysis, the synthesis of materials with new properties [5,6], and the formation of nanotopographical structures on surfaces [4,7]. The effects are related to the potential energy of the MCI (the sum of the binding energies of the removed electrons), which may exceed the kinetic energy of the ion significantly at sufficiently low velocity. During MCI interaction with a solid surface, the potential energy is released in connection with the neutralization of the ion. According to the classical-over-the-barrier model [8], the interaction process may start already a few tenths of a nanometer in front of the surface, being associated with the transfer of a large number of electrons. Emission of Auger electrons from the resulting hollow atom or during its subsequent collisional interaction with the top surface [8–10] may reemit a significant fraction of the initial potential energy into the vacuum. However, this fraction plus the energy carried away by x rays and secondary atoms and ions was found to amount to less than about 10% of the initial potential energy ([11] and references therein). Thus, a substantial fraction will remain in the bulk of the substrate, which is simultaneously a prerequisite for significant effects of potential energy surface modifications.

To the best of our knowledge, only two earlier publications described measurements of this retained fraction of the potential energy. Schenkel *et al.* [11] employed a silicon detector to determine the charge transported by Auger electrons into the depletion layer as well as the charge created there by UV photons and x rays. Their result of 35%–40% of retained potential energy for highly charged Xe and Au ions represents a lower estimate as a significant fraction might be deposited in the 50 nm insensitive surface layer of their detector. Alternatively, Kentsch *et al.* [12] used a calorimetric setup to measure the retained potential energy for Ar ions incident on copper. Again, a retained fraction of 30%–40% was found, which, in comparison to Ref. [11], was considered to be fortuitous but to corroborate the conclusion that a significant fraction of the potential energy dissipates into unknown channels. Therefore, it was the aim of the present study to remeasure electron emission and calorimetric data under improved experimental conditions using the identical system of Ar^{q+} incident on copper. As we will show below, electron emission and thermalization in the solid represent the dominant channels of dissipation of potential energy. The findings are consistent with a full detection of the potential energy, thus resolving the former puzzle of unknown dissipation channels.

The electron emission experiments were performed in a UHV vacuum chamber attached to the 14.5 GHz electron cyclotron resonance (ECR) source at Hahn-Meitner Institute. The base vacuum was well in the 10^{-10} mbar range. Prior to the measurements, the polycrystalline copper samples were sputter cleaned by 3 keV Ar^+ bombardment. During the subsequent measurements of electron emission, no traces of any C or O contaminants were visible in the energy spectra. Using a deceleration lens system, the measurements were performed at fixed kinetic ion energy of 720 eV for all charge states. The available charge states were limited to $q < 10$, as the $^{40}Ar^{10+}$ beam was contaminated by ions of equal mass to charge ratio

(e.g., $^{16}O^{4+}$). To evaluate the amount of the emitted secondary-electron energy, double differential electron spectroscopy was employed yielding the number of electrons $d^2N/dEd\Omega$ per interval of electron energy E and emission angle Θ with respect to the surface normal. The data were fitted using the function [10,13]

$$\frac{d^2N}{dEd\Omega}(E, \Theta) = A(E) + B(E)\cos(\Theta), \qquad (1)$$

where the fit parameters A and B were found to be essentially independent of the emission angle. The total number of electrons emitted per energy interval dN/dE is then obtained by integrating Eq. (1) over the backward 2π solid angle. Figure 1 shows the integrated electron energy spectra for different charge states of the projectiles. In addition to a pronounced low-energy fraction, a characteristic peak structure around 200 eV appears for the highest charge states. This is attributed to LMM–Auger-electron transitions, which arise for Ar^{9+} and metastable Ar^{8+} due to a vacancy in the L shell.

The total emitted energy is calculated according to

$$E^{\mathrm{em}} = \int_E E\frac{dN}{dE}dE. \qquad (2)$$

The result is shown in Fig. 2. There is a clear increase of the emitted energy at increasing charge state q of the projectile. For $q = 2$, the total amount of emitted energy is very small, which indicates that kinetic electron emission can be neglected under the present experimental conditions.

For the calorimetric measurement of the deposited potential energy, the setup at Forschungszentrum Dresden-Rossendorf [12] was considerably improved. A UHV chamber with a base pressure of $(2–3) \times 10^{-10}$ mbar, equipped with a device for vacuum sample transfer, was connected to a 14.5 GHz ECR source with a similar beam deceleration system as described above. By installing proper thermal radiation shields, the drift caused by variations of the environmental temperature was largely suppressed. During former studies [12], the ion current was measured in a separate Faraday cup with secondary-electron suppression, which might have led to errors due to the influence of the suppressor voltage on the trajectories of the low-energy ions. This procedure also required very high beam stability during the measurements. Therefore, in the present study the ion current was measured simultaneously with the calorimetric measurements. No voltage was applied to the target, while measuring the secondary-electron current at a surrounding metallic shield.

As in the former setup, the calorimeter was calibrated using an electrical reference heater. After a target cleaning procedure, as described above for the electron emission measurements, the calorimetric runs were performed at kinetic energies varying from 100 to 1000 eV for each charge state. As described in Ref. [12], the deposited fraction of the potential energy is obtained by extrapolation to zero kinetic impact energy. The results are shown in Fig. 2 for charge states ranging from 2 to 10. It should be noted that the reproducibility of the measurement (see the repeated runs at $q = 4$ and $q = 6$) is much better than the spread indicated by the error bars, which include systematic experimental errors.

Also included in Fig. 2 are the total potential energies associated with the different charge states, which have been obtained by summing over the ionization energies resulting from atomic structure codes [14,15]. Their trend of a strong increase with increasing charge state is repro-

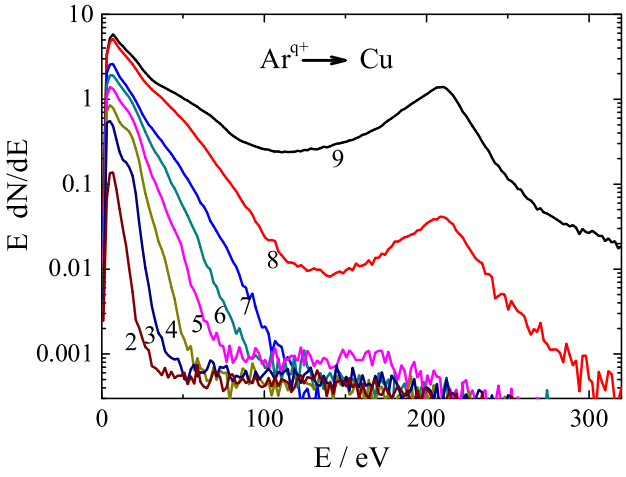

FIG. 1 (color online). Energy dispersive emitted amount of kinetic energy of secondary electrons for different charge states of argon ions impinging on a copper surface. The kinetic energy of the ions was fixed to 720 eV for all charge states.

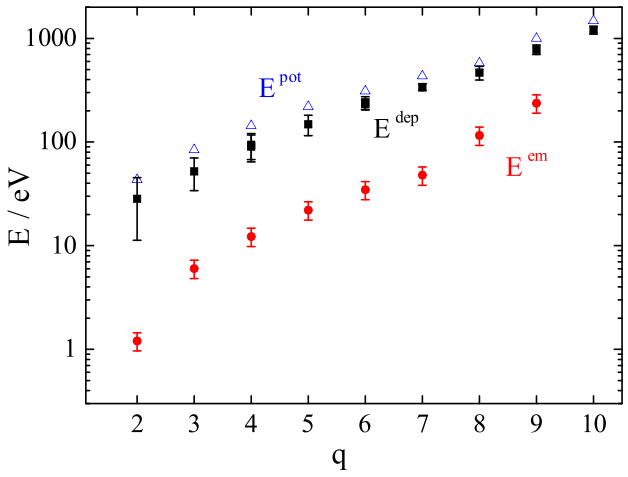

FIG. 2 (color online). Total amount of emitted electron energy E^{em} (circles) and potential energy deposited in the bulk E^{dep} (squares) per incident ion versus the charge state q of the incident argon ions. The data are compared to the potential energies E^{pot} as obtained from atomic structure codes [14,15] (open triangles).

duced by both the reemitted and the deposited fractions at a high degree of qualitative similarity. In Fig. 3, the data are replotted as fractions of the total potential energy of the projectiles. Within the experimental errors which are significant, in particular, for the low charge states, the deposited fraction is nearly constant at $(80 \pm 10)\%$. This is about twice the value of Kentsch *et al.* [12], which we mainly attribute to the improved procedure of ion current measurement. The emitted fraction amounts to $(10 \pm 5)\%$ in rough agreement with former findings [11], with a tendency of an increase at increasing charge state. The latter becomes apparent especially for charge states higher than $q = 7$ due to the onset of LMM–Auger-electron emission as described above. For the lowest charge states, the emitted fraction is somewhat underestimated, since the corresponding spectra are dominated by low-energy electrons, which are affected by a loss of detector efficiency (see Fig. 1). However, this error is small as it can be demonstrated by extrapolating the electron energy distributions towards zero energy. The sum of the results of the two complementary measurements yields a relative amount of potential energy of $(90 \pm 11)\%$ which fulfils the potential energy balance within the experimental errors. This finding is in agreement with expectation. For the present projectiles with a nuclear charge of $Z = 18$ and a highest charge state of $q = 10$, x-ray emission during the relaxation processes can be neglected, being lower by about 2 orders of magnitudes as compared to the Auger-electron yield [16–19]. Moreover, potential emission of atoms has not been

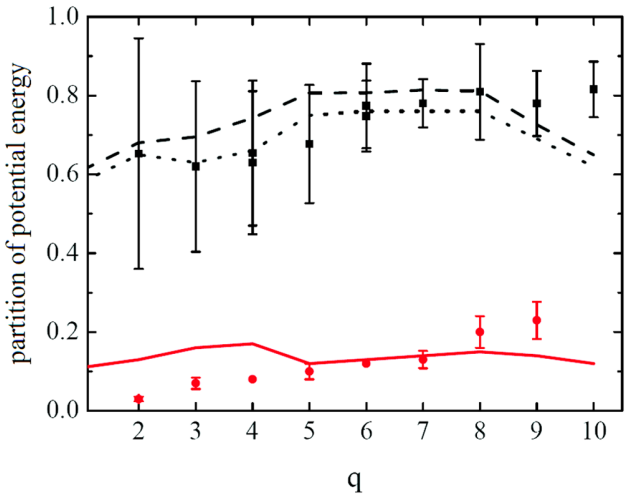

FIG. 3 (color online). Fractions of the potential energy dissipated into electron emission (circles, solid line) and deposited in the surface (squares, dashed line) versus charge state q. The symbols denote the experimental data. The lines have been obtained from numerical simulations using the extended dynamic classical-over-the-barrier model at a kinetic ion energy of 720 eV, as described in the text. The dotted line denotes the deposited fraction with the contribution from image charge acceleration being neglected.

observed for metals. Thus, the essential energy dissipation channels are secondary-electron emission and the deposition of potential energy in the subsurface atomic layers.

For corresponding calculations of the conversion of the potential energy into the dissipation channels, numerical computer simulations based on the extended dynamical classical-over-the-barrier model [8,20,21] were performed. The original simulations were mainly developed to model the relaxation of hollow atoms above the surface, whereas corresponding subsurface studies are limited [22]. Here, we extended the concepts of Refs. [20,21] for electron transfer dynamics to the subsurface regions. In brief, the processes of resonant capture and loss are switched off after crossing the jellium edge of the surface, so that the electron transfer dynamics are governed by peeloff and sidefeeding. Ion stopping in the bulk was implemented. At the instant of each Auger-electron emission the kinetic energy of the electron and the position of the ion are stored. If the ion is positioned above the surface, it is assumed that 50% of the electrons are ejected each toward the surface and away from the surface. If the electron emission takes place below the surface, we at first share the number of electrons again equally. The half that moves in the forward direction deposits all its kinetic energy in the solid. The second half, which is traveling towards the surface, is subject to electron attenuation with a probability $K(E_0, x_i)$ depending on the initial kinetic energy E_0 and the emission depth x_i of the electrons [23]. From these numbers of electrons, the fractions of energy which are deposited in the bulk or emitted into the vacuum are obtained by multiplying with the corresponding initial energies.

During the calculations, the image charge acceleration of the MCI in front of the surface is also evaluated, which, due to the low velocity of the ions, is nearly completely deposited into nuclear stopping. Thus, by means of the simulations, the fractions of potential energy deposited into the electronic and the nuclear system of the solid can be separated. The simulation results confirm that the energy required for the image charge acceleration is balanced by a shift of the atomic levels of the ion approaching the surface, i.e., fed by the potential energy of the MCI. For the present system, the image potential energy gain fraction amounts to about 5% of the total potential energy. This energy gain also contributes to the calorimetric measurement of the deposited fraction of the potential energy.

The results of the numerical calculations are given by the lines in Fig. 3. With respect to the experimental error bars, the potential energy dissipation does not significantly depend on the kinetic energy in the range of the experiments, so that the results at 720 eV are taken as being representative. Despite the simplicity of the model, a surprisingly good agreement is found between the calculated and experimental data. The calculated emitted fraction is in good quantitative agreement with the experiments in aver-

age, but is almost independent of the charge state in contrast to the experimental trend. For the deposited fraction, there is a significant deviation only at the highest charge states. The model calculations treat the influence of the image charge potential on the atomic levels of the ions as a perturbation. For L-shell vacancies, the ion neutralization in front of the surface is reduced due to frequent autoionization processes, so that the ion survives longer when approaching the surface. This leads to an increase of the perturbation and a correspondingly reduced energy of the released electrons. As the screening by outer electrons is neglected, this high perturbation might be partly artificial and result in a reduced calculated fraction of the released potential energy.

Both in experiment and from calculation, the deposited and emitted fractions do not fully add to the nominal potential energy of the ions. The latter is given relative to the vacuum level, whereas during ion-solid interaction electrons are transferred to the ion from the Fermi level of the solid, which corresponds to the consumption of the work function per transferred electron. With the work function of Cu of 4.4 eV, this energy consumption ranges from about 10 to 40 eV for the present charge states. At the charge states of 6 and 7, where the experimental errors are relatively small and the agreement between model calculations and experiments is best (see Fig. 3), the resulting relative energy deficit is about 8% in good agreement with the data of Fig. 3. This, however, might be fortuitous in view of the experimental errors and the simplicity of the model.

Summarizing, we conclude that the potential energy of the MCI is released by emission of a specific number of Auger electrons along the ion trajectory, which either are emitted into the vacuum or deposit their kinetic energy in the solid, depending on the MCI position at emission time and the energy of the Auger-electron transition. For the first time, it is demonstrated that the fraction of the potential energy of multiply charged ions which is released by Auger electrons, and the fraction which is deposited into the target, balance with the total potential energy at different charge states. For argon ions incident on copper with charge states up to 10, the deposited fraction is almost independent of the charge state. The results of computer simulations based on the extended dynamic classical-over-the-barrier model are in good agreement with the experimental data, thus corroborating the picture that the potential energy is essentially transferred via Auger electrons, which are either emitted into the vacuum or deposited into the bulk.

*Corresponding author.
Email address: w.moeller@fzd.de
Fax: +49-351-260 3285

[1] S. Datz, Phys. Scr. **T3**, 79 (1983).
[2] A. Arnau *et al.*, Surf. Sci. **27**, 113 (1997).
[3] J. D. Gillaspy, J. Phys. B **34**, R93 (2001).
[4] F. Aumayr and H. P. Winter, Nucl. Instrum. Methods Phys. Res., Sect. B **233**, 111 (2005).
[5] G. Borsoni *et al.*, Solid-State Electron. **46**, 1855 (2002).
[6] T. Meguro *et al.*, Nucl. Instrum. Methods Phys. Res., Sect. B **235**, 431 (2005).
[7] M. Terada *et al.*, Nucl. Instrum. Methods Phys. Res., Sect. B **235**, 452 (2005).
[8] J. Burgdörfer, P. Lerner, and F. Meyer, Phys. Rev. A **44**, 5674 (1991).
[9] F. Aumayr *et al.*, Phys. Rev. Lett. **71**, 1943 (1993).
[10] R. Köhrbrück *et al.*, Phys. Rev. A **45**, 4653 (1992).
[11] T. Schenkel *et al.*, Phys. Rev. Lett. **83**, 4273 (1999).
[12] U. Kentsch, H. Tyrroff, G. Zschornack, and W. Möller, Phys. Rev. Lett. **87**, 105504 (2001).
[13] R. Köhrbrück *et al.*, Phys. Rev. A **50**, 1429 (1994).
[14] R. D. Cowan, *The Theory of Atomic Structure and Spectra* (University of California Press, Berkeley, 1981).
[15] M. F. Gu, Astrophys. J. **582**, 1241 (2003).
[16] G. Wenzel, Z. Phys. **43**, 524 (1927).
[17] K. D. Sevier, *Low Energy Electron Spectrometry* (John Wiley & Sons, New York, 1972).
[18] R. W. Fink, R. C. Jopson, H. Mark, and C. D. Swift, Rev. Mod. Phys. **38**, 513 (1966).
[19] G. D. Archard, in *Proceedings of the Second International Symposium on X-Ray Microscopy and Microanalysis, Stockholm, 1959* (Elsevier, Amsterdam, 1960).
[20] J. Ducree, H. J. Andrä, and U. Thumm, Phys. Scr. **T80**, 220 (1999).
[21] J. Ducree, F. Casali, and U. Thumm, Phys. Rev. A **57**, 338 (1998).
[22] N. Stolterfoht, A. Arnau, M. Grether, R. Köhrbrück, A. Spieler, R. Page, A. Saal, J. Thomaschewski, and J. Bleck-Neuhaus, Phys. Rev. A **52**, 445 (1995).
[23] P. J. Cumpson and M. P. Seah, Surf. Interface Anal. **25**, 430 (1997).

APPLIED PHYSICS LETTERS **90**, 263502 (2007)

Lateral variation of target poisoning during reactive magnetron sputtering

D. Güttler, R. Grötzschel, and W. Möller[a)]
Institute of Ion Beam Physics and Materials Research, Forschungszentrum Dresden-Rossendorf, P.O. Box 510119, 01314 Dresden, Germany

(Received 11 May 2007; accepted 1 June 2007; published online 26 June 2007)

The reactive gas incorporation into a Ti sputter target has been investigated using laterally resolving ion beam analysis during dc magnetron deposition of TiN in an Ar/N_2 atmosphere. At sufficiently low reactive gas flow, the nitrogen incorporation exhibits a pronounced lateral variation, with a lower areal density in the target racetrack compared to the target center and edge. The findings are reproduced by model calculations. In the racetrack, the balance of reactive gas injection and sputter erosion is shifted toward erosion. The injection of nitrogen is dominated by combined molecular adsorption and recoil implantation versus direct ion implantation. © *2007 American Institute of Physics*. [DOI: 10.1063/1.2752019]

Magnetron sputtering[1,2] is a common technique in the fabrication of high quality functional thin films. In the reactive deposition mode,[3,4] a metal target is exposed to a rare gas discharge to which a fraction of reactive gas (such as nitrogen and oxygen) is added. At the substrate, the reactive gas reacts with the sputtered target material to the desired compound. Its stoichiometry depends, e.g., on the reactive gas partial pressure and the deposition power. The efficiency of the process, however, is often limited by the so-called target poisoning, which means that the compound layer forms not only on the substrate as desired but also on the sputter target. This results in a significantly reduced sputter yield, and thereby a reduced deposition rate. As a further consequence, the reactive gas consumption decreases due to the lower yield of sputtered material, and its partial pressure increases rapidly. For this situation, global particle-balance models of the interaction between gas flow, target erosion, and thin film deposition[5–7] show a partly negative slope of the relation between reactive gas flow and partial pressure, which results in a hysteresis behavior. A corresponding instability often requires additional means of stabilization for practical applications.[8] At the target, the particle balance is determined by the fluxes of neutral and ionic species from the gas and the plasma. The incorporation of reactive gas has been suggested to result from a stationary balance of injection by ion implantation and chemisorption in connection with recoil implantation, and erosion by ion-induced sputtering.[9–11] This was confirmed in previous experiments using *in situ* real-time ion beam analysis of the nitrogen incorporation at the target.[10]

Magnetron discharges are laterally strongly nonuniform due to the electron confinement in the magnetic field configuration. In front of a cylindrical magnetron target a toroidal region of high plasma density is formed, which creates the so-called racetrack as a zone of high target erosion. Consequently, also a nonuniform incorporation of reactive gas atoms can be expected. With this background, an experiment has been designed, which allows laterally resolved *in situ* ion beam analysis of the reactive gas incorporation at the target surface. A standard magnetron sputter configuration was installed in an ultrahigh vacuum chamber of 50 l volume. The planar, cylindrical dc magnetron of 5 cm diameter was equipped with a 99.995% purity titanium target and installed in the center of an ultrahigh vacuum chamber of 50 l volume. It was operated in constant current mode at 0.3 A. Using mass flow controllers, the argon and nitrogen flows were fixed at 10 SCCM (SCCM denotes cubic centimeter per minute at STP) and varied between 0 and 2.5 SCCM, respectively, which resulted in operating pressures between 0.3 and 0.35 Pa. The partial pressures were measured by means of a mass spectrometer, which was calibrated in pure Ar and N_2. The target voltage adjusted from $\sim$330 to $\sim$360 V at increasing reactive gas flow. For *in situ* ion beam analysis of the nitrogen incorporation at the target by means of the $^{14}N(d,\alpha)^{12}C$ nuclear reaction, the setup is attached to the beam line system of a 5 MV tandem ion accelerator (for details, see Ref. 10). The ion beam is collimated to a spot of 1×1 mm^2, which defines the lateral resolution of the analysis. The low cross section of the reaction requires analysis times of up to 30 min to obtain statistically satisfactory results. In order to reduce the consumption of the sputter target and the corresponding contamination of the target chamber, the measurements have been performed after magnetron operation. By comparison to real-time analysis during magnetron operation, it was assured that no postoperation nitrogen loss occurs.[10]

Figure 1(a) shows the radial distribution of the ion current density across the target surface, which has been derived from the surface erosion profile after long-time operation for 17 h with Ar inert gas only. The current density varies between about 1 and 50 mA/cm^2 at the target center and the centerline of the racetrack, respectively, and vanishes toward the target edge. There is a qualitative anticorrelation between the distribution of the ion current and the nitrogen areal densities shown in Fig. 1(b). The latter represent stationary distributions after a sufficiently long operation time for each parameter setting. [To achieve the stationary state, the eroded thickness should well exceed the thickness of the nitrided layer. With a sputter yield around 0.4 according to TRIM (Ref. 12) computer simulations, a current density of about 1 mA/cm^2 corresponds to sputter removal of 2.5×10^{15} at./cm^2 s. Thus, with the observed nitrogen areal density of $\sim1\times10^{16}$ cm^{-2}, the stationary state is achieved within about 10 s even at the target center.] The average nitrogen incorporation increases at increasing nitrogen gas

a)Author to whom correspondence should be addressed; electronic mail: w.moeller@fzd.de

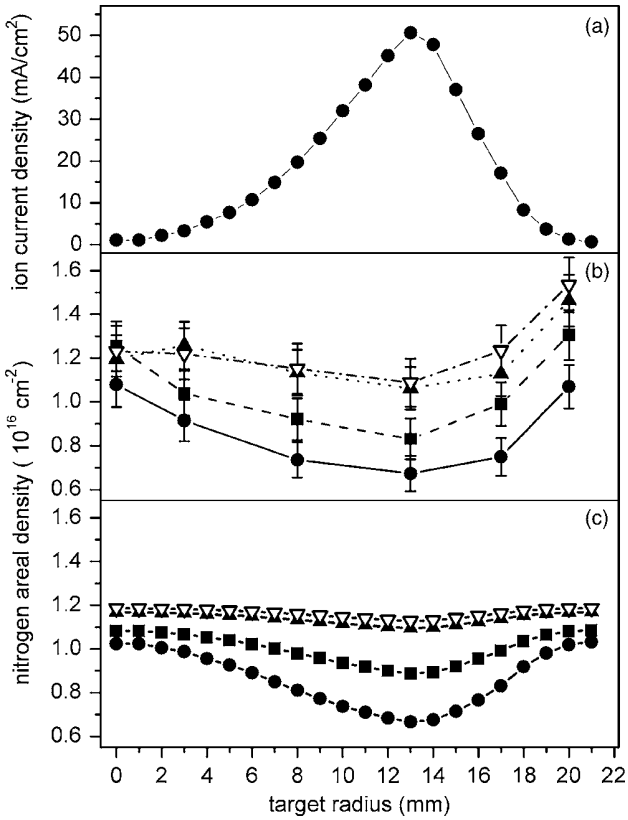

FIG. 1. Radial distributions of the ion current (a) and of the nitrogen areal density at the target surface at different nitrogen flows [(b) and (c)], as determined from ion beam analysis (b) and from model calculations (c). For (b) and (c), the nitrogen gas flows are 0.65 SCCM (dots), 1 SCCM (squares), 2 sccm (full triangles), and 2.5 SCCM (open triangles). The lines are added to guide the eyes.

flow. At the target center, the nitrogen areal density appears to saturate except for the lowest nitrogen flow. When neglecting sputtering, an upper estimate of the saturation areal density can be obtained assuming the formation of stoichiometric TiN within the range of the incident reactive gas ions. The dominant reactive ion species from the discharge is N_2^+, which, after acceleration by the target voltage and upon impinging the surface, splits into two atoms of half-energy. The range distribution of the resulting ~175 eV N atoms extends to about 2.7 nm in Ti,[12] which corresponds to a nitrogen areal density of 1.5×10^{16} cm^{-2} in rough agreement with the experimental result. Toward the centerline of the racetrack, the nitrogen incorporation decreases by ~45% and ~10% for the lowest and highest nitrogen flows, respectively. The radial position of minimum nitrogen incorporation is in good agreement with that of the maximum current density. Further, toward the edge of the target, the nitrogen areal density increases again in accordance with the decreasing ion flux. However, for the largest nitrogen flows, it increases to a level which is significantly above the saturation level at the target center, although the current density is similar. We ascribe this to some redeposition of Ti and corresponding compound formation in this outer area, although the transport mechanisms of redeposition are not obvious.

As briefly mentioned above, the stationary reactive gas incorporation results from a balance of reactive gas deposition and sputter erosion. The three major mechanisms of reactive gas accumulation are chemisorption of reactive gas molecules at the surface, direct implantation of ionized reactive species, and recoil implantation of the chemisorbed species by ion bombardment. Recoil implantation and sputter erosion are mainly due to inert gas ions, as the nitrogen addition is relatively small and the electron-impact ionization cross sections of Ar are larger than the ones of N_2.[14,15] All ion fluxes, and thereby the sputter erosion, follow the radial current distribution of Fig. 1(a), whereas the molecular gas flux arrives uniformly across the target. Thus, if adsorption in connection with recoil implantation plays a significant role for deposition, the deposition-erosion balance is shifted toward erosion in the center of the racetrack compared to the target center and edge, which results in a reduced nitrogen incorporation.

In order to corroborate this picture, quantitative model calculations have been performed. For this purpose, the dynamic global surface model given by Kubart *et al.*,[13] which incorporates the above mechanisms, has been applied to the stationary state. Compound formation at the surface is modeled by chemisorption of incident reactive gas molecules assuming a unity sticking coefficient on the metallic fraction of the surface. The corresponding gas-kinetic fluxes are derived from the nitrogen partial pressure, which has been measured using mass spectrometry for each setting of the reactive gas flow. Of ions, only Ar^+ and N_2^+ are taken into account, which are dominant in the discharge according to the electron-impact ionization cross sections.[14,15] The radially varying total (Ar^+ plus N_2^+) ion flux is taken from the radial distribution of Fig. 1(a). (Secondary electron production at the target is neglected, as it is known to be small.[16]) The Ar^+ to N_2^+ flux ratio is chosen according to the respective partial pressures and the ratio of the ionization cross sections. The latter is obtained by averaging the cross sections over an energy range extending from the ionization threshold to the target voltage. The yields of surface sputtering and recoil implantation are derived from TRIM (Ref. 12) with Ar^+ ions incident on 1 ML of TiN on Ti. (The surface binding energies have been chosen according to Ref. 17.) Recoil implantation of surface nitrogen atoms into the bulk and direct implantation of N_2^+ ions are modeled by a saturable transfer into a fixed monolayer at a depth of 2.7 nm (see above). Thus, the model neglects any details of the depth distributions of direct and recoil implantation and any in-depth multiple relocation of the reactive atoms.

Figure 1(c) shows the model prediction of the nitrogen incorporation versus the target radius. At the target center, the experimental results [cf. Fig. 1(b)] are reproduced quantitatively. As discussed above, the discrepancy at the target edge is attributed to redeposition. The sequence of the radial dependencies at different reactive gas flows shows good qualitative agreement between experiment and model results, although the shape of the radial dependencies appears somewhat different with a narrower depression in the racetrack obtained from the model. In particular, for the highest nitrogen flow, the predicted reduction of nitrogen incorporation in the center of the racetrack is in excellent agreement with the experiment. Thus, in view of the simplicity of the model, the agreement between model predictions and experiment can be regarded as being surprisingly good. The inspection of the nitrogen depth profiles obtained from the model shows that the saturated areal density is associated with the formation of a stoichiometric layer, whereas in the nonsaturated region around the racetrack centerline a constant, substoichiometric

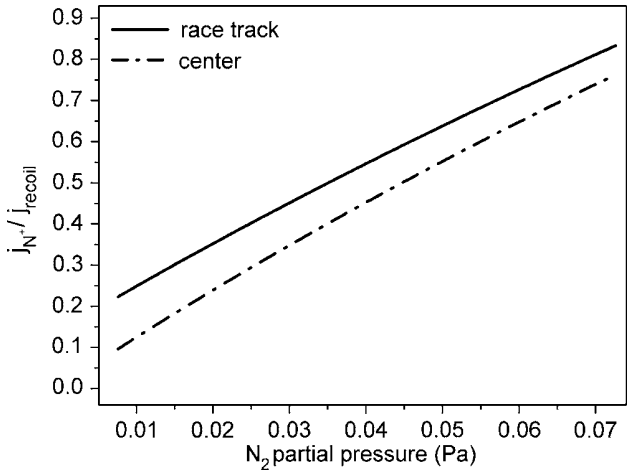

FIG. 2. Ratio of nitrogen injection by direct ion implantation and recoil implantation from the surface layer vs the nitrogen partial pressure for different target locations. $j_N{}^+$ and j_{recoil} denote the respective atomic nitrogen fluxes. The partial pressure of 0.07 Pa corresponds to a reactive gas flow of 2.5 SCCM.

nitrogen concentration extends from the surface into the depth. In view of the good agreement with the model results, we apply this picture with some confidence also to the interpretation of the experimentally observed areal densities.

In the framework of the above modeling, Fig. 2 illustrates the relative contributions of the mechanisms of nitrogen incorporation at different reactive gas flows and target locations, as calculated for the stationary state. In the present range of reactive gas partial pressure, combined chemisorption and recoil implantation dominates over direct ion implantation. This is consistent with the high gas-kinetic flux of nitrogen molecules relative to the flux of N_2^+ ions, and an efficient transfer of the chemisorbed nitrogen by recoil implantation into the bulk. At increasing nitrogen partial pressure, the relative contribution of direct ion implantation increases, as the surface becomes increasingly saturated. The latter limits the rate of chemisorption of gas molecules at the surface, and thereby the inward flux by recoil implantation. Comparing the two lines of Fig. 2, the relative contribution of direct ion implantation is somewhat higher in the racetrack. However, the difference is surprisingly small in view of the ion current distribution, which varies by more than one order of magnitude. This is again attributed to the limitation of combined chemisorption and recoil implantation, which occurs preferentially at the target center and edge. The high ion bombardment in the racetrack not only increases the relative contribution of direct implantation of reactive ions but also transfers chemisorbed nitrogen efficiently to the bulk by recoil implantation, so that a high rate of chemisorption is sustained.

In conclusion, we have demonstrated a significant variation of target poisoning across the target surface during reactive magnetron sputtering of TiN, which depends on the reactive gas admixture. For typical conditions of practical applications with a reactive gas addition of a few percent, the nitrogen incorporation in the racetrack may be reduced by almost 50% compared to the target center and edge. The experimental results are consistent with the simple modeling of the local particle balance. Ion implantation, reactive gas adsorption in combination with recoil implantation, and sputter erosion are confirmed as the main mechanisms of establishing the local target composition in the stationary state.

[1] J. A. Thornton and J. E. Greene, *Sputter Deposition Processes*, Handbook of Deposition Technologies for Films and Coatings, 2nd ed., edited by R. Bunshah (Noyes, Park Ridge, NJ, 1994), p. 249.
[2] P. Hovsepian, D. Lewis, and W. D. Münz, Surf. Coat. Technol. **133**, 166 (2000).
[3] S. Schiller, U. Heisig, C. Korndörfer, G. Beister, J. Reschke, K. Steinfelder, and J. Strümpfel, Surf. Coat. Technol. **33**, 405 (1987).
[4] W. D. Sproul, Science **273**, 889 (1996).
[5] S. Berg, H.-O. Blom, T. Larsson, and C. Nender, J. Vac. Sci. Technol. A **5**, 202 (1987).
[6] S. Berg, T. Larsson, H.-O. Blom, and C. Nender, J. Appl. Phys. **63**, 887 (1988).
[7] S. Berg and T. Nyberg, Thin Solid Films **476**, 215 (2005).
[8] T. Wallendorf, S. Marke, C. May, and J. Strümpfel, Surf. Coat. Technol. **174–175**, 222 (2003).
[9] D. Depla and R. De Gryse, Surf. Coat. Technol. **183**, 184 (2004); **183**, 190 (2004); **183**, 196 (2004).
[10] D. Güttler, B. Abendroth, R. Grötzschel, W. Möller, and D. Depla, Appl. Phys. Lett. **85**, 6134 (2004).
[11] D. Rosen, I. Katardjiev, S. Berg, and W. Möller, Nucl. Instrum. Methods Phys. Res. B **228**, 193 (2005).
[12] J. F. Ziegler, J. P. Biersack, and U. Littmark, *The Stopping and Range of Ions in Solids* (Pergamon, New York 1985), Chap. 8. (http://www.srim.org)
[13] T. Kubart, O. Kappertz, T. Nyberg, and S. Berg, Thin Solid Films **515**, 421 (2006).
[14] H. C. Straub, P. Renaud, B. G. Lindsay, K. A. Smith, and R. F. Stebbings, Phys. Rev. A **52**, 1115 (1995).
[15] H. C. Straub, P. Renaud, B. G. Lindsay, K. A. Smith, and R. F. Stebbings, Phys. Rev. A **54**, 2146 (1996).
[16] M. A. Lieberman and A. J. Lichtenberg, *Principles of Plasma Discharges and Materials Processing* (Wiley, New York, 1994), p. 467.
[17] W. Möller and M. Posselt, TRIDYN_FZR User Manual, Scientific Technical Report No. FZR-317 (Forschungszentrum Rossendorf, Dresden, Germany, 2001).

APPLIED PHYSICS LETTERS **90**, 181910 (2007)

Binary-collision modeling of ion-induced stress relaxation in cubic BN and amorphous C thin films

B. Abendroth,[a] H. U. Jäger, and W. Möller
Institute of Ion Beam Physics and Materials Research, Forschungszentrum Dresden-Rossendorf, D-01314 Germany

M. Bilek
Applied and Plasma Physics Department, School of Physics, University of Sydney, Sydney, New South Wales 2006, Australia

(Received 15 February 2007; accepted 2 April 2007; published online 1 May 2007)

It is demonstrated that ion-bombardment-induced stress release during physical vapor deposition of cubic boron nitride (*c*BN) and amorphous carbon (*a*C) films is related to collisional relocation of atoms. A model based on TRIM and molecular dynamics computer simulations is presented. Experimental results obtained using pulsed substrate bias are in good agreement with the model predictions at adequately chosen threshold energies of atomic relocation. The collisional relaxation model describes the experimental data significantly better than the widely applied thermal spike model. © *2007 American Institute of Physics*. [DOI: 10.1063/1.2734472]

Low-energy ion bombardment ($E_{ion} < 1$ keV) is widely used in physical and chemical vapor deposition of thin films to improve film adhesion, structure, and morphology.[1] By subplantation of primary ions or recoil atoms into the subsurface region,[2,3] ion bombardment facilitates the synthesis of metastable phases such as tetrahedral amorphous carbon (taC), as well as diamondlike carbon.[4] In the case of boron nitride deposition, low-energy ion bombardment is required to enable the nucleation and growth of the cubic (*c*BN) phase.[5,6] On the other hand, low-energy ion bombardment may lead to high compressive stress in the film, which in the case of *c*BN (Ref. 7) and *ta*C (Ref. 8) can reach 10 GPa, and hence limit the adhesion and the achievable film thickness. Davis[9] developed a model that relates the stress in thin films to the energy of incident particles. This model treats stress generation as a consequence of subplantation of primary ions or recoil atoms into subsurface regions. The density n of implanted atoms is approximately related to the ion flux j_i and energy E by $n \propto j_i E^{1/2}$.[10] A strain ε evolves, which is proportional to n. Elastic theory predicts a biaxial stress σ in the thin film on a substrate, which is proportional to ε.[11] Further, a thermal spike[12] that evolves around an ion impact allowing strained atoms to move to the surface, thereby decreasing n is invoked to describe stress relaxation. The balance between stress formation and relaxation in thermal spikes leads to a maximum of compressive stress at lower ion energies. At higher ion energies the relaxation outweighs the stress formation, resulting in lower net film stress. High-energy ion bombardment has been used specifically to reduce the stress in thin films. Good film qualities were achieved by combining the low-energy film forming particle flux j_0 with a high-energy ion flux j_i, with $j_i \ll j_0$ and $E(j_i) \gg E(j_0)$, for stress relaxation.[13–17] For *c*BN (Refs. 18 and 19) and amorphous carbon (*a*C) (Refs. 8 and 20) films, the stress relaxation due to high-energy ion impact has been studied systematically at varied ion flux and energy. Both materials show the same behavior of increasing stress relaxation as the product of ion energy and ion flux increases, followed by a saturation at a certain level of residual stress for high values of $E(j_i)j_i$. The same trends were also reported for the stress relaxation in AlN and TiN.[16,17] The dependence of the stress relaxation on Ej_i is in contradiction to the model of atomic rearrangements in a thermal spike as it is applied in the model described above[9] which predicts a scaling of the number of atomic relocations, and hence of the stress relaxation with $E^{5/3}$.[3,9,12] In the present letter we will demonstrate that the stress relaxation in *c*BN and *a*C can be described well by collisional relocation, rather than by using the thermal spike concept ($E^{5/3}$ scaling).

To model the stress relaxation, two particle flux components are considered as described above. The film forming flux j_0 is assumed to leave some atoms in interstitial or otherwise unfavorable positions, leading to a certain density n of atoms in strained bonding configurations. Stress relief occurs by relocations of these atoms from unfavorable positions due to energy transfer from the energetic ion flux j_i. Each incident ion activates some atoms within a certain volume around the impact site with a depth distribution function $f_a(x,E)$. Integration over x yields the total number of activation events, $\phi_a(E)$, per incident ion. In the dynamic situation of film growth, the average number of activation events, N_a, per atom of the growing film is obtained by integration with a moving boundary, i.e., the film surface, resulting in $N_a = (j_i/j_0)\phi_a(E)$, where j_0 can be written as the product of film atomic density n_0 and growth velocity v_g, assuming a unity incorporation of the film forming flux into the film. The relaxation rate of the strained atom density due to atomic relocations can be written as

$$\frac{dn(x)}{dt} = -j_i f_a(x,E)\frac{n(x)}{n_0}. \tag{1}$$

Substituting $dt = dx/v_g$ and integrating over time and depth yields the final density of unrelaxed atoms in the film,

[a]Electronic mail: b.abendroth@fzd.de

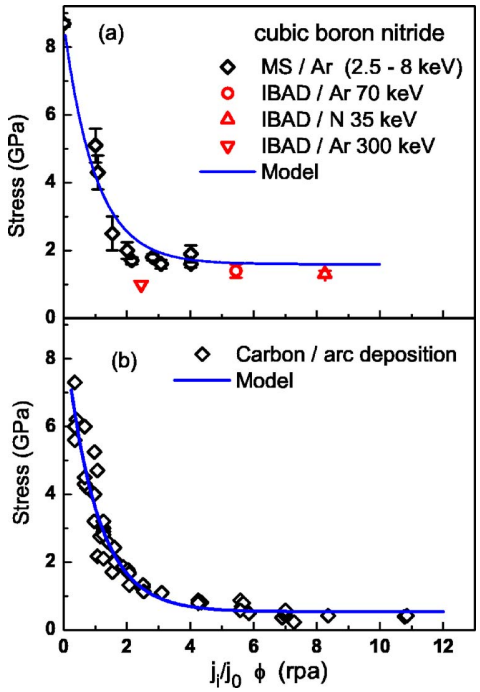

FIG. 1. (Color online) (a) Residual stress in *c*BN films deposited by magnetron sputtering and 2.5–8 keV Ar^+ implantation (diamonds) (Ref. 18), ion beam assisted deposition (IBAD) and Ar^+ implantation at 70 keV (circles), IBAD and N^+ implantation at 35 keV (up triangles) (Ref. 7), and IBAD and Ar^+ implantation at 300 keV (down triangles) (Ref. 23) as a function of relocations per atom (N_a) with the collisional relocation yield $\phi_a^{\mathrm{col}}(E)$ obtained from TRIM with a threshold energy $E_a^{\mathrm{col}}=7.2$ eV. The line represents the collisional relaxation model for *c*BN. (b) Residual stress in *a*C films (Refs. 8 and 20) as a function of N_a with $\phi_a^{\mathrm{col}}(E)$ obtained from TRIM with $E_a^{\mathrm{col}}=2$ eV. The line represents the collisional relaxation model for carbon.

$$n = n_u \exp\left(-\frac{j_i}{j_0}\phi_a(E)\right) = n_u \exp(-N_a), \tag{2}$$

with n_u being the density of unrelaxed atoms at zero flux of energetic ions. From elastic theory, the stress is proportional to the strain. Hence, the film stress is proportional to the density of unrelaxed atoms and can be written as

$$\sigma = (\sigma_u - \sigma_r)\exp\left(-\frac{j_i}{j_0}\phi_a(E)\right) + \sigma_r, \tag{3}$$

where σ_u is the intrinsic film stress without relaxation and σ_r is a residual stress which cannot be relaxed further, as is observed in the experiments. Note that compressive stress is set as positive.

In analogy to the concept of collisional damage,[21] the transferred energy must exceed a threshold energy E_a^{col} to produce a permanent relocation. For simplicity, we assume a sharp threshold rather than a spectrum of threshold energies. Based on the binary-collision approximation (BCA), the modified Kinchin-Pease (KP) model[21] predicts $\phi_a^{\mathrm{KP}}(E) = \gamma E/2E_a^{\mathrm{col}}$ for the number of relocations per incident ion, where γ is a constant with value around 0.8. The modified KP approximation becomes questionable in the threshold regime and it treats electronic stopping only in an approximate way. Therefore, higher accuracy BCA computer simulations (TRIM) (Ref. 22) have been employed here to obtain the collisional relocation function $\phi_a^{\mathrm{col}}(E)$.

Figure 1(a) shows the residual stress data for *c*BN films produced by magnetron sputtering (MS) and ion beam assisted deposition (IBAD). In the case of MS, the stress relaxation was achieved by Ar and N ion implantation in the energy range from 2.5 to 8 keV, created by applying a pulsed substrate bias with duty cycles ranging from 0.3% to 1.2%.[18] For stress relaxation during IBAD, Ar and N ions with energies ranging from 35 to 300 keV from ion implanters were used (for details, see Refs. 7 and 23). The line in the figure represents the theoretical exponential function according to Eq. (3). σ_u and σ_r are known from experiment and amount to 8.7 and 1.6 GPa, respectively. A best fit is obtained by varying the threshold energy of relocation in repeated TRIM simulations and occurs for a threshold energy $E_a^{\mathrm{col}}=7.2$ eV. It is seen that the experimental data obtained in different processes of thin film deposition are reproduced very well by the fitted model. The same procedure has also been applied to amorphous carbon films produced by plasma-immersion ion-assisted cathodic arc deposition.[8,20] Pulsed substrate bias voltages between 1.7 and 20 kV, a fixed pulse duration of 20 μs, and frequencies between 50 Hz and 1.2 kHz provided the energetic ions for stress relaxation in this case. The experiments yield an unrelaxed film stress of $\sigma_u=9$ GPa (from extrapolation to zero high voltage in the pulse) and a residual stress of $\sigma_r=0.54$ GPa after saturation. A relocation threshold energy around $E_a^{\mathrm{col}}=2.0$ eV was found to result in a satisfactory fit of the collisional stress release model to the experimental data. However, when tracing the collision cascades to such low energies, the validity of the BCA has to be seriously questioned.[24] Therefore, the number of relocations per incident ion was also calculated using molecular dynamics (MD) simulations[25,26] at incident ion energies between 0.1 and 2 keV, with a modified Brenner[27] potential governing the C–C interaction. For a threshold energy of 2 eV, the MD simulations reproduce the BCA simulation data perfectly,[28] thus again confirming their consistency with the model of collisional stress release.

As applied in the model of Davis[9] and according to Ref. 12, the thermal spike relocation yield is given by $\phi_a^{ts}(E) \approx 0.016(E/E_a^{ts})^{5/3}$ with E_a^{ts} denoting the activation threshold energy. The above sets of experimental data were also fitted using Eq. (3) and $\phi_a^{ts}(E)$. The best fits were obtained with values of $E_a^{ts}=13$ and 4 eV for *c*BN and *a*C, respectively, however, the quality of the best fits was clearly worse as compared to the collisional model. For the carbon data the mean square errors came to 11 and 54, using $\phi_a^{\mathrm{col}}(E)$ and $\phi_a^{ts}(E)$, respectively. Correspondingly, in the case of *c*BN, the mean square errors were 3.9 and 8.4, using the respective $\phi_a^{\mathrm{col}}(E)$ and $\phi_a^{ts}(E)$. This is consistent with the experimentally observed j_iE scaling, as described above, rather than a $j_iE^{5/3}$ scaling as employed in the thermal spike models. A similar result was reported in Ref. 29. The discrepancy between the thermal spike model and the experimental data is evident in Fig. 2 which shows the best fits for both models plotted against the carbon data. For a set of the *a*C data with constant duty cycle (0.4%), i.e., constant j_i/j_0, the film stress is shown as a function of the incident ion energy together with the best fits from the collisional and thermal spike models. In the critical region below 10 keV, the thermal spike model predicts significantly lower stress than measured, indicating that the relocation yield is overestimated by this model.

The threshold energy, which has been obtained above using the collisional model of relocation, is significantly

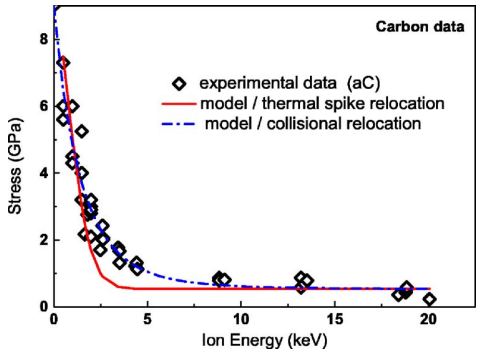

FIG. 2. (Color online) Experimental data (diamonds) for *a*C (Refs. 8 and 20) and the stress relaxation model with a relocation yield $\phi_a^{ts}(E)$ according to the thermal spike model with a threshold energy E_a^{ts}=4 eV (solid line) and a collisional relocation yield $\phi_a^{\mathrm{col}}(E)$ with E_a^{col}=2 eV (dash-dotted line) as a function of the ion energy at constant ion to neutral flux ratio.

larger for *c*BN than for *a*C. For *c*BN, it has been shown that stress relaxation occurs within the grains of the nanocrystalline material,[18,19] which may be ascribed to the removal of interstitial atoms from the grains and their transport to the grain boundaries. On the other hand, *a*C is amorphous in the stressed state, so that only slight rearrangements of the atomic configuration without significant atomic transport might result in stress release, which would require a lower energy transfer than for *c*BN. These pictures are qualitatively consistent with the observed residual stress σ_r upon saturation of stress relief, which, for *c*BN, is significantly larger and can be attributed to interface stress.[19] They are also consistent with the pronounced stability of *c*BN against ion irradiation,[7,19,30] whereas in *a*C, sp^3 bonds are easily transformed under ion irradiation into sp^2 hybridization,[31] leading to a swelling of the surface. The threshold energies for both materials are significantly lower than the conventional damage thresholds[21] which are characteristic for the creation of a stable Frenkel pair. The latter consumes the Frenkel pair formation energy plus a critical kinetic energy transfer for a sufficient separation of the interstitial-vacancy pair. In contrast, the displacement of a preexisting interstitial and a local rearrangement in an amorphous structure, which are responsible for stress relief in our cases, require clearly lower energy transfers.

The above j_iE scaling would be consistent with a universal role of the average energy parameter $(j_i/j_0)E$ in describing film growth and morphology, which has been discussed controversially in literature (e.g., Refs. 15 and 32, and references therein). However, the above scaling is only valid if the incident energies are large compared to the relocation threshold energies. This is not necessarily fulfilled in general, as, e.g., low substrate bias. Moreover, other collisional mechanisms, such as diffusion, may determine film growth and properties.

In conclusion, the results show that the stress relaxation by energetic ion bombardment is described well by a model based on collisional relocation of atoms in strained bonding configurations. The data and the model are consistent in a wide range of ion energies and for different deposition techniques. The Kinchin-Pease approximation, which predicts the collisional relocation yield per incident ion to be proportional to the ion energy, is consistent with the experimental finding that the stress relaxation depends on the product of ion flux and ion energy. In contrast, the thermal spike model is not supported by the data. These results suggest a critical revision of subplantation models of thin film growth which involve thermal spikes.

[1] L. Hultman, W.-D. Münz, J. Musil, S. Kadlec, I. Petrov, and J. E. Greene, J. Vac. Sci. Technol. A **9**, 434 (1991).
[2] Y. Lifshitz, S. R. Kasi, and J. W. Rabalais, Phys. Rev. Lett. **62**, 1290 (1989).
[3] J. Robertson, Diamond Relat. Mater. **2**, 984 (1993).
[4] M. Weiler, S. Sattel, T. Giessen, K. Jung, H. Ehrhardt, V. S. Veerasamy, and J. Robertson, Phys. Rev. B **53**, 1594 (1996).
[5] P. Mirkarimi, K. McCarty, and D. Medlin, Mater. Sci. Eng., R. **21**, 47 (1997).
[6] W. Kulisch and S. Ulrich, Thin Solid Films **423**, 183 (2003).
[7] C. Fitz, A. Kolitsch, W. Möller, and W. Fukarek, Appl. Phys. Lett. **80**, 55 (2002).
[8] M. M. M. Bilek, M. Verdon, L. Ryves, T. W. H. Oates, C. T. Ha, and D. R. McKenzie, Thin Solid Films **482**, 69 (2005).
[9] C. A. Davis, Thin Solid Films **226**, 30 (1993).
[10] P. Sigmund, in *Sputtering by Particle Bombardment*, edited by R. Behrisch (Springer, Berlin, 1981), Vol. 1, p. 9.
[11] H. Windischmann, J. Appl. Phys. **62**, 1800 (1987).
[12] F. Seitz and J. Koehler, Solid State Phys. **3**, 305 (1956).
[13] H. Ljuncrantz, L. Hultman, J. E. Sundgren, and L. Karlsson, J. Appl. Phys. **78**, 832 (1995).
[14] D. H. Lee, S. Fayeulle, K. C. Walter, and M. Nastasi, Nucl. Instrum. Methods Phys. Res. B **148**, 216 (1999).
[15] S. Mukherjee, F. Prokert, E. Richter, and W. Möller, Thin Solid Films **445**, 48 (2003).
[16] B. K. Gan, M. M. M. Bilek, D. R. McKenzie, Yang Shi, D. A. Tompset, M. B. Taylor, and D. G. McCulloch, J. Phys. D **16**, 1751 (2004).
[17] S. H. N. Lim, D. G. McCulloch, M. M. M. Bilek, and D. R. McKenzie, Surf. Coat. Technol. **174**, 76 (2003).
[18] B. Abendroth, R. Gago, A. Kolitsch, and W. Möller, Thin Solid Films **447**, 131 (2004).
[19] B. Abendroth, R. Gago, F. Eichhorn, and W. Möller, Appl. Phys. Lett. **85**, 5905 (2004).
[20] M. M. M. Bilek, D. R. McKenzie, and W. Möller, Surf. Coat. Technol. **186**, 21 (2004).
[21] M. Nastasi, J. Mayer, and J. Hirvonen, *Ion-solid Interactions: Fundamentals and Applications* (Cambridge University Press, Cambridge, 1996).
[22] J. Ziegler, J. Biersack, and U. Littmark, *The Stopping and Range of Ions in Solids* (Pergamon, New York, 1985).
[23] H.-G. Boyen, P. Widmayer, D. Schwertberger, N. Deyneka, and P. Ziemann, Appl. Phys. Lett. **76**, 709 (2000).
[24] W. Eckstein, *Computer Simulation of Ion-Solid Interactions* (Springer, Berlin, 1991).
[25] H. U. Jäger and A. Y. Belov, Phys. Rev. B **68**, 024201 (2003).
[26] A. Y. Belov and H. U. Jäger, Thin Solid Films **482**, 74 (2005).
[27] D. W. Brenner, Phys. Rev. B **42**, 9458 (1990); **46**, 1948 (1992).
[28] W. Möller, B. Abendroth, H.-U. Jäger, and M. Bilek (unpublished).
[29] M. M. M. Bilek and D. R. McKenzie, Surf. Coat. Technol. **200**, 4645 (2006).
[30] S. Eyhusen, I. Gerhards, H. Hofsäss, C. Ronning, M. Blomenhofer, J. Zweck, and M. Seibt, Diamond Relat. Mater. **12**, 1877 (2003).
[31] T. W. H. Oates, L. Ryves, F. A. Burgmann, B. Abendroth, M. M. M. Bilek, D. R. McKenzie, and D. G. McCulloch, Diamond Relat. Mater. **12**, 1395 (2005).
[32] I. Petrov, F. Adibi, J. E. Greene, L. Hultman, and J. E. Sundgren, Appl. Phys. Lett. **63**, 36 (1993).

PRL 99, 167202 (2007) PHYSICAL REVIEW LETTERS week ending 19 OCTOBER 2007

Dynamic Vortex-Antivortex Interaction in a Single Cross-Tie Wall

K. Kuepper,[1,*] M. Buess,[2] J. Raabe,[2] C. Quitmann,[2] and J. Fassbender[1]

[1]*Forschungszentrum Dresden-Rossendorf, Post Office Box 51 01 19, D-01314 Dresden, Germany*

[2]*Swiss Light Source, Paul Scherrer Institut, CH-5232 Villigen, Switzerland*

(Received 1 March 2007; revised manuscript received 17 May 2007; published 18 October 2007)

A fascinating property of micromagnetism comes from the possibility to control the domain and vortex configuration through the sample shape and size. For instance, in a rectangular platelet a configuration containing a stable combination of vortices and an antivortex can be created. Such a single cross-tie wall can be understood as being a coupled micromagnetic system with three static solitons. Here we report on its magnetization dynamics including the vortex-antivortex interactions. The spectrum of eigenmodes is investigated as well as the effect of different vortex core orientations. We show that the vortex dynamics can be used to identify the core configuration, which is not directly accessible to x-ray microscopy because of its limited spatial resolution.

DOI: 10.1103/PhysRevLett.99.167202 PACS numbers: 75.40.Gb, 75.60.Ch, 75.75.+a

Two-dimensional topological solitons are fascinating for researchers in many fields. These solitons determine the properties of very different systems such as atoms in superfluids and Bose-Einstein condensates [1,2] and Cooper pairs in superconductors. In thin ferromagnetic films they can be present as vortices and antivortices [3–7]. Because vortex and antivortex are the corresponding antiparticles they can annihilate under emission of energy [8]. However, in special geometries a stable combination of vortices and antivortices can be obtained. A cross-tie wall is an example of an infinite chain of vortices and antivortices.

Here we study a ferromagnetic rectangle, containing two vortices and a single antivortex, thus forming the unit cell of a cross-tie wall. The solitons are coupled through the domain walls and domains. This special geometry provides insight into the vortex configuration and into coupling effects which turn out to be very relevant for the dynamics of these solitons.

Up to now, significant effort has been invested in understanding the dynamics of ''simple'' magnetic vortex structures, such as thin permalloy squares and disks. Time-resolved imaging [9,10] allows us to investigate their excitations and switching in the time-domain [11–14]. Vortex-antivortex interaction has also attracted attention in semicontinuous films because of potential applications for spin wave radiation devices [8,15], and magnetic pinning arrays for superconducting films [16].

Neudert *et al.* [17] have investigated the generation of cross-tie walls in large permalloy platelets following the excitation by field pulses using Kerr microscopy. In this Letter we investigate the excitations of a single cross-tie wall by combining micromagnetic simulations based on the LLG equation [18] and magnetic imaging by means of time-resolved photo emission electron microscopy (PEEM). We study the response to weak magnetic in-plane field pulses, concentrating on the dynamics of the vortices and the antivortex and their mutual interaction.

Permalloy ($Ni_{81}Fe_{19}$) samples of 50 μm length, 6 μm width, and 20 nm thickness were prepared on a 10 μm wide coplanar waveguide. A rectangular element of 10×6 μm^2 was patterned by focused ion beam (FIB) sputtering. The time and spatially resolved magnetization was measured using PEEM. Employing x-ray magnetic circular dichroism at the Fe L_3 edge the image intensity is $I \propto M_y(\vec{r}) \cdot \vec{P}$. We use a gray scale representation with white representing the parallel and black the antiparallel orientation of the magnetization and the polarization. The rectangle is excited every 16 ns using magnetic field pulses synchronized to the x-ray pulses emitted by the synchrotron. The time dependence is measured by varying the time delay Δt [12]. The field pulse $\vec{H}_p$ is along the y direction and has a magnitude of ≈ 20 Oe and a temporal width of 500 ps with a rise time of about 150 ps.

First we discuss the equilibrium magnetization of a ferromagnetic platelet containing a single cross-tie wall. Figure 1(a) shows the simulated in-plane component $M_y(\vec{r})$ of the magnetization. The magnetization configuration can be thought of as consisting of two squares, each having a clockwise flux-closure pattern and containing a vortex core in its center. The two flux-closure patterns are separated by

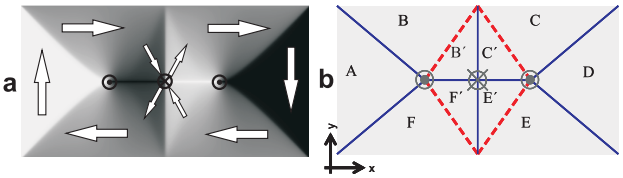

FIG. 1 (color online). (a) Micromagnetic simulation showing $M_y(\vec{r})$ for a rectangular platelet (5 μm $\times$ 3 μm $\times$ 20 nm) containing a single cross-tie wall. (b) Sketch depicting the 90° Néel walls (solid lines, blue) and the 45° pseudo Néel walls (dashed lines, red). The vortex cores have an out of plane magnetization with positive (u or ⊙) or negative (d or ⊗) z direction. Here we find [udu].

a Néel wall of ~90° running along the y axis and containing the antivortex at the center. A second Néel wall connecting the two vortex cores runs along the x axis [see Fig. 1(b)]. The cross-tie structure consists of these 90° Néel walls and four 45° pseudo Néel walls (dashed lines). The latter are pseudo domain walls, because along them the magnetization rotates continuously (e.g., between domains B and B'). In addition there are four 90° Néel walls (solid lines) running from the platelet edges to the vortex cores. To reduce the exchange energy that would be associated with spins on neighboring atoms pointing antiparallel, the magnetization of the vortex and antivortex rotates out of plane in a narrow region called the core. This core can point either in positive (u or ⊙) or in negative (d or ⊗) z direction resulting in a total of 2^3 possible configurations.

PEEM images of the magnetization $M_y(\vec{r}, \Delta t)$ of the permalloy rectangle ($10\,\mu\text{m} \times 6\,\mu\text{m} \times 20\,\text{nm}$) are shown in Fig. 2 (for a movie of the full series see Ref. [19]). The top row displays the experimental data, the second row the corresponding micromagnetic simulations. The two subsequent rows show difference images $M_y(\vec{r}, \Delta t) - M_y(\vec{r}, 0)$ for experiment and simulation, respectively. These difference images visualize the changes relative to the equilibrium state. In our geometry, the short edge of the rectangle is along the y direction and parallel to both the x-ray polarization $\vec{P}$ and the magnetic field pulse $\vec{H}_p$.

The first image shows the equilibrium state of the magnetization ($\Delta t = 0$). The domains A-F are similar to domains in conventional flux-closure patterns. Domain A, which is parallel to $\hat{y}$, is white and domain D, which is antiparallel, is black. Domains B, C, E, and F are gray since their magnetization is perpendicular to $\hat{y}$. The domains B', F', C', and E' in the cross-tie are at $\pm 45°$ to $\hat{y}$ resulting in darker and lighter gray values, respectively.

Next we discuss the temporal evolution of the magnetization. At a delay of $\Delta t = 300$ ps all domains having a finite x component of the magnetization in the equilibrium state have become brighter. The reason is the torque ($\vec{M} \times \vec{H}_p$) exerted by the field pulse causing an excursion in the z direction followed by a precession. This rotates their magnetization into the y direction leading to a higher intensity. Only domains A and D do not show such an increased intensity because they are parallel and antiparallel to the field pulse, respectively.

In addition the 90° Néel walls originating from the flux-closure pattern and the cross-tie wall pointing along $\hat{y}$ bulge to the right. In the difference images these effects show up as bright areas and lines, respectively. At $\Delta t =$ 450 ps the coherent precession in the domains has continued. The magnetization is almost perpendicular to $\hat{y}$, resulting in a gray difference intensity. The bulged domain walls are now even more intense than at $\Delta t = 300$ ps and are visible in experiment and simulation. At $\Delta t = 600$ ps the ongoing precession leads to a brighter appearance of domains B, C, E, and F again. For this delay time we observe a maximum in the curvature of both, the cross-tie wall along $\hat{y}$ and the 90° Néel walls along the black (D) and white (A) domains.

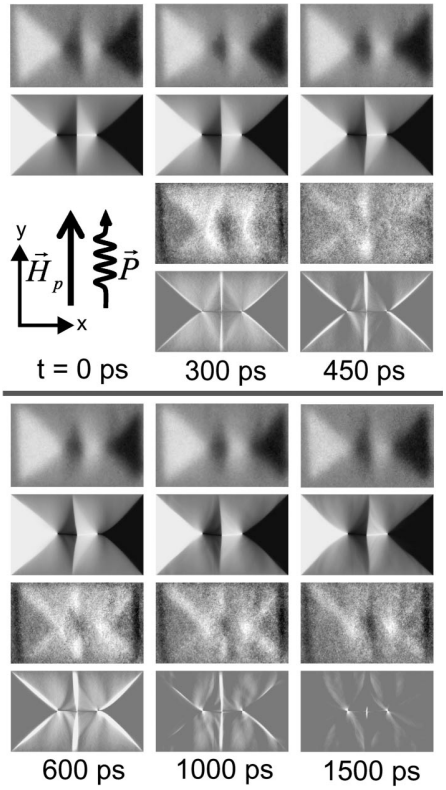

FIG. 2. Magnetization $M_y(\vec{r}, \Delta t)$ at characteristic delay times. Experimental results (top row) and difference images (third row) are compared to the corresponding simulation (second and fourth row).

Turning to longer delays, the vortex dynamics becomes prominent. The difference images show that the Landau like domains A-F have almost completely relaxed back to the equilibrium state. The domain walls, the two vortices, and the antivortex, on the other hand, are still displaced, resulting in a finite intensity for the difference images. For 1500 ps, the main visible features are the two vortices and the antivortex, indicating their slow relaxation into the equilibrium state. For all delays we find reasonable agreement between simulation and experiment [20].

To gain further insight into the dynamics we perform a Fourier transformation [21,22] of the experimental data, using a Hamming cutoff window. Large Fourier amplitudes indicate eigenfrequencies of the system. Figure 3 shows the spatial distribution of the Fourier amplitude and phase for the observed eigenfrequencies. For the higher frequencies (2.2 and 2.4 GHz) the intensity dominates in the domains B, C, E, and F, all of which have their equilibrium magnetization perpendicular to $\vec{H}_p$. The frequencies and the observed phase shift of π (corresponding to a change from red to blue in Fig. 3) are in good agreement with the findings in Landau flux-closure structures [12].

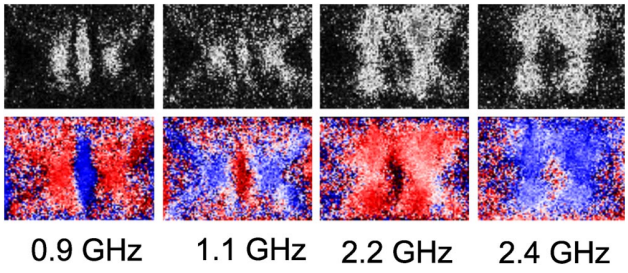

FIG. 3 (color online). Spatial distribution of the Fourier components of the magnetization $M_y(\vec{r})$ at characteristic frequencies showing amplitude (top) and phase (bottom: dark gray, blue online = 0, light gray, red online = π).

The wall modes occur at lower frequencies. For 1.1 GHz we find large Fourier amplitudes around the two vortices, the antivortex positions, and the corresponding domain walls. In addition they seem to radiate out along the 90° Néel walls, indicating the coupling of the vortices to these domain walls. At 0.9 GHz, corresponding to the longest time scale visible in our experiment, the dominant feature is the cross-tie wall along $\hat{y}$ indicating that it is the last subcomponent of the pattern responding to the exciting field pulse. This wall mode at 0.9 GHz is phase shifted by π with respect to the mode at 1.1 GHz. For both low frequency modes it is evident that the movement of the core positions is coupled to the adjacent domain walls, which mediates the mutual interaction of different cores by the exchange interaction within the wall.

Having studied the response of the domains and the domain walls we now focus on the vortex core dynamics and the effect of different core configurations. Our rectangle with the cross-tie wall containing two vortices and a single antivortex can have $2^3 = 8$ different configurations. There are two configurations where both vortex cores have the same orientation, but are opposite to the antivortex (I): $[udu]$, $[dud]$. There are four configurations where both vortex cores are antiparallel (II): $[uud]$, $[udd]$, $[duu]$, $[ddu]$. And last there are two configurations where all three cores are parallel (III): $[uuu]$, $[ddd]$.

Comparing the three configurations their total energies are very similar ($E_{udu} = 1.1254 \times 10^{-9}$ erg, $E_{duu} = 1.1392 \times 10^{-9}$ erg, $E_{uuu} = 1.1392 \times 10^{-9}$ erg). Their total energies differ only about 1%, and thus the present configuration is *a priori* not clear; however, the contribution of the exchange and demagnetizing energy differ substantially, indicating a change in the coupling between the vortex cores [19]. The core orientation is relevant since it determines the sense of rotation for the gyrotropic motion. Note that for the same orientation vortex and antivortex have an opposite sense of rotation [8]. A first example of a vortex-vortex interaction has been demonstrated by Buchanan *et al.* [23] for the case of a two-vortex system. Here we study the interaction in a system containing both vortex and antivortex cores.

From the simulated time series we extract the vortex and antivortex core positions. Figure 4(a) shows the displacements for the three different configurations (I, II and III) [18]. The vortex and antivortex motions show a very different behavior depending on the configuration. For configuration (I) [Fig. 4(a), top row] all three cores have the same sense of rotation [counterclockwise (ccw)], and the amplitudes and frequencies are similar. However, the antivortex exhibits a 180° phase shift. This opposite motion of vortex and antivortex cores might also be called an optical mode. For configuration (II) the vortex cores point along opposite directions. This leads to different interaction with the antivortex. Compared to configuration (I), in particular, the antivortex and the right vortex core exhibit a significantly reduced gyration. For configuration (III) an

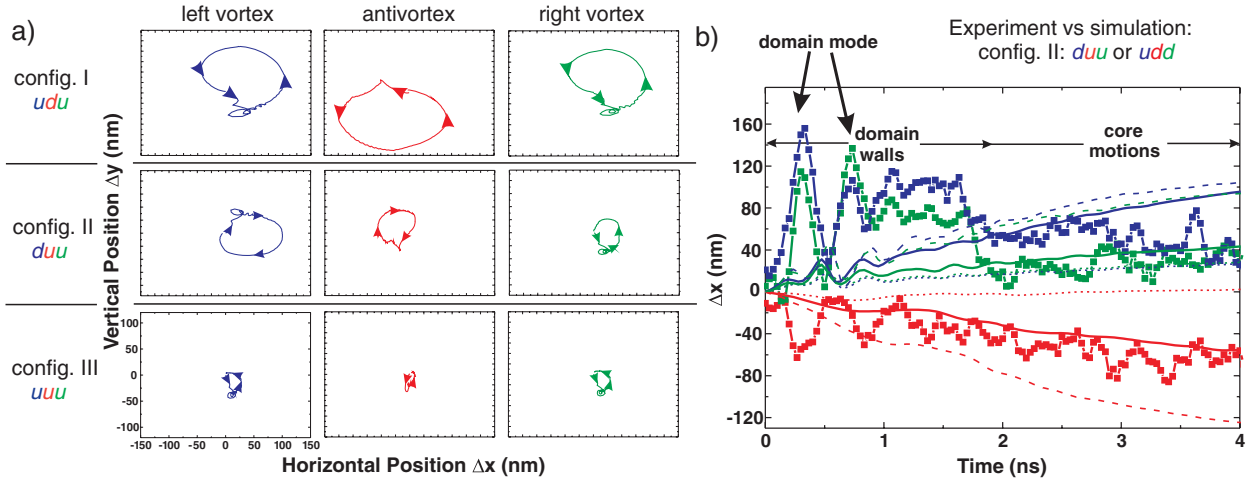

FIG. 4 (color online). (a) Trajectories of the two vortex (left and right, blue and green online) and the antivortex (center, red online) core displacements as extracted from micromagnetic simulations [18] ($\Delta t = 0 - 16$ ns) (see text). The arrows indicate the sense of rotation for the core motion. (b) Horizontal core displacement from experiment (■) and the three possible configurations [configuration (I) (dashed line), configuration (II) (solid line), and configuration (III) (dotted line)].

even more complex behavior is observed. The amplitudes of all three cores are even more reduced. The two vortex cores gyrate as expected (ccw) and again have comparable amplitudes. The antivortex core gyration is, however, opposite from what was expected and its amplitude is reduced significantly. The reason is the interaction with the adjacent vortex cores, quenching the free gyration of the antivortex. The remaining five configurations can be deduced by means of symmetry considerations, provided the symmetry breaking caused by the direction of the pulse field H_p is neglected.

From the above results it is evident that the vortex-antivortex interaction, mediated by the exchange interaction of the corresponding domain walls, is very important for the magnetization dynamics of a single cross-tie wall. All other systems comprising multiple vortex and/or antivortex structures are likely to exhibit an even more complex dynamic behavior which can only be explained with a detailed understanding of the individual constituents.

To finally determine which of the 2^3 possible core configurations is present in our experiment we make use of the strong configuration dependence of the dynamics presented in Fig. 4(a). The horizontal vortex displacements determined from experiment and simulations are compared in Fig. 4(b).

For configuration (II) we observe an agreement in the horizontal displacement direction for all three moving cores and in addition comparable amplitudes for $\Delta t \gtrsim 2$ ns. For $\Delta t \lesssim 2$ ns the movements of the domain and the domain walls are strongly overlapping the vortex and antivortex movements (see Fig. 2) leading to a large uncertainty in the experimental determination of the core position. The horizontal displacement of the antivortex and the right vortex is very well reproduced, whereas the left vortex shows a somewhat larger displacement in the simulation; however, this deviation is comparable to the precision of the core determination of about 30 nm.

An analysis of the vertical displacement is more difficult because of the reduced amplitudes and is not shown. We can therefore not distinguish between a $[duu]$ and a $[udd]$ configuration consistent with the horizontal displacement observed for configuration (II). However, we can conclude that one vortex is antiparallel to the antivortex and the other vortex core in the present experiment.

In summary, we report results of vortex-antivortex dynamics. These include the dynamics of antivortices and the indirect coupling between vortex cores and the antivortex, which is mediated by the exchange interaction of the adjacent domain walls. This coupling is significant and introduces unexpected effects, such as the quenching of gyrotropic motion for the antivortex in certain core configurations. Another consequence is the absence of simple eigenmodes describing the vortex gyration. By using simulations the strong influence of the vortex coupling on the core dynamics can in turn be used to determine the core configuration, a parameter otherwise inaccessible to direct observation.

Part of this work has been performed at the Swiss Light Source, Paul Scherrer Institut, Villigen, Switzerland. We are grateful to L. Bischoff for performing FIB. We thank S. Wintz, B. Liedke, M. R. Scheinfein, and C. H. Back for support and helpful discussions. We are indebted to D. Weiss (University of Regensburg) for making the cleanroom available.

*k.kuepper@fzd.de

[1] D. R. Tilley and J. Tilley, *Superfluidity and Superconductivity* (IOP Publishing Ltd., Bristol, 1990), 3rd ed..
[2] M. R. Matthews *et al.*, Phys. Rev. Lett. **83**, 2498 (1999).
[3] G. Blatter *et al.*, Rev. Mod. Phys. **66**, 1125 (1994).
[4] C. Kittel, Rev. Mod. Phys. **21**, 541 (1949).
[5] A. Hubert and R. Schäfer, *Magnetic Domains* (Springer, Berlin, 1998).
[6] J. Raabe *et al.*, J. Appl. Phys. **88**, 4437 (2000).
[7] A. Wachowiak *et al.*, Science **298**, 577 (2002).
[8] R. Hertel and C. M. Schneider, Phys. Rev. Lett. **97**, 177202 (2006).
[9] Y. Acremann *et al.*, Science **290**, 492 (2000).
[10] T. Gerrits *et al.*, Nature (London) **418**, 509 (2002).
[11] S.-B. Choe *et al.*, Science **304**, 420 (2004).
[12] J. Raabe *et al.*, Phys. Rev. Lett. **94**, 217204 (2005).
[13] K. Kuepper *et al.*, Appl. Phys. Lett. **90**, 062506 (2007).
[14] B. van Waeyenberge *et al.*, Nature (London) **444**, 461 (2006).
[15] S.-K. Kim *et al.*, Appl. Phys. Lett. **86**, 052504 (2005).
[16] M. V. Milošević and F. M. Peeters, Phys. Rev. Lett. **93**, 267006 (2004).
[17] A. Neudert *et al.*, J. Appl. Phys. **99**, 08F302 (2006).
[18] http://llgmicro.home.mindspring.com We use standard permalloy material parameters: exchange constant $A = 8 \times 10^{-12}$ J/m, saturation magnetization $M_s = 860.000$ A/m, magnetic damping constant $\alpha = 0.01$, uniaxial anisotropy $K_u = 0$. To take into account a possible resonant excitation we simulate a sequence of five full excitation cycles (every 16 ns) for each configuration. We observe no significant change in the frequencies or the trajectories of the vortex cores, only the amplitudes of the trajectories increase. For the analysis we use the averaged results of the third—fifth excitation cycles.
[19] See EPAPS Document No. E-PRLTAO-99-053742 for a table displaying the energies of the three configuations and a movie of the data shown in Fig. 2. For more information on EPAPS, see http://www.aip.org/pubservs/epaps.html.
[20] Simulations were done for a rectangle of ($5\ \mu$m $\times$ $3\ \mu$m $\times$ 20 nm) and a cell size of $5 \times 5 \times 20$ nm^3 to limit the neccessary memory and and computing times. The experiments are done on larger rectangles of ($10\ \mu$m $\times$ $6\ \mu$m $\times$ 20 nm). We find good agreement between simulation and experiment justifying reduced size for the simulation.
[21] J. P. Park *et al.*, Phys. Rev. B **67**, 020403 (2003).
[22] M. Buess *et al.*, Phys. Rev. Lett. **93**, 077207 (2004).
[23] K. S. Buchanan *et al.*, Nature Phys. **1**, 172 (2005).

Journal Reprint
RAPID COMMUNICATIONS

PHYSICAL REVIEW B **75**, 220407(R) (2007)

Induced anisotropies in exchange-coupled systems on rippled substrates

M. O. Liedke,[1,2] B. Liedke,[1] A. Keller,[1] B. Hillebrands,[2] A. Mücklich,[1] S. Facsko,[1] and J. Fassbender[1,*]
[1]*Institute of Ion Beam Physics and Materials Research, Forschungszentrum Dresden-Rossendorf, P.O. Box 51 01 19, D-01314 Dresden, Germany*
[2]*Fachbereich Physik, TU Kaiserslautern, Erwin-Schroedinger-Strasse 56, D-67663 Kaiserslautern, Germany*
(Received 1 June 2007; published 25 June 2007)

The role of monoatomic steps at the mutual interface between a ferromagnetic and an antiferromagnetic layer in a $Ni_{81}Fe_{19}/Fe_{50}Mn_{50}$ exchange bias system is enlightened. For this purpose a special ripple substrate with a well defined morphology is used. Due to the film morphology a strong uniaxial anisotropy is induced in the polycrystalline $Ni_{81}Fe_{19}$ layer, which is fixed in its orientation. By means of different field annealing cycles the direction of the induced unidirectional anisotropy can be chosen. For all mutual orientations both anisotropy contributions are superimposed independently and the angular dependence of the magnetization reversal behavior can be described perfectly by a coherent rotation model with one parameter set. In addition it is demonstrated that the magnitude of the unidirectional anisotropy contribution scales with the step density of the substrate, which is in full agreement with theoretical predictions.

DOI: 10.1103/PhysRevB.75.220407 PACS number(s): 75.30.Gw, 68.35.Ct, 75.70.Cn, 75.75.+a

A thin ferromagnetic layer experiences a unidirectional anisotropy when an internal magnetic field is created due to the exchange coupling to an antiferromagnetic layer of sufficient thickness.[1,2] A shift of the hysteresis loop, the so-called exchange bias field H_{eb}, is observed if the induced internal field exhibits a well defined direction. This is conventionally achieved by a field annealing cycle, i.e., the magnetization of the ferromagnetic layer is aligned along any desired direction, when the antiferromagnetic layer is cooled down below the blocking temperature. By doing so the spin configuration of the antiferromagnetic layer is frozen and generates an internal magnetic field which acts on the ferromagnetic layer. Since in a polycrystalline film the grains are usually randomly oriented in the film plane, no higher-order anisotropies are present and the angular dependence of H_{eb} follows a simple cosine behavior, $H_{eb}(\alpha_M)=H_{eb}\times\cos(\alpha_M-\alpha_{K_1})$, as expected from a coherent rotation model. α_M (α_{K_1}) is the angle between the magnetization direction (field-cooling direction) and a reference direction. However, if higher-order anisotropy contributions are present, as, for example, magnetocrystalline contributions in epitaxial systems,[3–6] buffer induced anisotropy contributions,[7,8] or shape anisotropy contributions in patterned films,[9,10] a complicated angular dependence of the magnetization reversal behavior is observed. If in addition interfacial roughness comes into play, even more parameters enter the magnetization reversal process,[11–13] which further complicate the interpretation. In general, in experimental papers addressing the effect of interfacial roughness published so far, the amount of roughness could neither be varied easily nor quantified absolutely. Thus no consensus about the effect of interfacial roughness on the unidirectional anisotropy could be achieved.

In this Rapid Communication a special template system is used which allows us (i) to easily determine the step density and thus the interfacial roughness, and (ii) to induce a strong uniaxial anisotropy which is directly related to the highly anisotropic step distribution. Thereby we can (i) unambiguously determine the roughness induced increase in unidirectional anisotropy, and (ii) since by means of different magnetic-field annealing cycles the mutual angle between uniaxial and unidirectional anisotropy can be chosen independently, we can study their potential intercorrelation.

In order to create such a template system, self-organized ripple formation during low-energy ion erosion is employed. This process is well known for semiconductor surfaces,[14,15] where rather high topographic modulations (typically 2–20 nm) can be achieved. However, due to the ion erosion process the sample surface is amorphized. Ripple formation has also been studied for metallic surfaces and magnetic thin films.[16–18] In these cases the topographic modulations are much smaller ($\leqslant$0.2 nm) and so far these investigations are restricted to single crystalline surfaces. Therefore step-or morphology-induced anisotropy contributions are always superimposed by magnetocrystalline contributions. In order to simplify the interpretation of our results, magnetocrystalline anisotropy contributions have to be circumvented. This has been achieved by the deposition of initially low anisotropic polycrystalline $Ni_{81}Fe_{19}$ films on top of rippled Si surfaces.

The Si templates are created by 500-eV Ar^+ sputtering of a Si(001) wafer with an incident angle of 67° with respect to the surface normal in high vacuum. A sputter fluence of 1×10^{18} ions/cm^2 leads to a modulated Si surface which after deposition of a metallic buffer produces subsequently a high anisotropic step density (see Fig. 1). After ion erosion the templates have been removed from the vacuum chamber which leads to a natural oxide of 2–4 nm on the surface. Subsequent to initial atomic force microscopy (AFM) characterization the template was inserted into a molecular-beam epitaxy system. Prior to film deposition the sample was heated to 250 °C in order to clean the sample surface. Subsequently the whole layer stack, 2-nm Mn/9-nm $Ni_{81}Fe_{19}$/10-nm $Fe_{50}Mn_{50}$/2-nm Cr, was deposited at room temperature by *e*-beam evaporation (Cr, $Ni_{81}Fe_{19}$, Fe) and from a Knudsen cell (Mn), respectively. In order to compare the exchange bias system with the single ferromagnetic layer, the antiferromagnetic FeMn layer was deposited on half of the sample only. Subsequently the surface topography was reinvestigated by means of *ex situ* AFM. In order to further clarify the film morphology, cross-sectional transmission

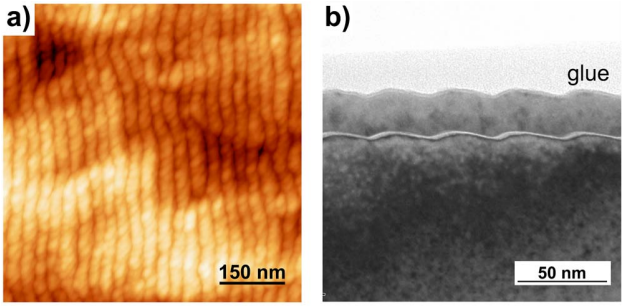

FIG. 1. (Color online) (a) AFM image of the surface topography of the exchange bias layer stack. (b) Cross-sectional TEM image of the Si ripple and metallic layer structure. The film morphology perfectly reproduces the ripple substrate.

electron microscopy (TEM) was performed for a different sample fabricated using the same recipe.

In Fig. 1(a) an AFM micrograph of the layer stack surface is shown. The ripple periodicity can be determined to $\lambda = 32$ nm from the satellite peaks observed in the two-dimensional (2D)-Fourier transform of the AFM image. A peak-to-valley height of ≈ 2 nm is observed. This corresponds to a mean local inclination of the fiber-textured (111) surface of 7°, i.e., one monoatomic step per seven atoms. The rms roughness of the ripple structure is determined to $w = 0.74$ nm. Although the metallic layer thickness is much larger than the surface corrugation of the initial template system, the ripple structure is reproduced completely with respect to periodicity and modulation amplitude. This can be observed nicely by inspection of the cross-sectional TEM image shown in Fig. 1(b).

For the interpretation of the magnetic measurements one of the crucial issues is to determine the different anisotropy contributions with the highest achievable accuracy. Therefore the whole angular dependence (360°) of the magnetization reversal behavior was measured (1° step size) and compared to numerical simulations based on a coherent rotation model which allows for the calculation of the hysteresis curves and subsequently of the angular dependence of H_{eb}. In this extended Stoner-Wohlfarth model[19,20] the free-energy density can be written as

$$f(\alpha_M) = -|\vec{M}||\vec{H}|\cos(\alpha_M - \alpha_H) - K_1 \cos(\alpha_M - \alpha_{K_1}) - K_2 \cos^2(\alpha_M - \alpha_{K_2}).$$

K_1 and K_2 are the unidirectional and uniaxial anisotropy constants, respectively, $\vec{H}$ is the applied field, and $\vec{M}$ is the magnetization. All angles α_i, corresponding to K_1, K_2, $\vec{H}$, and $\vec{M}$, are defined with respect to the ripple direction. Since this direction corresponds to the easy axis of the uniaxial anisotropy (see below), $\alpha_{K_2} = 0$. The mutual angle $\angle(K_1, K_2)$ is then only given by α_{K_1}. For the calculation of the magnetization reversal curves the perfect-delay convention is used, i.e., the magnetization remains in a local-energy minimum until the energy barrier between local and global energy minimum vanishes.

Experimentally α_{K_1} is set by applying a magnetic field of 2 kOe along different directions during a field annealing cycle. Three different configurations are discussed in the present Rapid Communication. In order to achieve a complete comparison between experimental and theoretical magnetization reversal curves a special graphical data representation is chosen. The longitudinal magnetization component is displayed color coded ($-M$: black; $+M$: white). A single hysteresis curve is displayed as a vertical line from $-H \rightarrow +H \rightarrow -H$ as indicated in Fig. 2. The experimental data are

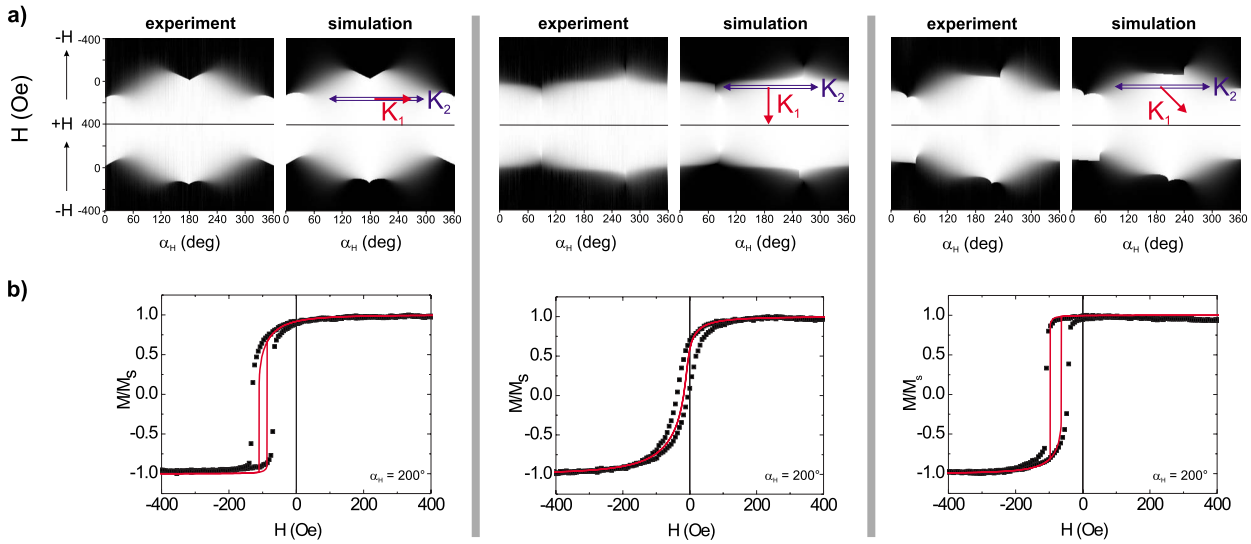

FIG. 2. (Color online) (a) Angular dependence of the magnetization reversal behavior for three different configurations (left: $\alpha_{K_1} = 1°$; middle: $\alpha_{K_1} = 86°$; right: $\alpha_{K_1} = 41°$) as sketched. In each case the left (right) image corresponds to the experimental data (simulation). The longitudinal magnetization component is displayed color coded ($-M$: black; $+M$: white). One image contains 360 hysteresis curves. (b) Conventional plots of the measured (full symbols) and simulated (line) magnetization reversal curves for $\alpha_H = 200°$ for the different configurations shown above.

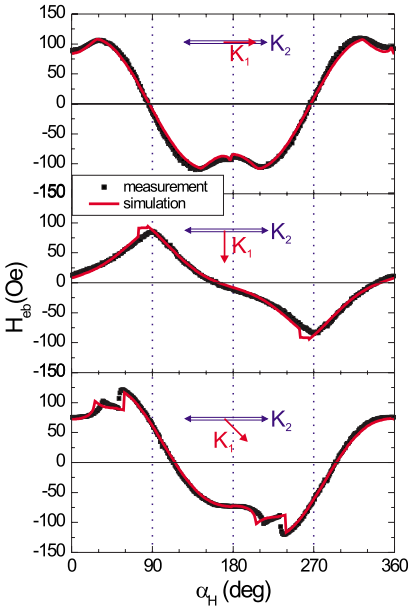

FIG. 3. (Color online) Angular dependence of H_{eb} (experiment: full symbols; simulation: line) for the same configurations as in Fig. 2 (top: $\alpha_{K_1}=1°$; middle: $\alpha_{K_1}=86°$; bottom: $\alpha_{K_1}=41°$).

obtained by means of longitudinal magneto-optic Kerr effect measurements.

The whole angular dependence of the magnetization reversal curves, measured and simulated, are shown in Fig. 2(a) for three different configurations of K_1 with respect to K_2, i.e., $\alpha_{K_1}=0°,90°,45°$. For all simulations the same anisotropy constants $K_1=7.9\times10^4$ erg/cm^3 and $K_2=2.8\times10^4$ erg/cm^3 are used. The only free parameter in the simulations is the mutual angle between both anisotropy contributions α_{K_1}, which has been set to 1° (left column), 86° (middle column), and 41° (right column), respectively. The small deviations in α_{K_1} from the nominal values are attributed to a misalignment during the field annealing procedure, which causes slight asymmetries in the angular dependence. With these values of anisotropy and α_{K_1} a perfect agreement between the experimental data and the numerical simulations is obtained simultaneously for all three configurations and also the experimental asymmetries are well reproduced. In addition, in Fig. 2(b) the measured and simulated magnetization reversal curves are shown for an in-plane angle of $\alpha_H=200°$ in a conventional way. Although both coercive fields are underestimated by the model in general, the exchange bias field, i.e., the loop shift, is reproduced perfectly. Its angular dependence, which has been extracted from the experimental and simulated magnetization reversal curves of Fig. 2, is shown in Fig. 3. Also this data representation demonstrates the perfect agreement between experimental data and the simulated angular dependence. The origin of minimal discrepancies are asymmetric deviations in coercivity. However, since no nucleation and domain-wall motion processes are considered in our model, the degree of congruence is still stunning.

The present results demonstrate that both anisotropy contributions are superimposed independently and that no interTABLE I. Unidirectional K_1 and uniaxial K_2 anisotropy contributions of exchange bias films deposited either on a flat or a rippled Si substrate. To further characterize the substrates the corresponding maximum step densities are given.

	Flat	Rippled
Step density (steps/nm)	$\leqslant 0.01$	≈ 0.7
Step distance (atomic units)	$\geqslant 500$	≈ 7
K_1 (erg/cm^3)	6.6×10^4	7.9×10^4
K_2 (erg/cm^3)	2.5×10^3	2.8×10^4

correlation between them is present. Furthermore, this also proves that dipolar effects arising from the film morphology exhibit only a negligible contribution to the unidirectional anisotropy and thus to the exchange bias effect. For a given interfacial roughness or step density the direction of the unidirectional anisotropy does not influence its magnitude. However, this finally leads to the question of whether the unidirectional anisotropy is influenced by the amount of interfacial roughness at all.

In order to address this issue, the same layer stack was deposited on a flat Si(001) substrate which has not been treated by ion erosion. After deposition both anisotropy constants have been determined using the same procedure as described above. In Table I the different anisotropy contributions are compared. The uniaxial anisotropy depends strongly on the step density and an increase by more than a factor of 10 is observed. In principle, this enhancement can have different microscopic origins: (i) dipolar effects due to the generation of stray fields,[21,22] or (ii) step-edge anisotropies due to reduced atomic coordination originating from spin-orbit coupling.[23,24] Based on Schlömann's theory[21] the dipolar contribution of one rough surface can be calculated by

$$K_2^{dip} = 2\pi M^2 \frac{\pi w^2}{\lambda D}$$

with w the rms roughness (0.74 nm), λ the periodicity (32 nm), and D the film thickness (9 nm). Using the experimental values we obtain $K_2^{dip}=2.8\times10^4$ erg/cm^3, exactly the value determined experimentally. However, since two interfaces are involved the calculated K_2^{dip} is even larger than K_2. In any case, it becomes immediately clear that the dipolar contribution governs the uniaxial anisotropy. In contrast to epitaxial systems,[16] the step-edge anisotropies are negligibly small. This can be understood considering the fact that the grains are oriented randomly in-plane and that consequently the step-edge orientation is random. The possible anisotropies arising from the step edges are thus canceled to a large extent.

In addition to the uniaxial anisotropy, also the unidirectional anisotropy is increased which can be attributed to an enhancement of uncompensated spins at the interface for a rippled interface with respect to a flat one. This is exactly what is expected[11] if a compensated antiferromagnet is considered. For uncompensated antiferromagnets a decrease in unidirectional anisotropy is predicted.[11] For the FeMn sys-

tem investigated here it is agreed that the magnetic ground state is the $3Q$ noncollinear magnetic structure, in which the magnetic moments align toward the center of the unit cell and thus create an ideally compensated antiferromagnetic material.[25,26] Consequently, the observed increase in unidirectional anisotropy is in full agreement with theoretical predictions.

In summary we have demonstrated that a ripple structure gives rise to an increase of both unidirectional and uniaxial anisotropy contributions in exchange bias systems in agreement with theoretical predictions. However, the origin of the increase is different for both cases; dipolar effects (uniaxial anisotropy) and uncompensated spins (unidirectional anisotropy). Since the direction of the unidirectional anisotropy can be set along any in-plane direction with its magnitude remaining unchanged intercorrelation effects between both anisotropies can be ruled out. The magnetization reversal behavior can be perfectly reproduced by an extended coherent rotation model for all different configurations simultaneously with one parameter set only.

The authors thank J. McCord for the critical reading of the manuscript. M.O.L. acknowledges the financial support from the European Communities Human Potential Program NEXBIAS under Contract No. HPRN-CT2002-00296.

*j.fassbender@fzd.de

[1] J. Nogues and I. K. Schuller, J. Magn. Magn. Mater. **192**, 203 (1999).
[2] R. L. Stamps, J. Phys. D **33**, R247 (2000).
[3] S. Riedling, M. Bauer, C. Mathieu, B. Hillebrands, R. Jungblut, J. Kohlhepp, and A. Reinders, J. Appl. Phys. **85**, 6648 (1999).
[4] T. Mewes, H. Nembach, M. Rickart, S. O. Demokritov, J. Fassbender, and B. Hillebrands, Phys. Rev. B **65**, 224423 (2002).
[5] H. Xi, T. F. Ambrose, T. J. Klemmer, R. van de Veerdonk, J. K. Howard, and R. M. White, Phys. Rev. B **72**, 024447 (2005).
[6] D. Y. Kim, C. G. Kim, C.-O. Kim, M. Shibata, M. Tsunoda, and M. Takahashi, IEEE Trans. Magn. **41**, 2712 (2005).
[7] S. Dubourg, J. F. Bobo, B. Warot, E. Snoeck, and J. C. Ousset, Phys. Rev. B **64**, 054416 (2001).
[8] J. Camarero, J. Sort, A. Hoffmann, J. M. Garcia-Martin, B. Dieny, R. Miranda, and J. Nogues, Phys. Rev. Lett. **95**, 057204 (2005).
[9] A. Hoffmann, M. Grimsditch, J. E. Pearson, J. Nogues, W. A. A. Macedo, and I. K. Schuller, Phys. Rev. B **67**, 220406(R) (2003).
[10] S. H. Chung, A. Hoffmann, and M. Grimsditch, Phys. Rev. B **71**, 214430 (2005).
[11] J.-V. Kim, R. L. Stamps, B. V. McGrath, and R. E. Camley, Phys. Rev. B **61**, 8888 (2000).
[12] C. Liu, C. Yu, H. Jiang, L. Shen, S. Alexander, and G. J. Mankey, J. Appl. Phys. **87**, 6644 (2000).
[13] K. Nakamura, A. J. Freeman, D.-S. Wang, L. Zhong, and J. Fernandez-de-Castro, Phys. Rev. B **65**, 012402 (2001).
[14] J. Erlebacher, M. J. Aziz, E. Chason, M. B. Sinclair, and J. A. Floro, Phys. Rev. Lett. **82**, 2330 (1999).
[15] B. Ziberi, F. Frost, Th. Höche, and B. Rauschenbach, Phys. Rev. B **72**, 235310 (2005).
[16] R. Moroni, D. Sekiba, F. Buatier de Mongeot, G. Gonella, C. Boragno, L. Mattera, and U. Valbusa, Phys. Rev. Lett. **91**, 167207 (2003).
[17] D. Sekiba, R. Moroni, G. Gonella, F. Buatier de Mongeot, C. Borgano, L. Mattera, and U. Valbusa, Appl. Phys. Lett. **84**, 762 (2004).
[18] F. Bisio, R. Moroni, F. Buatier de Mongeot, M. Canepa, and L. Mattera, Phys. Rev. Lett. **96**, 057204 (2006).
[19] A. L. Dantas, G. O. G. Reboucas, A. S. W. T. Silva, and A. S. Carrico, J. Appl. Phys. **97**, 10K105 (2005).
[20] E. C. Stoner and E. P. Wohlfarth, Philos. Trans. R. Soc. London, Ser. A **240**, 599 (1948).
[21] E. Schlömann, J. Appl. Phys. **41**, 1617 (1970).
[22] Y.-P. Zhao, G. Palasantzas, G.-C. Wang, and J. Th. M. De Hosson, Phys. Rev. B **60**, 1216 (1999).
[23] P. Gambardella, A. Dallmeyer, K. Maiti, M. C. Malagoli, W. Eberhardt, K. Kern, and C. Carbone, Nature (London) **416**, 301 (2002).
[24] S. Rusponi, T. Cren, N. Weiss, M. Epple, P. Buluschek, L. Claude, and H. Brune, Nat. Mater. **2**, 546 (2003).
[25] K. Nakamura, T. Ito, A. J. Freeman, L. Zhong, and J. Fernandez-de-Castro, Phys. Rev. B **67**, 014405 (2003).
[26] T. Mewes, B. Hillebrands, and R. L. Stamps, Phys. Rev. B **68**, 184418 (2003).

APPLIED PHYSICS LETTERS **91**, 062107 (2007)

Suppression of secondary phase formation in Fe implanted ZnO single crystals

K. Potzger,[a] Shengqiang Zhou, H. Reuther, K. Kuepper, G. Talut, M. Helm, and J. Fassbender
Institute of Ion Beam Physics and Materials Research, Forschungszentrum Dresden-Rossendorf, P.O. Box 510119, 01314 Dresden, Germany

J. D. Denlinger
Advanced Light Source, Lawrence Berkeley National Laboratory, Berkeley, California 94720

(Received 11 April 2007; accepted 12 July 2007; published online 7 August 2007)

Unwanted secondary phases are one of the major problems in diluted magnetic semiconductor creation. Here, the authors show possibilities to avoid such phases in Fe implanted and postannealed ZnO(0001) single crystals. While α-Fe nanoparticles are formed after such doping in as-polished crystals, high temperature (1273 K) annealing in O_2 or high vacuum before implantation suppresses these phases. Thus, the residual saturation magnetization in the preannealed ZnO single crystals is about 20 times lower than for the as-polished ones and assigned to indirect coupling between isolated Fe ions rather than to clusters. © *2007 American Institute of Physics*.
[DOI: 10.1063/1.2768196]

Diluted magnetic semiconductors (DMSs) such as transition metal (TM) doped ZnO have recently attracted huge attention due to their application potential in spintronics.[1,2] Especially for rather easy available *n*-type ZnO, TM dopants such as Fe or Co but not Mn are theoretically predicted to yield ferromagnetic coupling.[2] One of the major drawbacks in preparation is the unwanted formation of magnetic secondary phases for high TM concentrations (~5%) necessary[3–5] mimicking a room-temperature DMS. In this letter, we show that unwanted secondary phases in ZnO single crystals implant doped with Fe can be avoided by annealing the crystals prior to implantation. Moreover, weak ferromagnetic properties are introduced that are not related to ordinary superparamagnetic nanoparticles. Thus, the following sample set has been prepared from hydrothermal, commercial epipolished ZnO(0001) substrates purchased from Crystec: (1) nonpreannealed, i.e., as polished, (2) O_2 preannealed in flowing O_2 at 1273 K for 15 min, and (3) vacuum preannealed in high vacuum (base pressure $<1\times10^{-6}$ mbar) at 1273 K for 15 min. O_2 annealing at high temperatures is known to reduce lattice damage in the near surface region of ZnO.[6,7] Vacuum annealing (3), was chosen due to the formation of point defects that might mediate indirect ferromagnetic coupling of the implanted ions.[8–10] Note that mild vacuum annealing around 873 K usually introduces both O vacancies and Zn interstitials.[11] After high temperature annealing, however, Zn interstitials are not stable, i.e., the defects are dominated by oxygen vacancies.[12] Following that paper, oxygen vacancies are not expected to mediate ferromagnetic coupling, while Zn interstitials are. Thus, our approach, in addition to the suppression of secondary phases, would give a confirmation of these different effects of various kinds of defects for the case of Fe doping. For further processing, our samples were subjected to ^{57}Fe ion implantation. The implantation energy was 80 keV at an incident angle of 7° yielding a projected range of 38 nm and a straggling of 17 nm (TRIM). The implanted Fe fluence of 2×10^{16} cm^{-2} yielded a maximum atomic concentration of 5%. In order to avoid magnetic secondary phases already in the as-implanted samples, a low implantation temperature of 253 K was used.[3] Postimplantation annealing for lattice recovery was performed in high vacuum at a temperature of 823 K for 15 min. The base pressure was below 1×10^{-6} mbar. The particular parameters for the postannealing have been chosen to avoid long-range diffusion and oxidation of the implanted Fe as have been observed earlier for higher annealing temperatures.[4] For a detailed analysis we applied x-ray diffraction (XRD) using a Siemens D 5005 diffractometer equipped with a Göbel mirror for enhanced brilliance, Rutherford backscattering/channeling (RBS/C), atomic force microscopy (AFM), conversion electron Mössbauer spectroscopy (CEMS) at room temperature, x-ray absorption spectroscopy (XAS) performed at beam line 8.0.1 of the Advanced Light Source in Berkeley, and superconducting quantum interference device (SQUID) magnetometry with the magnetic field applied parallel to the sample surface. RBS/C revealed no significant change of the crystallinity after preannealing. In contrast, AFM (not shown) reveals pronounced changes of the crystal surface morphology. After O_2 preannealing, the root mean square surface roughness (R_q) of the ZnO sample slightly increases from 0.23 to 0.27 nm and regularly oriented steps appear. The latter is an indication for surface recrystallization.[7] Vacuum preannealing, in contrast, yielded a surface roughness of 23 nm. While after implantation a slight increase of R_q is detectable, postannealing does not change R_q significantly for any of the samples. RBS/C for both the preannealed and nonpreannealed crystals [Fig. 1(a)] shows a decrease of the minimum channeling yield (χ_{min}) with postannealing. The drop is largest for the nonpreannealed crystal and smallest for the vacuum preannealed sample. The lowest χ_{min} is achieved for the O_2 preannealed crystal. χ_{min} directly reflects the crystalline homogeneity, i.e., while an amorphous sample shows a χ_{min} of 100%, a perfect single crystalline sample exhibits 1%–2%. Diffusion of the implanted Fe due to postannealing could be ruled out by means of RBS/C random spectra [Fig. 1(b)]. Bumps origi-

[a]Electronic mail: k.potzger@fzd.de

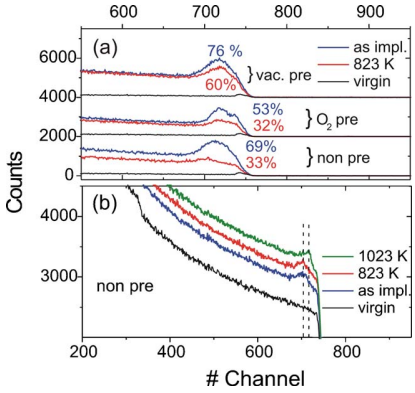

FIG. 1. (Color online) (a) Channeling RBS spectra for the as-implanted and postannealed ZnO single crystals. Preimplantation annealing is indicated. The χ_{min} value for every spectrum is given in %. (b) Exemplary random spectra for the nonpreannealed crystal for different postannealings. Fe is visible in the random spectra as a bump. All spectra have been shifted in y direction for better clarity.

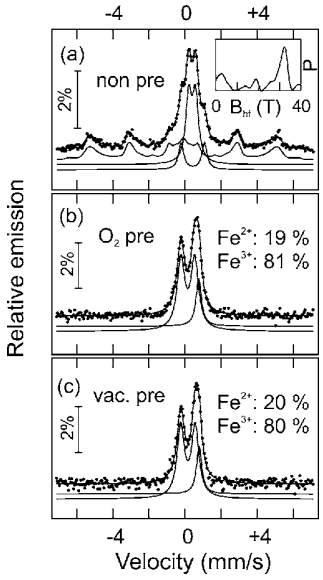

FIG. 2. CEM spectra and least squares fits with Lorentzian lines (see Ref. 15) of the Fe implanted and postannealed ZnO single crystals. (a) Nonpreannealed crystal with pronounced magnetic hyperfine field corresponding to α-Fe. The ratio between Fe^0 and Fe^{3+} is 48%:52%, respectively. [(b) and (c)] CEM spectra of the preannealed samples. The ratio between the valence states is indicated.

nating from the implanted Fe are visible in all samples that allow us to investigate the potential diffusion of the Fe inside ZnO. Upon postannealing at 823 K these bumps do not shift, i.e., Fe is not segregating over larger distances. In order to check the potential formation of secondary phases, XRD of the implanted and postannealed samples has been performed. The presence of secondary phases has only been observed for the nonpreannealed and postannealed crystal (not shown), i.e., α-Fe nanoparticles of 7 nm mean diameter, as calculated using the Scherrer formula.[13]

In order to further prove that metallic nanoparticle formation has been avoided by our preannealing, element specific spectroscopy was applied. We performed CEMS and XAS, respectively. While CEMS is more bulk sensitive, XAS recording the total electron yield is rather sensitive to the surface region. The combination of both methods thus leads to a complete picture of the charge states of the implanted Fe. Moreover, CEMS allows simultaneous detection of electronic and magnetic properties at the nucleus of the implanted Fe. The CEM spectra of the as-implanted samples (not shown) look similar exhibiting mixed Fe^{2+} and Fe^{3+} valence states. No magnetic sextet was detected for any of the samples. Thus, they are comparable to the ones from earlier work.[3,14] Figure 2 shows CEM spectra for all the postannealed samples. Only the nonpreannealed one shows a magnetic hyperfine field with an isomer shift equal to that of α-Fe. The value of the magnetic hyperfine field is distributed over a wide range so that it can be assumed that a large part of the Fe ions also does not contribute to the full magnetic bulk moment. In contrast, no indication for metallic Fe exists in the spectra of the preannealed samples. They show similar hyperfine parameters dominated by a Fe^{3+} doublet. Please note that after postannealing, Fe^{2+} states are only present for the preannealed crystals but not for the nonpreannealed ones. The XAS measurements of the postannealed samples yield similar results (Fig. 3), i.e., ionic 2^+ and 3^+ valence states in all of the crystals with a contribution from metallic Fe solely in the nonpreannealed sample. Also for the O_2 preannealed sample we find a good coincidence between the Mößbauer and XAS data. That is, from the multiplet structure of the corresponding Fe $L_{2,3}$ XAS (third spectrum from the top in Fig. 3) one can conclude that Fe^{3+} ions are dominating in this sample, whereas the presence of some Fe^{2+} ions cannot be excluded. We find quite good agreement with the Fe $L_{2,3}$ XAS of Fe_3O_4 comprising 66.7% Fe^{3+} and 33.3% of Fe^{2+} ions. On the other hand, we find some differences in detail in the case of the vacuum preannealed crystal. The bulk sensitive CEMS suggests a very similar valence state than for the O_2 preannealed sample, dominated by Fe^{3+} ions. The more surface sensitive XAS also suggests a mixed valence state, however, involving some more Fe^{2+} than Fe^{3+} states. The XAS of the O_2 preannealed sample is very similar to that of a Sr_2FeMoO_6 sample which has been found to have a mixed iron valence state involving around 65% Fe^{2+} ions and 35% Fe^{3+} ions.[16] This discrepancy could be explained by different spatial distributions of the charge states for the different preannealing conditions. From this analysis, we conclude that

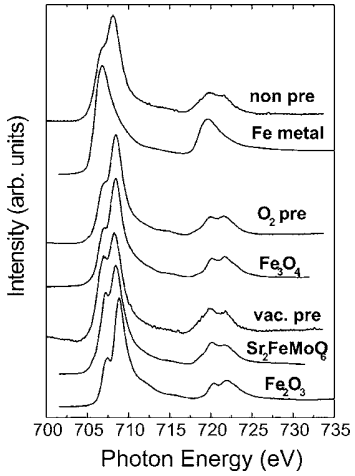

FIG. 3. Fe $L_{2,3}$ XAS of the nonpreannealed sample (top) and the two preannealed samples (third and fifth from the top) after implantation and postannealing. Several measurements on reference compounds, namely, Fe metal, Fe_2O_3, Fe_3O_4, and Sr_2FeMoO_6 are also shown for comparison (see Refs. 16 and 18). These spectra allow a qualitative determination of the Fe charge states in the ZnO samples. Please note that only the nonpreannealed sample shows pronounced contributions from metallic Fe.

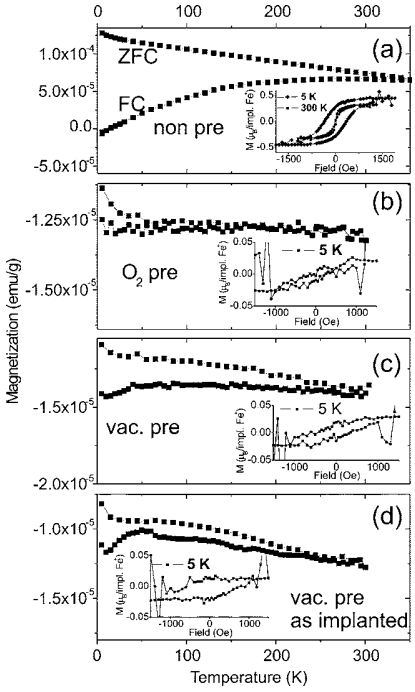

FIG. 4. ZFC-FC magnetization vs temperature measurements and magnetic hysteresis loops (insets) for all Fe implanted and postannealed ZnO single crystals [(a)–(c)]. The ZFC curves were obtained by cooling the sample from 300 down to 5 K in zero field and subsequently annealing it back to 300 K in 50 Oe field. The FC curves were obtained during subsequent cooling of the sample down to 5 K in a 50 Oe field. For the insets, the diamagnetic background was subtracted. (a) Nonpreannealed sample exhibiting α-Fe nanoparticles [(b) and (c)] O_2- and vacuum preannealed crystals after postannealing. (d) As-implanted vacuum preannealed crystal (for comparison). The latter three show a weak separation in the ZFC-FC and very low saturation moment in the hysteresis loops, as compared to (a). For (c) and (d), the thermomagnetic irreversibility temperature is above 250–300 K.

nanoparticle formation is suppressed by both preannealing methods. The mechanism of the suppression is not yet completely clear. Removal of defects acting as nucleation centers or introduction of defects immobilizing the Fe ions might be an explanation.

The magnetic properties were analyzed by means of SQUID magnetometry. The hydrothermally grown virgin samples are purely diamagnetic with a susceptibility of -2.6×10^{-7} emu/g Oe. This value is consistent with the one observed by Quesada *et al.*,[17] i.e., -1.62×10^{-7} emu/g Oe. The difference might originate from the much different preparation method of the ZnO samples by this group. Pronounced ferromagnetic properties were only found for the nonpreannealed crystal after postannealing [Fig. 4(a)]. Magnetization reversal and zero field cooled (ZFC)/field cooled (FC) temperature dependence measurements recorded at 50 Oe show typical behavior of superparamagnetic nanoparticles with size distribution.[4] The nonpreannealed and the O_2 preannealed crystals do not show magnetic ordering for the as-implanted state (not shown). In contrast, after postannealing a weak separation between ZFC and FC curves up to 70 K can be observed for the O_2 preannealed crystal and up to a temperature above 250 K for the vacuum preannealed crystal [Figs. 4(b) and 4(c)]. Note that weak ferromagnetic properties occur already after implantation for the vacuum preannealed crystal [Fig. 4(d)]. The saturation magnetization extracted from hysteresis loops recorded at 5 K is below $0.025\mu_B$ per implanted Fe ion. As compared to α-Fe the magnetic moment per implanted Fe ion is about 20 times smaller than the as-purchased crystal after postannealing. The shape of the ZFC-FC curve could be explained assuming regions with inhomogeneous Fe content as can be expected from the low temperature implantation. Postannealing, however, smoothes the ZFC-FC curve. The origin of the observed ferromagnetic properties is rather speculative at this point. First, due to the very low saturation magnetization achieved, we conclude that a large amount of defects created by high temperature annealing, probably oxygen vacancies, do not lead to pronounced ferromagnetic coupling of the implanted Fe ions. Second, it is rather likely that implantation or implantation plus mild postannealing creates such kind of defects, which lead to ferromagnetic properties of the Fe implanted ZnO. One possibility is the coupling of a small part of the Fe ions via Zn interstitials.

In summary, we demonstrated that preannealing of commercial ZnO(0001) single crystals in both flowing O_2 or vacuum suppresses metallic secondary phase formation after Fe implantation and mild postannealing in contrast to the nonpreannealed crystals. Weak ferromagnetic properties are induced in the vacuum preannealed crystals. These properties cannot be associated with ordinary superparamagnetic nanoparticles but could be due to indirect coupling mediated by point defects.

[1] S. A. Wolf, D. D. Awschalom, R. A. Buhrman, J. M. Daughton, S. von Molnár, M. L. Roukes, A. Y. Chtchelkanova, and D. M. Treger, Science **294**, 1488 (2001).
[2] K. Sato and H. Katayama-Yoshida, Semicond. Sci. Technol. **17**, 367 (2002).
[3] K. Potzger, Shengqiang Zhou, H. Reuther, A. Mucklich, F. Eichhorn, N. Schell, W. Skorupa, M. Helm, J. Fassbender, T. Herrmannsdörfer, and T. P. Papageorgiou, Appl. Phys. Lett. **88**, 052508 (2006).
[4] Shengqiang Zhou, K. Potzger, H. Reuther, G. Talut, F. Eichhorn, J. von Borany, W. Skorupa, M. Helm, and J. Fassbender, J. Phys. D **40**, 964 (2007).
[5] X. X. Wei, C. Song, K. W. Geng, F. Zeng, B. He, and F. Pan, J. Phys.: Condens. Matter **18**, 7471 (2006).
[6] T. Monteiro, C. Boemare, M. J. Soares, E. Rita, and E. Alves, J. Appl. Phys. **93**, 8995 (2003).
[7] S. Graubner, C. Neumann, N. Volbers, B. K. Meyer, J. Bläsing, and A. Krost, Appl. Phys. Lett. **90**, 042103 (2007).
[8] J. M. D. Coey, M. Venkatesan, and C. B. Fitzgerald, Nat. Mater. **4**, 173 (2005).
[9] K. R. Kittilstved, W. K. Liu, and D. R. Gamelin, Nat. Mater. **5**, 291 (2006).
[10] D. A. Schwartz and D. R. Gamelin, Adv. Mater. (Weinheim, Ger.) **16**, 2115 (2004).
[11] X. Q. Wei, B. Y. Man, M. Liu, C. S. Xue, H. Z. Zhuang, and C. Yang, Physica B **388**, 145 (2007).
[12] M. H. F. Sluiter, Y. Kawazoe, P. Sharma, A. Inoue, A. R. Raju, C. Rout, and U. V. Waghmare, Phys. Rev. Lett. **94**, 187204 (2005).
[13] B. D. Cullity, *Elements of X-Ray Diffraction* (Addison-Wesley Reading, MA, 1978), Vol. 1, p. 102.
[14] K. Potzger, W. Anwand, H. Reuther, Shengqiang Zhou, G. Talut, G. Brauer, W. Skorupa, and J. Fassbender, J. Appl. Phys. **101**, 033906 (2007).
[15] R. Brand, Nucl. Instrum. Methods Phys. Res. B **28**, 398 (1987).
[16] K. Kuepper, I. Balasz, H. Hesse, A. Winiarski, K. C. Prince, M. Matteucci, D. Wett, R. Szargan, E. Burzo, and M. Neumann, Phys. Status Solidi A **201**, 3252 (2004).
[17] A. Quesada, M. A. García, M. Andrés, A. Hernando, J. F. Fernández, A. C. Caballero, M. S. Martín-González, and F. Briones, J. Appl. Phys. **100**, 113909 (2006).
[18] K. C. Prince, M. Matteucci, K. Kuepper, S. G. Chiuzbaian, S. Bartkowski, and M. Neumann, Phys. Rev. B **71**, 085102 (2005).

APPLIED PHYSICS LETTERS **90**, 044105 (2007)

Thin film patterning by surface-plasmon-induced thermocapillarity

Lars Röntzsch[a] and Karl-Heinz Heinig
Institute of Ion Beam Physics and Materials Research, Research Center Dresden-Rossendorf, P.O. Box 51 01 19, 01314 Dresden, Germany

Jon A. Schuller and Mark L. Brongersma
Geballe Laboratory of Advanced Materials, Stanford University, 476 Lomita Mall, Stanford, California 94305

(Received 18 September 2006; accepted 14 December 2006; published online 22 January 2007)

It is reported that standing surface-plasmon-polariton (SPP) waves can cause regular thickness undulations of thin polymethyl methacrylate (PMMA) films above a metallic substrate. Ripples, rings, and hillock arrays with long-range order were found. Numerical calculations reveal that periodic in-plane temperature profiles are generated in the PMMA due to the nonradiative damping of SPP interference patterns. Computer simulations on the temperature-gradient-driven mass transport confirm that thermocapillarity is the dominating mechanism of the observed surface patterning. © *2007 American Institute of Physics*. [DOI: 10.1063/1.2432282]

In the course of miniaturization of functional structures capillary effects have become increasingly important due to the large surface-to-volume ratio at the micro- and nanoscale. This principle applies equally to systems in the liquid[1] and in the solid state.[2,3] The difference lies in the microscopic kinetics of these systems: hydrodynamic flow on the one hand and atomic diffusion on the other. If a system is left to itself, capillarity-driven processes lead to surface free energy minimization; thus, the morphology of functional structures may strongly change in a self-organizing manner.[1–3] On the contrary, if a system is exposed to external forces it can be driven to a nonequilibrium state. Thermal gradients for instance give rise to thermocapillary forces which trigger a biased material flux.[4] If these gradients are periodic in space, long-range-ordered structures can be achieved.

In this letter, we report on a method to fabricate long-range-ordered thickness undulations in thin polymethyl methacrylate (PMMA) films on metals. This method, which uses periodic in-plane temperature fields induced by the damping of surface plasmon polaritons (SPPs), was previously used to characterize SPP propagation and scattering.[5] Here, experiments and numerical calculations are performed to further elucidate the underlying mechanisms for creating the observed thickness undulations. Reflection pole method (RPM) calculations[6] are used to determine the spatially dependent power losses generated by SPPs excited at a PMMA/Au interface. These losses give rise to local heating. Taking these losses as a spatially varying heat source, heat conduction calculations show that periodic temperature fields, which result in thermocapillary effects in the PMMA, are produced. Kinetic Monte Carlo (KMC) simulations reveal that such in-plane thermal gradients trigger a biased material transport. It is expected that this nonequilibrium fabrication method of SPP lithography can be applied to other thin film systems (particularly thin polymer films) in order to achieve regular thickness undulations with long-range order.

In Fig. 1, sample structure and experimental procedure are drawn schematically. A 50 nm thick patterned metal film (45 nm Au, 5 nm Ti sticking layer) was deposited on a Si(001) wafer (500 μm thick). Afterwards, a 1 μm thick 495 000 molecular weight PMMA film was spin coated over the whole wafer. The samples were then exposed for 1 s to CO_2 laser light ($\lambda = 10.64$ μm) at room temperature (RT). The 5 W quasi-continuous-wave[7] linearly polarized laser beam ($\mathbf{E} = E\mathbf{e}_x$) was focused to a spot of approximately 200 μm diameter, illuminating the patterned Au structures at normal incidence. After laser irradiation, surface profiles were imaged with differential image contrast (DIC) and atomic force microscopy.

In Fig. 2(a), a DIC micrograph that clearly indicates a ripple structure on the PMMA is shown. The periodic ripples only occur above the rectangular Au pads (region "B" in Fig. 1). In those areas with no Au beneath the PMMA (region "A" in Fig. 1), no periodic PMMA surface roughening is observed after laser irradiation. The ripple pattern is only periodic along the direction of laser polarization $\mathbf{e}_x$ as expected for a standing wave arising from a transverse magnetic (TM) guided mode. The location (above Au) and observed polarization dependence (TM) strongly suggest that the ripple patterns are caused by SPPs. Furthermore, our electromagnetic simulations based on RPM calculations[6] show that the structure supports a SPP mode with a wavelength of 10.2 μm but no other waveguide modes. That SPPs induce the ripple structure becomes even more evident in the case of more exotic SPP interference patterns which are observed when Au pads of different geometries are illuminated [Figs. 2(b) and 2(c)]. The excitation of SPPs at curved or angled interfaces results in circular and triangular interference patterns that induce annular and hillock patterns on the PMMA surface, respectively.

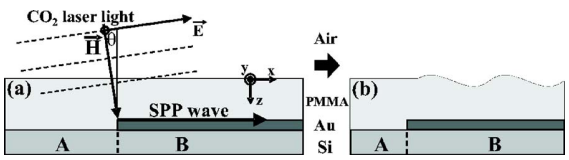

FIG. 1. Schematic drawing of (a) sample setup, experimental procedure, and (b) the periodic surface pattern obtained.

[a]Electronic mail: l.roentzsch@fzd.de

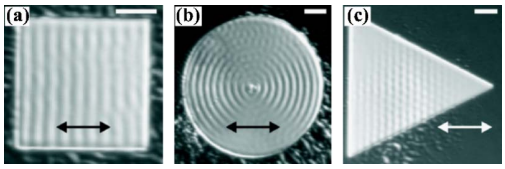

FIG. 2. DIC micrographs showing periodic PMMA surface patterns: (a) ripples, (b) rings, and (c) hillocks. The arrows are parallel to $\mathbf{e}_x$. The white scale bars denote 30 μm.

Since the SPPs are excited from the edges of the Au pad, the optical field is given by (ignoring SPP reflections) $\mathbf{E}_{\text{tot}}=[\mathbf{E}_i(z)+\mathbf{E}_l(z)e^{-ikx}+\mathbf{E}_r(z)e^{+i(kx+\delta)}]e^{-i\omega t}$, where $\mathbf{E}_i(z)$ corresponds to the standing wave produced by the incident laser reflected off the Au surface, $\mathbf{E}_{l,r}(z)$ are the SPPs excited at the left and the right edge of the structure, k is the SPP wave vector, and δ is the phase shift between the incident and SPP field. The damping of the optical field is given by $\partial u/\partial t=\omega\times\Im(\varepsilon)\times 1/2\Re(\mathbf{E}_{\text{tot}}\cdot\mathbf{E}_{\text{tot}}^{*})$, where u is the electromagnetic energy density.[8] With the above equation for $\mathbf{E}_{\text{tot}}$ the loss contains terms, which are only z dependent, and interference terms, which have a periodicity along $\mathbf{e}_x$. Interference of the two counterpropagating SPPs with each other and with the incident laser result in periodicities with wavelengths of $1/2\lambda_{\text{SPP}}$ and λ_{SPP}, respectively. The measured ripple patterns on rectangular Au pads have a peak-to-trough distance of approximately 40 nm and a periodicity of 10.7 ± 0.4 μm. We attribute the measured periodicity to interference of the incident laser with SPPs. The deviation of the measured periodicity from the calculated SPP wavelength ($\lambda_{\text{SPP}}=10.2$ μm) may be caused by off normal rays in the focused laser spot. The lack of a ripple pattern with a periodicity of $1/2\lambda_{\text{SPP}}$ is consistent with weak coupling to the SPPs ($E_i \gg E_{l,r}$). In Fig. 3, the losses in the PMMA and the Au layer are plotted assuming that 1% of the incident laser power is coupled to SPPs. Although the actual coupling is unknown, later it is shown that this estimation recaptures the qualitative features of the experiment. The optical absorption coefficient of PMMA at a wavelength of 10.6 μm, $\alpha_{\text{PMMA}}=0.04$ μm^{-1}, was used.[9]

The calculated nonradiative damping of the optical fields was taken as the heat source $S(x,z)$ in a steady-state heat conduction calculation to determine the spatially dependent temperature profile in the PMMA. The resultant heat conduction equation, $\nabla(\lambda_i\nabla T)=S(x,z)$, has been solved numerically by a finite element method. Here, λ_i denotes the heat conductivity of the ith material.[10] The heat source term is given by $S(x,z)=S_{\text{inc}}(z)+S_{\text{SPP}}(z)+S_{\text{int}}(x,z)$, where S_{inc} and S_{SPP} are the losses due to the incident field and the SPP, respectively.

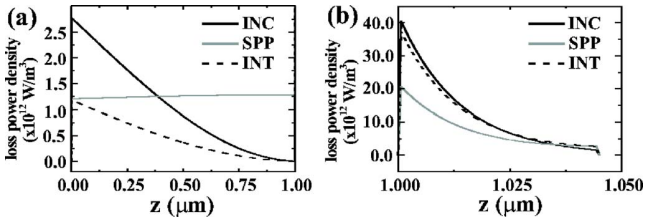

FIG. 3. Power loss densities of the optical field (a) in the PMMA and (b) in the Au according to RPM calculations. The PMMA surface and the PMMA-Au interface are located at $z=0.0$ μm and $z=1.0$ μm, respectively. The losses (INC), (SPP), and (INT) are due to the incident field, the SPP, and the interference between the incident wave and the SPP.

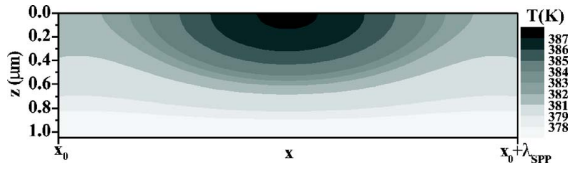

FIG. 4. Stationary temperature field in the PMMA resulting from a heat conduction calculation assuming 1% coupling to the SPP and T=RT at the upper and lower boundary of the layer stack 1 mm air/1 μm PMMA/50 nm Au/500 μm Si/0.5 μm air (see Ref. 14). The air-PMMA interface is located at $z=0$. The T profile in air and in the substrate is not plotted.

S_{int} denotes the loss that is periodic along $\mathbf{e}_x$ with a wavelength of λ_{SPP} due to damping of the SPP/incident laser interference pattern. In Fig. 4, the stationary temperature field for one period of λ_{SPP} is shown for the case of a 1% coupling to the SPP. Here, a mean temperature in the PMMA of 382 K is achieved; this is slightly above the PMMA glass transition temperature at 378 K.[11] The lateral temperature gradient at the PMMA surface is about 1 K/μm. Taking into account the PMMA surface tension, $\sigma_{\text{PMMA}}=4.11\times10^{-2}$ N m^{-1} (at 20 °C),[12] and its temperature coefficient, $d\sigma/dT=-7.6\times10^{-5}$ Nm^{-1} K^{-1},[12] it can be estimated that $d\sigma/dx=d\sigma/dT\times dT/dx=76$ N/m^2. This surface tension gradient causes the PMMA to flow from hot to cold regions resulting in thickness undulations. In the undulated PMMA layer, the Laplace pressure, $p=\kappa\sigma$, where κ is the local curvature and σ is the local surface tension, has to be position independent in the stationary regime: $\kappa d\sigma/dx+\sigma d\kappa/dx=0$. With the approximation $\kappa\approx d^2h/dx^2$, where $h(x)$ describes the surface profile, we get $d^3h/dx^3=-d^2h/dx^2\pi\Delta T/(\lambda\sigma)\times d\sigma/dT\times\cos(2\pi x/\lambda)$. Solving this equation numerically, we find that the experimentally observed thickness undulation amplitude of $\Delta h=40$ nm requires a surface temperature variation of $\Delta T=5$K which is in agreement with the calculated temperature profile. Apparently, the system is stationary after 1 s of laser illumination. A larger amplitude of the thickness undulation would be obtained with a larger in-plane temperature gradient. This might be achieved by a higher laser power and/or with a pulsed laser. Yet, a mean temperature above the glass transition temperature of PMMA is required to ensure sufficient kinetics in the system.

Computer simulations were performed for a microscopic understanding of the formation of thin film thickness undulations by in-plane thermal gradients. In a KMC model, an Ising-type potential with a nearest neighbor interaction based on a face-centered cubic lattice is considered. The system with $(256\times256\times64)$ lattice sites has periodic boundary conditions in the x-y plane. Time is measured in Monte Carlo steps (MCS). Further details of the KMC method are given in Ref. 13. Referring to the scenario of Fig. 2(a), the image series in Figs. 5(a)–5(d) depicts the reaction pathway of the thermocapillarity-induced ripple formation on a thin film. For the sake of simplicity, a stationary sinusoidal temperature profile, $T(x)=T_0-\Delta T\sin(kx)$, is considered resembling the periodic temperature profile in Fig. 4 generated by the optical field. The mean temperature T_0 is high enough to supply sufficient thermal activation for a fast material transport. Due to the small size of the simulation cell a rather high temperature gradient ($\Delta T/T_0=0.2$) was used to achieve well-pronounced ripples with a short wavelength. According to

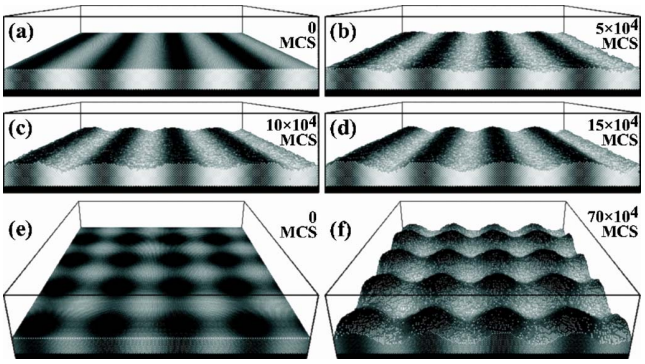

FIG. 5. [(a)–(d)] Series of KMC snapshots describing the thermocapillarity-induced ripple formation in a thin film. The color scale indicates the temperature in the film (dark = cold; light = hot). The black area illustrates the substrate. [(e) and (f)] KMC snapshots on the formation of hillock arrays.

Figs. 5(a)–5(d) biased material transport from hot to cold regions in the film is observed; thus, surface ripples are formed with the periodicity of the temperature profile. This periodic material redistribution is in phenomenological agreement with the experiment. In Figs. 5(e) and 5(f), two sinusoidal in-plane temperature profiles are superimposed orthogonally, i.e., $T(x,y)=T_0-\Delta T\sin(kx)\sin(ky)$. Resembling the experimental situation of Figs. 2(b) and 2(c), this situation results in the formation of a hillock array on the surface. Patterns with equal spatial frequencies but smaller (larger) amplitudes were obtained assuming lower (higher) temperature gradients. To a certain extent, a controlled material redistribution seems to be possible by adjusting the steady-state temperature profile. Due to the general aspect of KMC simulations it is expected that this nonequilibrium fabrication process of regular thickness undulations may be applicable to other thin film systems, even in the submicrometer range.

In conclusion, we have demonstrated that long-range-ordered regular surface patterns on thin PMMA films can be obtained by SPP-induced thermocapillarity. Periodic in-plane temperature fields were achieved by the nonradiative damping of standing SPP waves at a PMMA/Au interface. Numerical calculations on optical power loss and heat conduction as well as kinetic Monte Carlo simulations provide strong evidence that thermal gradients are the driving force of the in-plane material transport.

The authors would like to thank Anu Chandran for valuable discussions and assistance with RPM calculations. This work was partly supported by the German Research Foundation (project HE2137/2-1) and the Center for Probing the Nanoscale, a NSF Nanoscale Science and Engineering Center (PHY-0425897).

[1]M. Moseler and U. Landman, Science **289**, 1165 (2000).
[2]M. E. T. Molares, A. G. Balogh, T. W. Cornelius, R. Neumann, and C. Trautmann, Appl. Phys. Lett. **85**, 5337 (2004).
[3]P. Sutter, W. Ernst, Y. S. Choi, and E. Sutter, Appl. Phys. Lett. **88**, 141924 (2006).
[4]F. Korte, J. Koch, and B. N. Chichkov, Appl. Phys. A: Mater. Sci. Process. **79**, 879 (2004).
[5]F. Keilmann, K. W. Kussmaul, and Z. Szentirmay, Appl. Phys. B: Photophys. Laser Chem. **B47**, 169 (1988).
[6]E. Anemogiannis, E. N. Glytsis, and T. K. Gaylord, J. Lightwave Technol. **17**, 929 (1999).
[7]The laser is excited with a 5 kHz, 5% duty cycle square wave form. Due to the slow response of the laser plasma (~100 μs rise and fall time) the resulting output is mostly constant with a small 5 kHz amplitude variation.
[8]J. D. Jackson, *Classical Electrodynamics*, 3rd ed. (Wiley, New York, 1999), p. 264.
[9]F. Keilmann, B. Knoll, and A. Kramer, Phys. Status Solidi B **215**, 849 (1999).
[10]The following materials parameters were used: $\lambda_{air}=0.0245$ W m^{-1} K^{-1}, $\lambda_{PMMA}=0.16$ W m^{-1} K^{-1}, $\lambda_{Au}=317$ W m^{-1} K^{-1}, and $\lambda_{Si}=148$ W m^{-1} K^{-1}.
[11]*CRC Handbook of Chemistry and Physics*, 85th ed., edited by D. R. Lide (CRC, Boca Raton, FL, 2004), pp. 13–9.
[12]www.surface-tension.de/solid-surface-energy.htm
[13]M. Strobel, K.-H. Heinig, and W. Möller, Phys. Rev. B **64**, 245422 (2001).
[14]The temperature profile depends on the thermal contact to the sample holder. The assumed 0.5 μm air slit has the thermal resistivity of a carbon tape, approximately.

APPLIED PHYSICS LETTERS **90**, 181121 (2007)

Switchable two-color electroluminescence based on a Si metal-oxide-semiconductor structure doped with Eu

S. Prucnal, J. M. Sun,[a] W. Skorupa, and M. Helm[b]
Institute of Ion Beam Physics and Materials Research, Forschungszentrum Dresden-Rossendorf, P.O. Box 510119, 01314 Dresden, Germany

(Received 14 February 2007; accepted 5 April 2007; published online 3 May 2007)

A Si metal-oxide-semiconductor electroluminescent device structure is reported which emits two colors, while being doped with a single rare-earth element. Thermally grown SiO_2 oxide layers were implanted with Eu and subseqently annealed. Depending on the electrical excitation current, the luminescence is red or blue, which can be ascribed to electronic transitions in tri- and divalent europium (Eu^{3+} and Eu^{2+}), respectively. © *2007 American Institute of Physics*.
[DOI: 10.1063/1.2735285]

Great efforts are currently undertaken worldwide to achieve efficient light emission from Si based structures and devices with the aim of developing an integrated optoelectronic platform on Si.[1] Such light emitters appear attractive due to their material compatibility with the complementary metal-oxide-semiconductor (MOS) technology and may represent not only the basis for inter-/intrachip optical interconnects but also, e.g., microdisplays, waveguide amplifiers, or biological agent detection. Among the most promising approaches toward this goal are Si nanoclusters,[2,3] often embedded in a SiO_2 matrix and codoped with rare-earth ions.[4–6] Yet also sole doping with rare-earth ions can lead to light emission of different colors,[7] related to their specific energy level structure. Rare earths have also been embedded in other transparent host materials such as the wide-gap semiconductors SiC (Ref. 8) and GaN.[9] Recently, we have demonstrated MOS based light emitting diodes (MOSLEDs) doped with Er^{3+},[10] Tb^{3+},[11] Ce^{3+},[12] or Gd^{3+},[13] emitting in the infrared, green, blue, and ultraviolet spectral ranges, respectively. These MOSLEDs typically reach external quantum efficiencies between 1% and 10%.[7,10–13] In this letter we demonstrate a *switchable two-color* MOSLED doped with Eu, taking advantage of the fact that Eu occurs in the two oxidation states Eu^{3+} and Eu^{2+}. The electroluminescence (EL) can be switched with the excitation current between red (low current) and blue (high current), ascribed to electronic transitions in tri- and divalent Eu ions, respectively.

Most of the rare-earth (RE) elements occur in host materials in their trivalent oxidation state. Their $4f^n$ configuration is relatively isolated and the next excited configuration $4f^{n-1}$ $5d$ is located more than 5 eV above the ground state of the $4f^n$ configuration. The $4f$ electrons of RE^{3+} ions embedded in solids are thus well shielded from external fields, and sharp lines due to intrashell $4f$-$4f$ transitions for both optical absorption and emission spectra are observed. These transitions are dipole forbidden in the free ions and become allowed only due to the reduced symmetry of the host matrix. Eu, Sm, and Yb can also exist in solids as divalent ions containing one more electron. The $4f^{n-1}$ $5d$ states of RE^{2+} ions interact strongly with the matrix and the interconfigurational $4f^n$ to $4f^{n-1}$ $5d$ transitions of divalent rare earths are dipole allowed. They have transition strengths several orders of magnitude higher than $4f$-$4f$ transitions.[14] However, this does not necessarily translate into higher electroluminescence intensity, since the latter also depends on nonradiative relaxation time and the excitation efficiency.

The MOSLED device structures were prepared by standard silicon complementary MOS technology on 4 in. n-type silicon wafers. The structure consists of an active gate oxide area (SiO_2) surrounded by a 1 μm thick field oxide. Thermally grown 100 nm thick SiO_2 layers were implanted by Eu with an energy of 100 keV and subsequently annealed at 900 °C for 40 min. The concentration of Eu was ranging from 0.5% up to 3%. In order to protect the oxide layer against instability breakdown, a 50 nm SiON layer was deposited on it by plasma-enhanced chemical vapor deposition (ratio between O and N was 1:1). The gate electrode consists of a 100 nm thick indium tin oxide (ITO) deposited by rf sputtering. The diameter of the MOS device was between 1 and 500 μm. The EL spectra were measured at room temperature in the region from 350 to 750 nm on MOS structures with a circular ITO electrode of 200 μm diameter at constant current supplied by a source meter (Keithley 2410). The measurements were performed with electron injection from the silicon substrate. The same type of structures was used for the investigation of the EL intensity as function of excitation current. The EL signal was recorded using a monochromator (Jobin Yvon Triax 320) and a photomultiplier (Hamamatsu H7732-10). Photographs were taken by a standard digital camera connected with an optical microscope.

Figure 1 shows the EL spectra of MOSLED device structures implanted with different concentrations of Eu under 10 μA dc current injection. The EL is generated by hot-electron induced impact excitation of RE ions during Fowler-Nordheim tunneling. Peaks at 573, 616, and 655 nm are attributed to the $4f^5D_0$-^7F_J ($J=1,2,3$) intrashell transitions of Eu^{3+}, whose spectral positions are known to depend only weakly on the host material. On the other hand, the $5d$ electrons strongly interact with the host crystal field, and therefore the peak position of the lowest transition of Eu^{2+} doped materials varies more strongly with the host material than is the case for RE^{3+} doping.[15] In the case of the SiO_2 matrix, divalent europium exhibits two broad bands with maximum

[a]Present address: Institute of Physics, Nankai University, 300071 Tianjin, China.
[b]Electronic mails: m.helm@fzd.de

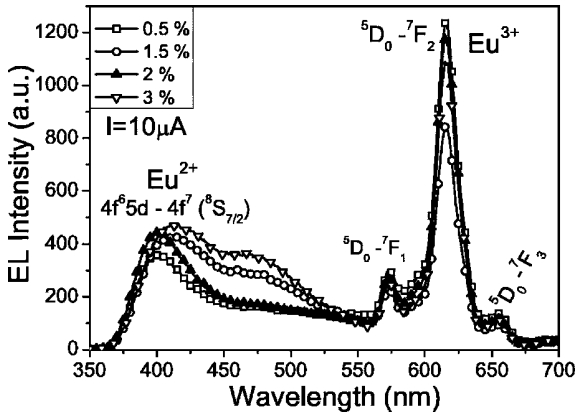

FIG. 1. Electroluminescence spectra of SiO_2:Eu MOSLED devices with different Eu concentrations as indicated. The excitation current is 10 μA and the device diameter is 200 μm.

intensities at 400 and 470 nm, corresponding to the $4f^6$ $5d$-$4f^7$ ($^8S_{7/2}$) transitions. (Note that the peak at 470 nm may also have some contribution from oxygen deficiency centers in SiO_2.[16]). For Eu^{2+} the strongest luminescence was observed for a concentration of 3%, while the trivalent europium shows the highest electroluminescence for the lowest europium concentration (0.5%). At higher concentrations, this intra-$4f$ electroluminescence may undergo concentration quenching,[11] caused by a nonradiative energy transfer between two neighboring Eu atoms.

Figure 2 shows the dependence of the blue and red EL intensities and applied voltage on the current for samples containing 0.5% of Eu. The radiative transition between the $^5D_0$ and $^7F_2$ levels in Eu^{3+} is observed already for a current of 2×10^{-8} A and a voltage of 99 V. With increasing injection current the red light monotonically increases up to the breakdown point. To obtain a population of the first excited level $4f^6$ $5d$ in divalent europium, higher voltages (>105 V) and current ($>4\times10^{-7}$ A) are needed. An increase of the 400 nm emission with current was observed up to 1 mA before it is finally quenched. For a current of up to 90 μA, the red light dominates over the blue one. In the range of 90 mA–1.8 the reverse situation is observed. The

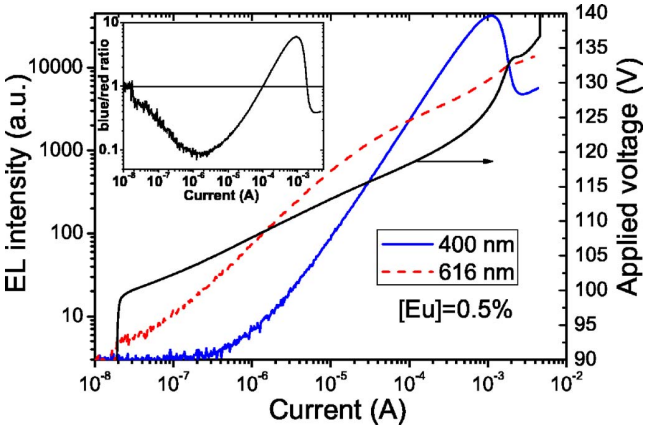

FIG. 2. (Color online) Electroluminescence intensity of a MOSLED device with 0.5% Eu, measured at 400 nm (blue solid curve) and 616 nm (red dashed curve) as a function of the injection current (left scale). The black solid curve shows the applied voltage vs current (right scale). The inset displays the ratio of the blue to the red EL vs injection current. The device was 200 μm in diameter.

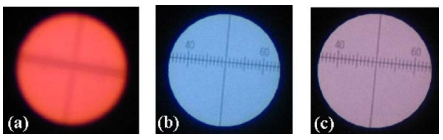

FIG. 3. (Color online) Photographs of SiO_2:Eu MOSLED devices with 200 μm diameter. The excitation currents were 20 μA (a), 1 mA (b), and 2.5 mA (c), respectively.

inset of Fig. 2 shows the blue/red ratio of the EL intensity versus current. It is clearly visible that by a proper choice of the operation current regime it is possible to switch between the two main colors: red and blue. In addition, for a current of around 100 μA as well as higher than 1.8 mA both colors have similar intensity resulting in violet emission [see Fig. 3(c)]. Operating at one of these crossover points, switching can be achieved by superimposing a small ac modulation voltage. Such a switchable two-color behavior has not been reported before for Si based light emitters. We are only aware of GaN based devices, where two colors were generated using two different rare-earth ions (Er and Eu).[17,18] The simplest explanation of the color change with applied voltage can be given considering the hot-electron distribution in the oxide.[19] At lower electric fields the average electron kinetic energy is only sufficient to excite the red transition (transition energy of ~2 eV), whereas at higher fields the electrons are more energetic and can also excite the blue transition (2.5–3 eV). Another possibility is electron capture at high current. A more detailed understanding of the microscopic mechanism will require further experiments.

Figure 3 shows photographs taken from devices of 200 μm diameter by a standard digital camera under an optical microscope. The red-light emission obtained with low-current excitation is presented in Fig. 3(a). Similar results were observed by Heikenfeld *et al.* from a GaN:Eu LED.[20] The blue electroluminescence [see Fig. 3(b)] from any matrix containing Eu^{2+} was not observed up to now. Kim and Holloway have identified both divalent and trivalent europium ions in GaN by x-ray photoelectron spectroscopy, but they observed EL only from Eu^{3+}.[21] Cathodoluminescence from Eu^{2+} doped $BaMg_{(1+x)}Si_xAl_{10}O_y$ has been reported by Studenikin and Cocivera.[22]

In summary, we have presented a switchable two-color MOSLED device structure based on a Eu implanted SiO_2 layer. This shows that photonics based on silicon has still a lot of potential, and even offers interesting optoelectronic functionalities. Future goals will be aimed toward a microscopic understanding of the two-color behavior and a reduction of the operating voltage by using thinner oxides. Combination with a green light emitter such as SiO_2:Tb could result in a Si based full-color microdisplay.

The authors would like to thank J. Winkler and F. Ludewig for the ion implantation, H. Felsmann, C. Neisser, and G. Schnabel for the processing of the MOS structures.

[1] S. Ossicini, L. Pavesi, and F. Priolo, *Light Emitting Silicon for Microphotonics*, Springer Tracts in Modern Physics Vol. 194 (Springer, New York, 2003).
[2] L. Pavesi, L. Dal Negro, C. Mazzoleni, G. Franzó, and F. Priolo, Nature (London) **408**, 440 (2000).
[3] R. J. Walters, G. I. Bourianoff, and H. A. Atwater, Nat. Mater. **4**, 143 (2005).
[4] A. Polman, Nat. Mater. **1**, 10 (2002).

[5]M. Fujii, M. Yoshida, Y. Kanzawa, S. Hayashi, and K. Yamamoto, Appl. Phys. Lett. **71**, 1198 (1997).
[6]S. Minissale, T. Gregorkiewicz, M. Forcales, and R. G. Elliman, Appl. Phys. Lett. **89**, 171908 (2006), and references therein.
[7]M. E. Castagna, S. Coffa, M. Monaco, A. Muscara, L. Caristia, S. Lorenti, and A. Messina, Mater. Sci. Eng., B **105**, 83 (2003).
[8]W. J. Choyke, R. P. Devaty, L. L. Clemen, M. Yoganathan, G. Pensl, and Ch. Hässler, Appl. Phys. Lett. **65**, 1668 (1994).
[9]A. J. Steckl, J. C. Heikenfeld, D.-S. Lee, M. J. Garter, C. C. Baker, Y. Wang, and R. Jones, IEEE J. Sel. Top. Quantum Electron. **8**, 749 (2002).
[10]J. M. Sun, W. Skorupa, T. Dekorsy, M. Helm, and A. M. Nazarov, Opt. Mater. (Amsterdam, Neth.) **27**, 1050 (2005).
[11]J. M. Sun, W. Skorupa, T. Dekorsy, M. Helm, L. Rebohle, and T. Gebel, J. Appl. Phys. **97**, 123513 (2005).
[12]J. M. Sun, S. Prucnal, W. Skorupa, M. Helm, L. Rebohle, and T. Gebel, Appl. Phys. Lett. **89**, 091908 (2006).
[13]J. M. Sun, W. Skorupa, T. Dekorsy, M. Helm, L. Rebohle, and T. Gebel, Appl. Phys. Lett. **85**, 3387 (2004).
[14]G. Liu and B. Jacquier, *Spectroscopic Properties of Rare Earths in Optical Materials* (Springer, Berlin, 2005), p. 122.
[15]J. Rubio, J. Phys. Chem. Solids **52**, 101 (1991).
[16]W. Skorupa, L. Rebohle, and T. Gebel, Appl. Phys. A: Mater. Sci. Process. **76**, 1049 (2003).
[17]D. S. Lee, J. Heikenfeld, R. Birkhahn, M. Garter, B. K. Lee, and A. J. Steckl, Appl. Phys. Lett. **76**, 1525 (2000).
[18]J. Heikenfeld and A. J. Steckl, IEEE Trans. Electron Devices **49**, 1545 (2002).
[19]M. V. Fischetti, D. J. DiMaria, S. D. Brorson, T. N. Theis, and J. R. Kirtley, Phys. Rev. B **31**, 8124 (1985).
[20]J. Heikenfeld, M. Garter, D. S. Lee, R. Birkhahn, and A. J. Steckl, Appl. Phys. Lett. **75**, 1189 (1999).
[21]J. H. Kim and P. H. Holloway, J. Appl. Phys. **95**, 4787 (2004).
[22]S. A. Studenikin and M. Cocivera, Thin Solid Films **394**, 264 (2001).

APPLIED PHYSICS LETTERS **91**, 232110 (2007)

Meyer-Neldel rule in ZnO

Heidemarie Schmidt[a)]
Institut für Experimentelle Physik II, Fakultät für Physik und Geowissenschaften, Universität Leipzig, Linnéstraße 3-5, 04103 Leipzig, Germany, and Forschungszentrum Dresden-Rossendorf e. V., Institut für Ionenstrahlphysik und Materialforschung, Bautzner Landstrasse 128, 01328 Dresden, Germany

Maria Wiebe, Beatrice Dittes, and Marius Grundmann
Institut für Experimentelle Physik II, Fakultät für Physik und Geowissenschaften, Universität Leipzig, Linnéstraße 3-5, 04103 Leipzig, Germany

(Received 11 April 2007; accepted 9 November 2007; published online 6 December 2007)

Seventy years ago Meyer and Neldel investigated four polycrystalline *n*-type conducting ZnO rods [W. Meyer and H. Neldel, Z. Tech. Phys. (Leipzig) **12**, 588 (1937)]. The specific conductivity increased exponentially with temperature. A linear relationship between the thermal activation energy for the specific conductivity and the logarithm of the prefactor was observed. Since then thermally activated processes revealing this behavior are said to follow the Meyer-Neldel (MN) rule. We show that the emission of charge carriers from deep electron traps in ZnO follows the MN rule with the isokinetic temperature amounting to 226±4 K. © *2007 American Institute of Physics*. [DOI: 10.1063/1.2819603]

In this work, we report on the properties of deep electron defects in ZnO thin films probed by deep level transient spectroscopy (DLTS).[1] The apparent thermal activation energy E_a and the capture cross section σ_i are the fingerprints of deep defects. However, due to the simple analysis of DLTS data,

$$e_i(T) = 1/\tau = N_c \upsilon_{\mathrm{th}} \sigma_i \exp(-E_a/k_B T) = e_0 T^2 \exp(-E_a/k_B T), \quad (1)$$

where a temperature independent capture cross section σ_i is assumed, the reported capture cross sections vary over many orders of magnitude. The parameter e_0 is related with the apparent capture cross section σ_i by

$$e_0 = N_c \upsilon_{\mathrm{th}} \sigma_i / T^2 = 4\pi \left(\frac{m^\star k^2}{h^3} \right) \sqrt{6\pi} \sigma_i. \quad (2)$$

Therefore, even in nominally undoped, intrinsically *n*-conducting ZnO, the "fingerprints" of deep defects are not unambiguous.

Seventy years ago Meyer and Neldel investigated the temperature dependence of the specific conductivity σ in ZnO and other oxidic compounds and found that the conductivity depends exponentially on temperature,

$$\sigma = \sigma_0 \exp(-E_a/k_B T), \quad [\sigma] = \Omega^{-1}\,\mathrm{cm}^{-1}. \quad (3)$$

Furthermore, they observed that the prefactor σ_0 depends on the activation energy E_a.[2] In more detail, the logarithm of the prefactor reads

$$\ln(\sigma_0) = \ln(\sigma_{00}) + E_a/k_B T_{\mathrm{iso}}, \quad (4)$$

with σ_{00} being a true constant and T_{iso} being the so-called isokinetic temperature.[3] The empiric Meyer-Neldel (MN) behavior has been found in different thermally activated processes including charge emission[4] and current flow,[5] and is well known to chemists from surface desorption processes.[6] Equation (4) is a good approximation if the conductivity is determined by deep traps. However, if shallow impurities determine the conductivity, the parameter σ_{00} strongly depends on the Fermi level position and mobility, and appears to be temperature dependent. If determined from conductivity measurements, the σ_{00} parameter thus may differ in one and the same material with different deep traps and shallow impurities.

We probed the parameters of deep electron defects in *n*-type conducting ZnO thin films using DLTS. Different groups report on thermal activation energies ranging from 0.1 up to 0.6 eV below the ZnO conduction band minimum and an abnormally large variation of the capture cross section. Here, we report a correct analysis of DLTS data with a temperature dependent capture cross section[4] and reveal that deep electron defects in ZnO exhibit a MN behavior. Our work will enable the categorization of deep electron defects in ZnO with respect to the change of phonon configuration entropy in the thermally activated carrier detrapping from deep defects. We have investigated more than 130 samples of ~1 μm thick ZnO films by DLTS. The epilayer structures consist of an ~0.2 μm thick 1% Al-doped ZnO layer grown by pulsed laser deposition on 10×10 mm^2 *a*-plane sapphire substrates using a KrF excimer laser,[7] serving as the Ohmic back electrode,[8] before the deposition of undoped ZnO films or of ZnO films doped with different 3*d* transition metal ions. All deposited films were *n* conducting. Finally, circular Schottky contacts were fabricated by thermal evaporation of Pd on the film surface.

DLTS is a powerful technique to characterize deep defects in the depletion region of reverse biased diodes by providing the thermal activation energy E_a, electron capture cross section σ_i, and defect concentration N_T.[9] For DLTS, the free charge carrier concentration has to be at least one order of magnitude larger than N_T in order to ensure that the Fermi level position is not influenced by the deep defects themselves. Typically, this condition is fulfilled in our samples for temperatures above 50 K with free charge carrier concentra-

a)Electronic mail: Heidemarie.Schmidt@fzd.de.

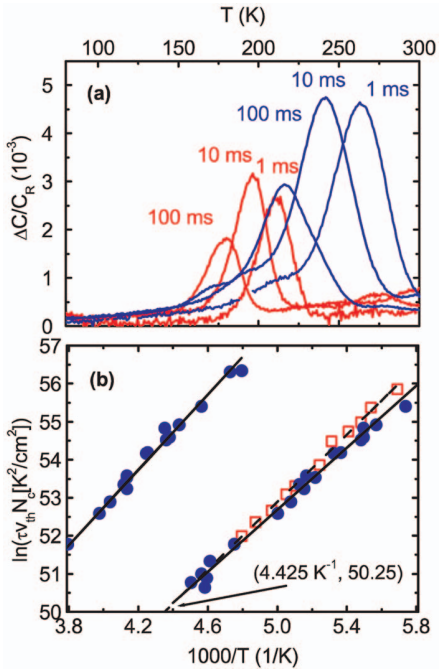

FIG. 1. (Color) (a) DLTS spectra measured at several rate windows T_w=1, 10, and 100 ms on two ZnO-Schottky diodes prepared from a nominally undoped ZnO film (red lines) and a Co-doped ZnO film with 0.2 at. % Co (blue lines) grown at 730 °C and 0.016 mbar. The DLTS peak temperature increases with decreasing rate window. (b) Standard Arrhenius evaluation for the DLTS spectra reveals the same slope and different intersection points, i.e., nearly the same thermal activation energy E_a and different apparent capture cross sections amounting to $\sigma_i=7.9\times10^{-14}$ cm^2 for the undoped ZnO (red squares) and to $\sigma_i=5.8\times10^{-16}$ cm^2 for the Co-doped ZnO film (blue circles).

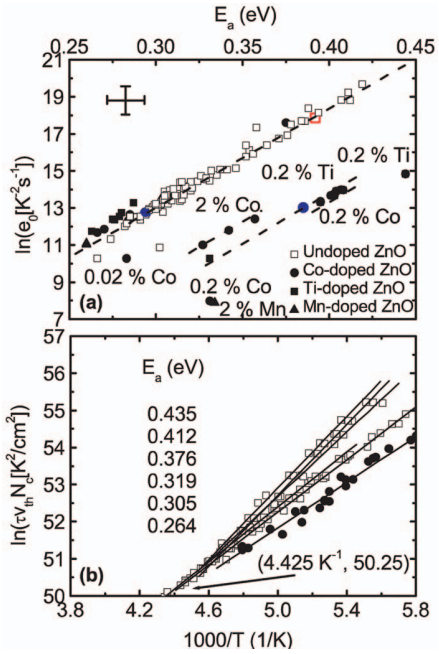

FIG. 2. (Color) (a) MN plot of $\ln(e_0)$ vs E_a of more than 130 ZnO Schottky diodes. The curve was generated using standard DLTS analysis for electron traps in 3*d* transition metal doped ZnO and nominally undoped ZnO. The $[E_a, \ln(e_0)]$ coordinates of the nominally undoped (red square) and Co-doped ZnO film (blue circles) from Fig. 1(b) are (0.386 eV, 17.77) and (0.385 eV, 13.03/0.294 eV, 12.75), respectively. (b) Arrhenius plots from six points (i.e., samples) lying on the MN line in (a) with different thermal activation energies E_a. For all six data sets, the corresponding Arrhenius plots cross at (4.424 K^{-1}, 50.25). The symbols have the same meaning as in (a).

tions ranging between 10^{16} and 10^{18} cm^{-3}. The DLTS technique records temporal capacitance changes after filling deep defects in the depletion region by applying a pulse voltage U_P during the filling pulse time t_P. For short filling pulse duration, not all deep defects may be filled resulting into a too small value for the capture cross section. We recorded the capacitance transients up to T=300 K in steps of 1 K at different period widths T_w and filling pulse times t_p ranging between 1 and 100 ms using a FT 1030 DLTS system[10] and a "square-lock-in" correlation function with a largest detectable emission rate of e_i=15 000 s^{-1}. For most samples, the filling pulse duration was long enough. DLTS spectra of two samples containing dominant defects with the same apparent thermal activation energy E_a and the apparent capture cross section varying by two orders of magnitude are shown in Fig. 1(a) for three different period widths. DLTS peaks occur where the emission rate of the traps $e_i(T)$ [Eq. (1)] lies within the period width,[9] i.e., the response peak shifts to lower temperatures with increasing period width. It is noted that the DLTS peak of the Co-doped ZnO is abnormally wide [Fig. 1(a)]. We used the CONTIN routine to resolve the DLTS peak overlap yielding two deep defects of similar concentration amounting to $N_T=2\times10^{14}$ cm^{-3} with DLTS signatures given by E_a=0.294 eV and $\sigma_i=4.4\times10^{-16}$ cm^2, and E_a=0.385 eV and $\sigma_i=5.8\times10^{-16}$ cm^2 [Fig. 1(b)]. Assuming thermal emission processes, standard Arrhenius evaluation yields the thermal activation energy E_a and capture cross section σ_i [Fig. 1(b)]. In the standard DLTS analysis σ_i [Eq. (2)] is assumed to be temperature independent. Possible detrapping entropy changes are neglected. However, we find a linear relationship between $\ln(e_0)$ and E_a [Fig. 2(a)],

$$\ln(e_0) = \ln(e_{00}) + \frac{E_a}{k_B T_{\mathrm{iso}}}, \tag{5}$$

from the Arrhenius plots evaluated from more than 130 samples. Here, e_{00} is a constant. The observed activation energies lie in the same energy range as commonly observed deep electron traps in ZnO (Ref. 11) amassing close to the deep electron trap E3 around 0.30 eV (Ref. 8) [Fig. 2(a)]. Electric field-assisted emission can cause a reduction ΔE_a of the thermal activation energy with respect to the low-field value. For a long-ranging defect potential, ΔE_a may be estimated from the Frenkel-Poole effect and amounts to 5 and 28 meV for a free charge carrier density of 10^{16} and 10^{18} cm^{-3} and the corresponding electric field strength amounting to 35 kV/cm and 110 kV/cm, respectively, for reverse biased *n*-ZnO Schottky diodes (U_R=−2 V) and a built-in potential of 0.7 V. Electric field-assisted effects may partially explain the spread in DLTS data represented in Fig. 2(a). Similar to the conductivity being independent of the activation energy E_a at the isokinetic temperature T_{iso} [Eqs. (3) and (4)],[2] we find that the emission rate is [Eq. (1)] independent of E_a at T_{iso}. That means that for all points on the MN line, the corresponding Arrhenius plots cross at (4.424 K^{-1}, 50.25) [Fig. 1(b)]. The MN rule assumes a considerable entropy change (ΔS) in thermal excitation, where $\Delta S=E_a/T_{\mathrm{iso}}=\Delta S_{\mathrm{ph}}+\Delta S_{\mathrm{el}}$ is defined by the electron entropy

term ΔS_{el} and the phonon configuration entropy ΔS_{ph}. Substituting Eq. (5) into Eq. (1) yields

$$e_i(T) = e_{00} \exp(E_a/k_B T_{iso}) T^2 \exp(-E_a/k_B T). \quad (6)$$

The slope of the MN line in Fig. 2(a) is $(k_B T_{iso})^{-1}$ with $T_{iso}=226$ K. At $T=T_{iso}$, e_i is independent of E_a [Fig. 2(b)] for all samples on the MN line. T_{iso}^{-1} is not far outside the DLTS data range. From the intersection of the MN line with the $\ln(e_0)$ axis in Fig. 2(a), $\ln(e_{00})=\ln[e_0(E_a \rightarrow 0)] = \ln[e_0(T \rightarrow \infty)]=-2.14$ has been determined. Because the estimated values of e_0 and E_a are not independent, slightly different MN lines may result with the isokinetic temperature amounting to 226 ± 4 K. Mainly, deep electron traps in $3d$ transition metal doped ZnO thin films lie below the MN line. Their smaller apparent capture cross sections hint toward a too short filling pulse time t_p or the presence of other deep defects in $3d$ transition metal doped ZnO thin films simultaneously filled when the pulse voltage is applied during the filling pulse time t_p. Probably, due to an uncomplete filling and a reduced apparent capture cross section, the deep defect in Co-doped ZnO with the same thermal activation energy as the defect in undoped ZnO [Fig. 1(b)] lies below the MN line [Fig. 2(a)]. The defect in Co-doped ZnO with the smaller thermal activation energy [Fig. 1(b)] lies on the MN line [Fig. 1(a)] and seems to be completely filled. All deep electron traps on the MN line emit at the determined $T_{iso}=226$ K with the same rate $e_i(T_{iso})=e_{00}T_{iso}^2=5996$ s^{-1}. For $T \rightarrow \infty$, a single capture cross section amounting to 1.5×10^{-22} cm^2 has been determined for deep electron traps on the MN line using $m^\star=0.24m_0$ (Ref. 12) in Eqs. (1) and (5). Despite the smaller capture cross section, the isokinetic temperature is the same for a set of Co-doped and Ti-doped ZnO films [scattered lines with the same slope in Fig. 2(a)]. Because the thermal activation energy E_a is large compared to typical elementary excitations of the system, many excitations of the system have to be assembled before the thermally activated emission of trapped electrons may take place.[13] Namely, $n=E_a/E_{ph}$ phonons have to be annihilated, where E_{ph} is the phonon energy amounting to 72 meV for longitudinal optical (LO) phonons in ZnO. Assuming N phonons lie in the interaction volume, the dimensionless entropy change associated with the thermally activated process is the natural logarithm of the number of ways of assembling n out of N interacting phonons,[13]

$$\Delta S/k_B = \frac{E_a}{k_B T_{iso}} = \ln\left[\frac{N!}{n!(N-n)!}\right]. \quad (7)$$

For $n \ll N$, Eq. (7) simplifes to $S/k_B=n\ln(N/n)$ and the temperature dependent number of phonons N which have to lie in the interaction volume may be easily determined. For example, for the deep electron trap E3 $n\approx4$ and $N\approx200$.

In summary, we have shown that the charge-carrier emission rate from deep levels in n-type conducting ZnO obeys the MN rule with an isokinetic temperature of 226 K. Mainly observed in $3d$ transition metal doped ZnO, an incomplete filling of deep defects reduces the apparent capture cross section. The single capture cross section of deep electron traps in ZnO lying on the MN line has been determined by including entropy changes in a detailed balance analysis and amounts to $\sigma_i=1.5\times10^{-22}$ cm^2. The MN line may not be extended to shallow defects in hydrothermally grown ZnO single crystals probed by admittance spectroscopy measurements.[14] Compared to deep defects in ZnO, this hints toward different entropy changes in thermal excitation of shallow defects in ZnO. Finally, we would like to state that the MN behavior can only be explored by investigating thermally activated processes with well-known temperature dependent prefactors in a large set of samples.

Parts of this work (H.S.) were supported by the German Federal Ministry of Science and Research (FKZ 03N8708). We acknowledge epilayer and diode preparation and fruitful discussions with G. Biehne, G. Ramm, H. Hochmuth, M. Lorenz, H. von Wenckstern (University Leipzig), and L. Cohausz and S. Weiss (PhysTech GmbH).

[1] M. Diaconu, H. Schmidt, H. Hochmuth, M. Lorenz, H. von Wenckstern, G. Biehne, D. Spemann, and M. Grundmann, Solid State Commun. **137**, 417 (2006).
[2] W. Meyer and H. Neldel, Z. Tech. Phys. (Leipzig) **12**, 588 (1937).
[3] A. Abd-El Mongy, Egypt. J. Solids **24**, 207 (2001).
[4] J. A. M. AbuShama, S. W. Johston, R. S. Crandall, and R. Noufi, Appl. Phys. Lett. **87**, 123502 (2006).
[5] R. Widenhorn, M. Fitzgibbons, and E. Bodegom, J. Appl. Phys. **96**, 7379 (2004).
[6] F. Grosse, W. Barvosa-Carter, J. J. Zinck, and M. F. Gyure, Phys. Rev. B **66**, 075321 (2002).
[7] M. Lorenz, in *Basics and Applications in Thin Film Solar Cells* (Springer Series in Material Science), edited by K. Ellmer, A. Klein, and B. Rech (Springer, Berlin, 2007), Vol. 7, p. 303.
[8] H. von Wenckstern, S. Weinhold, G. Biehne, R. Pickenhain, H. Schmidt, H. Hochmuth, and M. Grundmann, Adv. Solid State Phys. **45**, 263 (2005).
[9] D. V. Lang, J. Appl. Phys. **45**, 3023 (1974).
[10] S. Weiss and R. Kassing, Solid-State Electron. **31**, 1733 (1988).
[11] F. D. Auret, S. A. Goodman, M. J. Legodi, W. E. Meyer, and D. C. Look, Appl. Phys. Lett. **80**, 1340 (2002).
[12] W. S. Baer, Phys. Rev. **154**, 785 (1967).
[13] A. Yelon, B. Movaghar, and H. M. Branz, Phys. Rev. B **46**, 12244 (1992).
[14] H. von Wenckstern, H. Schmidt, M. Grundmann, M. W. Allen, P. Miller, R. J. Reeves, and S. M. Durbin, Appl. Phys. Lett. **91**, 022913 (2007).

APPLIED PHYSICS LETTERS **91**, 081109 (2007)

Coherent terahertz detection with a large-area photoconductive antenna

F. Peter,[a] S. Winnerl, S. Nitsche, A. Dreyhaupt, H. Schneider, and M. Helm
Institute of Ion Beam Physics and Materials Research, Forschungszentrum Dresden Rossendorf, P.O. Box 510119, 01314 Dresden, Germany

(Received 3 July 2007; accepted 27 July 2007; published online 21 August 2007)

We present a nonresonant photoconductive terahertz detection antenna suitable for detection of both focused and unfocused terahertz radiations. Our system consists of a scalable terahertz emitter based on an interdigitated electrode structure and a detection antenna with similar electrode geometry. While the emitter is fabricated on semi-insulating GaAs we compare different ion-implanted GaAs-based detection antennas. We studied the dependence of the measured terahertz signal on the power and spot size of the gating laser pulse. In addition we compare the performance of our antenna with that of electro-optical sampling. © *2007 American Institute of Physics*. [DOI: 10.1063/1.2772783]

Terahertz spectroscopy is of great scientific and technological interest in different fields.[1,2] While many time domain terahertz spectroscopy systems use electro-optic detection, there have been various advances in the field of photoconductive (PC) terahertz detection in recent years. In particular, new antenna geometries have been developed for polarization sensitive detection.[3] Furthermore, GaAs implanted with H^+ or N^+,[4,5] and ErAs:GaAs nanoisland superlattices[6] have been tested successfully as alternative substrate materials with a short carrier lifetime instead of the commonly used low-temperature grown GaAs for detection antennas. An important advantage of PC detection over electro-optic sampling is the possibility to build compact fiber-coupled systems.[7] Avoiding bulky reflective optical elements by applying silicon lenses makes such systems very attractive for imaging and for spectroscopy in magnetic fields.[8,9] So far all PC detection antennas are dipole antennas with typical gap width of a few micrometers.[10] Therefore the alignment is not simple, the beam pointing stability is crucial, and the possibility to move the antenna is limited.

In this letter we discuss a detection antenna based on a scalable interdigitated metallization where every second spacing between the electrodes is blocked by another gold layer. Using N^+-implanted GaAs substrates, high-performance terahertz detection is achieved with the additional benefit of allowing flexibility with respect to the spot diameter of both the terahertz signal and the gating laser. The sensitivity of the antenna is also compared with that of electro-optical sampling.

The design of the terahertz detector is similar to the structure of a terahertz emitter reported previously,[11] however, with a smaller area of 1×1 mm^2. The interdigitated metallization comprises 5 μm wide metal stripes with 5 μm spacing. An additional gold layer, separated from the first metallization by an isolating dielectric, blocks the optical excitation in every second spacing between the electrodes. In order to achieve a short carrier lifetime, semi-insulating (SI) GaAs implanted with N^+ (dual-energy implant, 0.4 MeV, dose 1×10^{13} cm^{-2} and 0.9 MeV, dose 3×10^{13} cm^{-2}) is used as a substrate for the antennas. The implantation results in a nearly homogeneous vacancy density to a depth of about 1 μm.[12] A terahertz field induces a photocurrent in this nonresonant antenna, as electrons are accelerated towards one set of connected electrode fingers and holes to the opposite ones.

For our experiments we use a standard setup, as described in Ref. 13. A mode-locked Ti:sapphire laser which generates 50 fs pulses at a wavelength of 800 nm is used for exciting the terahertz emitter and for coherent detection. The terahertz radiation is collimated and focused by a pair of off-axis parabolic mirrors. The terahertz signal and the probe beam are combined by a tin doped indium oxide coated mirror. The PC antenna is placed in the focus of the second parabolic mirror in the setup, such that both the terahertz radiation and the optical gating beam enter the antenna on the metallized side. The detected current is preamplified using a transimpedance amplifier (Femto DLPCA-200). The emitter used for the measurements had a similar electrode geometry as the detector, but with a 3×3 mm^2 active area and fabricated on SI GaAs. The emitter was driven with a bias of 15 V and excited with 450 mW of laser power focussed to a spot of 300 μm full width at half maximum (FWHM). To compare the PC antenna with electro-optic sensing, the detection antenna is replaced by a 160 μm thick (110) ZnTe crystal and two balanced photodiodes, as described in Ref. 13. The laser power for electro-optical detection and also for PC detection was 3 mW (spot size of 130 μm FWHM).

Figure 1(a) shows the comparison between PC detection and electro-optical sensing under similar conditions. For the PC detection a maximum current of 7 nA was measured. In Fig. 1(a) the temporal derivative of the current is plotted. The signal-to-noise ratio is 7×10^3 for electro-optical detection and 8×10^2 for photoconductive detection measured with a 100 ms time constant.

In general the detected current $I(t)$ is proportional to a convolution $I(t)\propto\int_{-\infty}^{\infty}E(t_1)g(t-t_1)dt_1$ of the time dependent conductivity $g(t)$ and the time dependent terahertz field $E(t)$. Assuming a single exponential decay of the type $g(t)\propto e^{-t/\tau}\Theta(t)$ with the Heaviside function $\Theta(t)$ and time constant τ allows us to deconvolve the measured current. The terahertz field is then given by the relation $E(t)\propto[dI(t)/dt]+(1/\tau)I(t)$. If the carrier lifetime is much shorter than the typical timescale of the terahertz waveform, the measured

[a]Electronic mail: f.peter@fzd.de

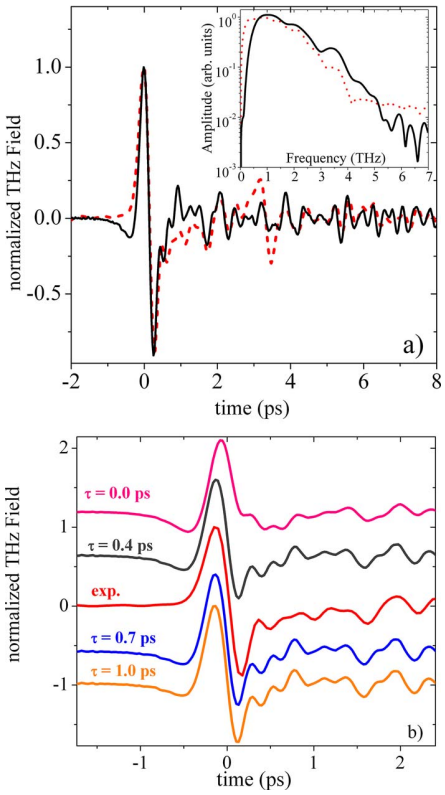

FIG. 1. (Color online) (a) Time domain terahertz wave form detected with electro-optical sensing (dotted line). The solid line shows the first derivative in time of the measured photocurrent. The spot diameter on the PC detector was 130 μm. The inset of (a) shows the calculated amplitude spectra. (b) shows a comparison between electro-optical signal (exp) and modeled using different carrier lifetimes of the detector material τ.

current is directly proportional to $E(t)$. In the opposite case of long carrier lifetimes, $E(t)$ is proportional to the first derivative of the measured current.

To characterize the PC material, we compare the field obtained from deconvoluting the measured current assuming different time constants with the result from electro-optical sampling [Fig. 1(b)]. For clarity, all curves are normalized and vertically shifted. For τ=0.0 ps the plotted curve corresponds to the measured current. Good agreement at positive time delay between the experimental curve and the calculation is found for τ=0.7 ps. The deviation for negative time delay can be attributed to slight differences in the terahertz wave forms seen by electro-optic detection and PC antenna due to different reflectivities of the surfaces. However, the comparison of the calculated and measured signals provides convincing evidence that the N^+ implanted material has a characteristic response time of at least 0.7 ps.

To investigate the proper gating conditions of the detector and to resolve the spatial emission characteristics of the emitter we removed the off-axis parabolic mirrors. The emitter and detector are now placed directly opposite to each other at a distance of 27 mm and the unfocused terahertz beam is detected. In this configuration the terahertz wave enters the detector through the substrate, while the optical gating pulse still hits the metallized side of the antenna. The excitation power on the emitter is 350 mW and the spot size is again 300 μm. The spot size of the optical gating pulse is 50 μm. Figure 2 shows the detected terahertz signal for different excitation densities at the detector. The highest excitation density corresponds to a power of 100 mW. At low excitation densities the terahertz field induced current increases linearly, as shown in the inset of Fig. 2. At higher excitation density the increase becomes sublinear. This is presumably caused by carrier scattering and screening effects at an excitation density of the order of several 10^{17} cm^{-3}.[14] Due to the large spot size of the gating beam the antenna can be driven at significantly higher laser power, as compared to conventional dipole antennas. This allows one to achieve photocurrents up to 2 nA in this configuration for detection of an unfocused terahertz beam.

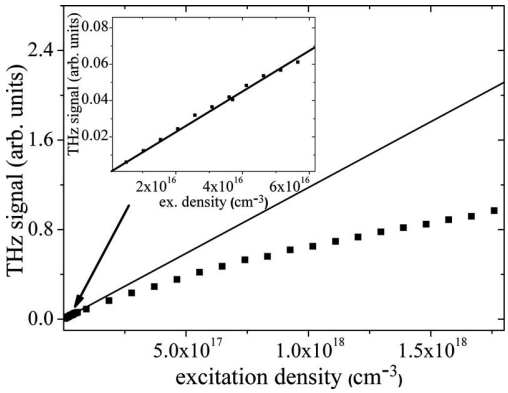

FIG. 2. Measured terahertz signal for different excitation densities at the photoconductive detector. The inset shows the linear behavior for low excitation densities. The solid line is the linear extrapolation from the low excitation densities.

To find optimum operation conditions we varied the spot size of the gating beam while keeping its power constant at 70 mW. The results are shown in Fig. 3. The terahertz signal increases strongly with spot size below 200 μm, then it is constant and decreases slowly for spot size larger than 500 μm. This decrease can be related to the fact that for such large spot size a part of the laser radiation is lost because it enters outside the 1×1 mm^2 active area of the antenna. The strong reduction for spot sizes below 200 μm is attributed to the nonlinear dependence of the terahertz signal at high excitation density. The solid line in Fig. 3 is the result of a calculation, where we take into account the sublinear increase displayed in Fig. 2.

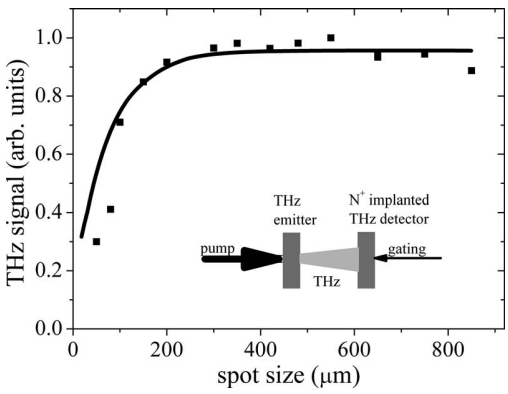

FIG. 3. Terahertz signal vs spot diameter of the gating beam at a fixed power of 70 mW on the detector. The black squares are the measured data, while the solid curve is a semiempirical calculation accounting for the nonlinear dependence between excitation density and terahertz signal (Fig 2). The inset shows the experimental configuration.

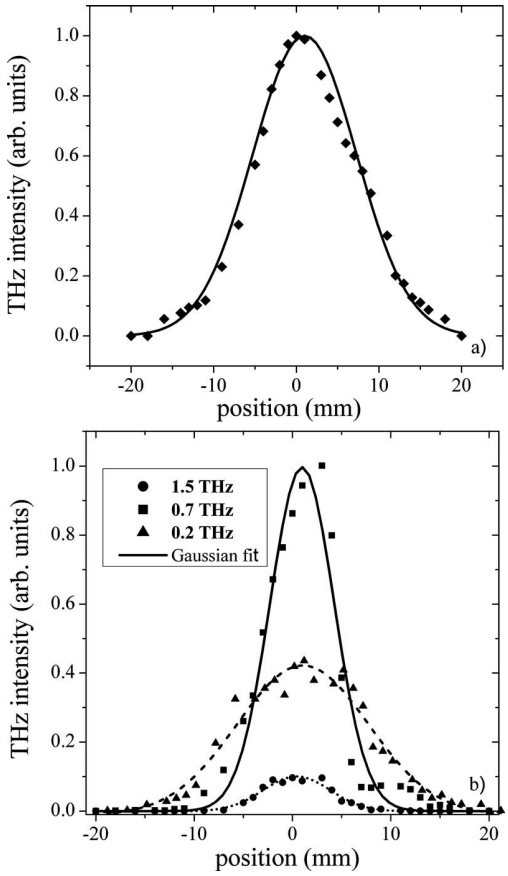

FIG. 4. (a) Measured terahertz profile. (b) Beam divergences resolved for several frequency components. Solid lines are Gaussian fits to the measured data.

Finally we take advantage of the good detector properties to characterize the spatial profile of the terahertz beam from the emitter. This is done by moving the detector and the probe beam perpendicular to the terahertz beam [Fig. 4(a)]. By transforming the measured terahertz wave forms from the time into the frequency domain for each position, we obtain the beam profiles of the emitter [Fig. 4(b)] for different frequencies. Comparing these profiles, we observe a strong increase of the beam divergence for lower frequencies. The FWHMs of the Gaussian profiles are 7.5, 7.8, and 15.2 mm at 1.5, 0.7, and 0.2 THz, respectively. This corresponds to opening angles from 15° at 1.5 THz to 32° at 0.2 THz. This divergence is smaller than expected from Gaussian beam propagation and can be described by a treatment of diffraction beyond the paraxial approximation.[15]

In conclusion, we have used an interdigitated electrode design for photoconductive terahertz detectors and compared it with electro-optic sampling. Besides the choice of the substrate material of the detector, also the beam properties of the gating laser are found to be important for optimum detection. In contrast to other PC antennas, our approach allows the use of larger spot size for gating which makes the detector more stable against misalignment and beam pointing instabilities. With these detectors we were able to measure directly, without any focusing component, the emission profile of a terahertz emitter.

The authors are grateful to A. Kolitsch for ion implantations and H. Felsmann for sample preparation.

[1]M. Tonouchi, Nat. Photonics **1**, 97 (2007).
[2]H. Liu, Y. Chen, G. J. Bastiaans, and X.-C. Zhang, Opt. Express **14**, 415 (2006).
[3]E. Castro-Camus, J. Lloyd-Hughes, M. B. Johnston, M. D. Fraser, H. H. Tan, and C. Jagadish, Appl. Phys. Lett. **86**, 254102 (2005).
[4]B. Salem, D. Morris, V. Aimez, J. Beauvais, and D. Houde, Semicond. Sci. Technol. **21**, 283 (2006).
[5]M. Mikulics, M. Marso, S. Mantl, H. Lueth, and P. Kordos, Appl. Phys. Lett. **89**, 091103 (2006).
[6]J. F. O'Hara, J. M. O. Zide, A. C. Gossard, A. J. Taylor, and R. D. Averitt, Appl. Phys. Lett. **88**, 251119 (2006).
[7]S. A. Crooker, Rev. Sci. Instrum. **73**, 3258 (2002).
[8]X. P. Gao, J. Y. Sohn, and S. A. Crooker, Appl. Phys. Lett. **89**, 122108 (2006).
[9]R. Inoue, Y. Ohno, and M. Tonouchi, Jpn. J. Appl. Phys., Part 1 **45**, 7928 (2006).
[10]S. G. Park, M. R. Melloch, and A. M. Weiner, Appl. Phys. Lett. **73**, 3184 (1998).
[11]A. Dreyhaupt, S. Winnerl, T. Dekorsy, and M. Helm, Appl. Phys. Lett. **86**, 121114 (2005).
[12]J. F. Ziegler, J. P. Biersack, and U. Littmark, *The Stopping and Range of Ions in Solids* (Pergamon, New York, 1985), Vol. 1, http://www.srim.org/.
[13]A. Dreyhaupt, S. Winnerl, M. Helm, and T. Dekorsy, Opt. Lett. **31**, 1546 (2006).
[14]D. S. Kim and D. S. Citrin, Appl. Phys. Lett. **88**, 161117 (2006).
[15]S. Winnerl (unpublished).

APPLIED PHYSICS LETTERS **91**, 191116 (2007)

Two-photon photocurrent spectroscopy of electron intersubband relaxation and dephasing in quantum wells

Harald Schneider[a)]
Forschungszentrum Dresden Rossendorf, Institute of Ion Beam Physics and Materials Research, P.O. Box 510119, 01314 Dresden, Germany and Fraunhofer Institute for Applied Solid State Physics, Tullastrasse 72, D-79108 Freiburg, Germany

Thomas Maier and Martin Walther
Fraunhofer Institute for Applied Solid State Physics, Tullastrasse 72, D-79108 Freiburg, Germany

H. C. Liu
Institute for Microstructural Sciences, National Research Council, Ottawa K1A 0R6, Canada

(Received 9 October 2007; accepted 18 October 2007; published online 8 November 2007)

Resonantly enhanced nonlinear absorption between conduction subbands in InGaAs/AlGaAs quantum wells induces a two-photon photocurrent under femtosecond excitation, which is exploited to determine electron intersubband relaxation and dephasing times. The approach allows us to study systematically the dependence of these time constants on structural parameters, including carrier density and modulation/well doping, and to discriminate between different scattering processes.
 [DOI: 10.1063/1.2806963]

Knowing the dynamics of intersubband transitions in quantum wells (QW) is crucial for optimizing quantum well infrared photodetectors[1] (QWIP) and quantum cascade lasers.[2] In addition, intersubband transitions in QWs constitute a model system to study basic concepts in semiconductor physics, including scattering,[3] many-particle effects,[4] quantum interference,[5] and coherent transport.[6] While most investigations have concentrated on linear spectroscopy of intersubband transitions, an increasing body of research efforts has focused on nonlinear optical studies, including harmonic generation,[7] pump-probe,[8–11] and four-wave mixing.[10,11]

We have previously demonstrated two-photon photodetection involving three equidistant energy levels $|1\rangle$, $|2\rangle$, and $|3\rangle$, namely, two bound states at energies E_1 and E_2, and one continuum resonance at energy E_3.[12,13] In contrast to QWIPs, where transitions from a bound state to a continuum resonance leads to a linear photocurrent, the three-level configuration requires two photons to generate a photocurrent (inset of Fig. 2). Therefore, the photocurrent scales quadratically with the incident power, which has been verified down to excitation densities as low as 0.1 W/cm^2.[12] This quadratic behavior allows for interferometric autocorrelation measurements under femtosecond excitation, and to determine the intersubband relaxation time T_1 and dephasing time T_2. Based on the third-order nonlinear susceptibility $\chi^{(3)}$, this approach provides an interesting alternative to four-wave mixing experiments for studying the dynamics of intersubband excitations.

In the present letter, we investigate systematically the influence of dopant concentration and distribution on the intersubband dynamics in InGaAs/AlGaAs QWs by interferometric two-photon photocurrent autocorrelation measurements.

The samples are based on modulation-doped and well-doped $In_{0.10}Ga_{0.90}As/Al_{0.31}Ga_{0.69}As$ multiple QW structures grown by molecular beam epitaxy (MBE) on [100]-oriented semi-insulating GaAs substrates. The active region, designed for a transition energy E_2-E_1 of about 150 meV, consists of 20 periods of 7.3 nm wide QWs separated by 46 nm wide barriers, and is embedded between *n*-type contact layers. For samples 1–3, nominally the central 5 nm of each QW are Si doped, whereas for sample 4, the QWs are modulation doped by incorporating 2 nm of Si-doped AlGaAs subsequent to 12 nm of undoped AlGaAs in each barrier, with doping concentrations as summarized in Table I. The wafers were processed into mesa detectors of 120×120 and 240×240 μm^2 in area with Ohmic contact metallization covering the top of the mesas. For photocurrent measurements, the radiation is coupled into the structures via 45° facets in order to provide an electric field component parallel to the quantized direction.[1] The actual doping concentrations, also given in Table I, have been measured by secondary-ion mass spectroscopy (SIMS).

Figure 1(a) shows intersubband absorption spectra of the as-grown layer structures involving the $|1\rangle\rightarrow|2\rangle$ transition, measured at a temperature of 77 K in Brewster angle geometry using a Fourier-transform infrared (FTIR) spectrometer. Also shown are fit functions yielding the Lorentzian full width at half maximum broadenings Γ_L given in Table I. The spectra in Fig. 1(a) indicate a characteristic increase of transition energy with increasing carrier density, which is attributed to many-particle effects.[1,4]

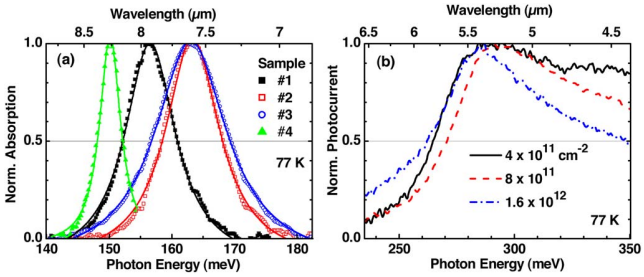

FIG. 1. (Color online) Normalized absorption spectra (a) of the $|1\rangle\rightarrow|2\rangle$ transition in Brewster-angle geometry at 77 K and normalized photocurrent spectra (b) at an elevated temperature of 160 K. Solid lines in (a) indicate Lorentzian fits to the experimental spectra.

[a)]Electronic mail: h.schneider@fzd.de

TABLE I. Doping concentrations (nominal and as determined by SIMS), measured transition energy E_2-E_1 and peak wavelength λ_{peak}, Lorentzian linewidth Γ_L, and relaxation times T_1 and T_2 of the investigated samples.

Sample	Nominal/SIMS doping (10^{11} cm^{-2})	E_2-E_1 (meV)	Γ_L (meV)	T_1 (fs)	T_2 (fs)
1	4/4.4 (well doped)	156.6	9.8	420	130
2	8/6.6 (well doped)	163.2	11.0	410	100
3	16/13.4 (well doped)	162.9	14.0	360	75
4	2/1.9 (mod doped)	150.0	4.4	640	260

Further information on the subband spacings is obtained from photocurrent spectroscopy at higher temperature (160 K), where photons at energy $h\nu=E_3-E_2$ produce a linear photocurrent since sufficient carriers are excited into level $|2\rangle$. After amplification by a transimpedance amplifier, photocurrent spectra are readily obtained using a standard FTIR spectrometer. Figure 1(b) shows photocurrent spectra of the well-doped structures. Interestingly, relatively narrow photocurrent peaks, only about 50% wider than those of the absorption measurement, are observed at the essentially degenerate energies of the $|1\rangle\rightarrow|2\rangle$ and $|2\rangle\rightarrow|3\rangle$ transitions. Besides the $|2\rangle\rightarrow|3\rangle$ bound-to-continuum excitation of electrons in the thermally populated second subband, an additional contribution presumably involves the $|1\rangle\rightarrow|2\rangle$ transition of electrons with high enough kinetic energy, such that the total energy of the final state in the second subband is close to or above the barrier edge.

Even though the $|1\rangle\rightarrow|3\rangle$ transition is parity forbidden in a symmetric QW, it still leads to a finite photocurrent, since residual asymmetry is induced by the externally applied electric field and by asymmetric dopant distributions. The steplike increase at around 280 meV indicates the photoconductive energy threshold; the broad absorption line is characteristic for bound-to-continuum transitions and relaxes the conditions for resonant two-photon transitions to be observed. Due to the induced asymmetry, the $|1\rangle\rightarrow|3\rangle$ photocurrent is larger than the peak at around 160 meV since only about 0.1% of the carriers are thermally excited into the second subband at this temperature. From Fig. 1(b), the continuum resonance appears wide enough to ensure that resonantly enhanced two-photon absorption is always present as long as the photon energy matches the $|1\rangle\rightarrow|2\rangle$ transition.

To study the intersubband dynamics, pulses of 165 fs duration, tunable from 6 to 18 μm, are generated at a repetition rate of 76 MHz by difference frequency mixing of the signal and idler beams of an optical parametric oscillator.[14] Using a beam splitter and a Michelson interferometer, the samples are illuminated by collinear pulses with variable delay time. Mesurements were conducted at a temperature of 77 K, low enough to suppress the thermally activated, linear photocurrent contribution discussed above, and at moderate operation voltages in the range of 1–2 V to avoid tunneling out of the intermediate state. The latter effect comes into play at high bias voltages where it allows for electrical switching between linear and quadratic detection.[15]

Quadratic photocurrent autocorrelation traces, normalized to the signal at large time delay, are shown in Fig. 2. In these experiments, the excitation energy was chosen to match the $|1\rangle\rightarrow|2\rangle$ transition. The peak-to-background ratio close to the ideal 8:1 value confirms that the signal scales quadratically with the incident power for all samples.[12] The "ideal" autocorrelation trace as obtained by assuming transform-limited Gaussian pulses (which is a good approximation for the midinfrared pulses used in our experiments[14]) has been included in Fig. 2 for comparison.

Comparing the experimental traces with the ideal autocorrelation, two striking differences are observed.[12] First, the fringe amplitude decays exponentially with increasing delay time τ, which directly reflects the phase relaxation of the coherent *intersubband polarization*. Therefore, the associated decay constant agrees with the phase relaxation time T_2. In contrast, the ideal case (lowest panel of Fig. 2) shows a Gaussian decay of the fringes. Second, even after the fringes have disappeared, the two-photon autocorrelation signal exhibits further exponential decay towards its asymptotic value. The latter decay constant arises from the *intersubband population* associated with the population relaxation time T_1.

These considerations provide the basis for a phenomenological model introduced by Nessler *et al.*,[16] which yields an analytical solution for numerical fitting of the experimental data. In fact, the fits thus obtained exhibit satisfactory agreement with experimental autocorrelation traces.[13] This agreement is also evident from the envelope functions shown in Fig. 2, which nicely reproduce the minima and maxima of the fringes.

The observed dynamics in Fig. 2, in particular, for the decay of the oscillatory part, depends considerably on the carrier density. Yet significantly longer time constants come into play for the modulation doped device structure 4. For further analysis, Fig. 3 compares the measured dynamical parameters, namely the diagonal and off-diagonal relaxation rates T_1^{-1} and T_2^{-1}, respectively, with the decay rate $\Gamma_L/2\hbar$ associated with the $|1\rangle\rightarrow|2\rangle$ absorption linewidth. Only small deviations exist between values of $\Gamma_L/2\hbar$ and observed dephasing rates, indicating predominantly homogenous broadening (i.e., lifetime broadening) of the $|1\rangle\rightarrow|2\rangle$ transition. Residual deviations of 10%–25% between these two quantities are attributed to some additional inhomogeneous broadening contribution.

The increase of the rates T_1^{-1} and T_2^{-1} in Fig. 3 with carrier concentration constitutes clear signature for electron-impurity scattering. T_1^{-1} depends only weakly on the doping concentration, indicating that LO phonon scattering dominates over impurity scattering. Assuming a linear dependence of the impurity scattering rate τ_{imp}^{-1} on the doping concentration in our well-doped structures, linear extrapolation gives rise to $T_1^{-1}=2.13$ THz at $N_D=0$, with a slope of $\tau_{imp}^{-1}=0.45N_D$ cm^2/s. In particular, this means that about 22% of the intersubband relaxation rate is caused by impurity scattering for the highest doped sample. For the modulation-doped sample, however, T_1^{-1} is as low as 1.56 THz, significantly below the extrapolated value. Taking account of the otherwise identical MBE growth parameters, the latter observation is unexpected and not understood at present.

The dephasing rate T_2^{-1} is found to depend more strongly on the doping concentration than T_1^{-1}. Here linear extrapolation for the well-doped case yields $T_2^{-1}=5.6$ THz at $N_D=0$. The slope ($6\pm1N_D$ cm^2/s) is mainly associated with (intrasubband) ionized impurity scattering,[3] with some additional contribution from electron-electron scattering [because density dependent T_2^{-1} is known to exist also in modulation-doped QWs (Ref. 10)]. Again, the dephasing rate for the modulation-doped structure is somewhat lower than expected from linear extrapolation.

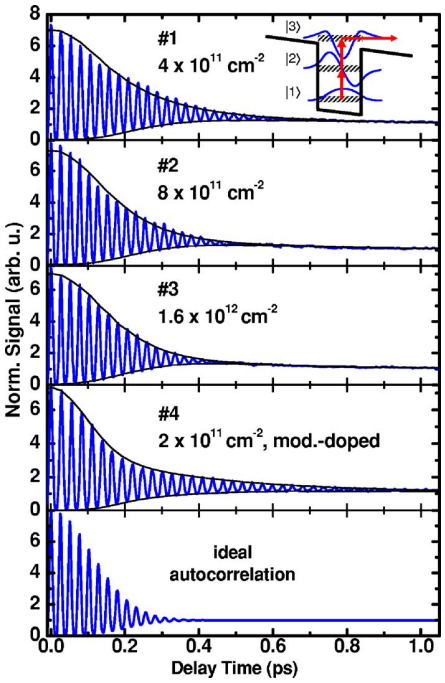

FIG. 2. (Color online) Photocurrent autocorrelation traces of samples 1–4 at 77 K and calculated ideal autocorrelation vs delay time. Relaxation times as obtained from the numerical fit (envelopes shown as thin lines) are listed in Table I. The inset shows the schematics of the two-photon QWIP.

Similar behavior is found for the linewidth parameter ($\Gamma_L/2\hbar$=6 THz at N_D=0, slope $3.5\pm1 N_D$ cm^2/s). Apparently, well doping leads to extra broadening which remains finite also at low density. We attribute this extra impurity-induced broadening to the dependence of the impurity binding energy on the dopant position along the growth direction,[17] which in turn influences the subband energies.[18] Since the correlation length associated with the impurity potentials, which is of the order of the mean impurity spacing, is still below the electronic scattering length for the carrier densities under consideration, the associated broadening is expected to be homogeneous (see also the discussion in Ref. 3 for the case of interface roughness scattering).

Since the dephasing directly relates to Γ_L for a homogeneously broadened transition, the observed doping dependence of T_2^{-1} is consistent with the line broadenings and can thus be qualitatively understood from the underlying scattering processes. We note that the observed large T_1 value for modulation doping cannot be traced back to impurity-induced broadening, since this process should only affect the coherence time and be of negligible influence for intersubband scattering.

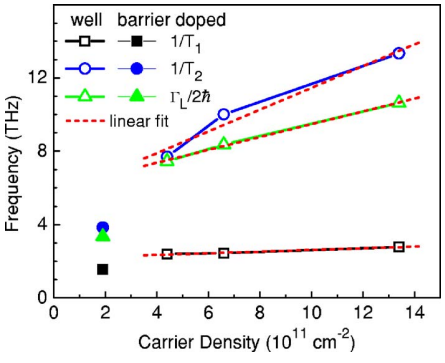

FIG. 3. (Color online) Population decay rate $1/T_1$, dephasing rate $1/T_2$, and line broadening $\Gamma_L/2\hbar$ vs carrier density.

To check the temperature dependence, we have also performed intensity autocorrelation measurements on sample 1 at higher temperatures up to 150 K (not shown) and found only a slight decrease of T_1 from 420 to 390 fs. This is consistent with the expected behavior of emission rates associated with the Fröhlich interaction.[19]

In conclusion, femtosecond dynamics of intersubband transitions in $In_{0.10}Ga_{0.90}As/Al_{0.31}Ga_{0.69}As$ QWs has been studied by interferometric two-photon photocurrent autocorrelation measurements. The approach has been used to investigate population and phase relaxation times, in particular, their dependence on impurity concentration and impurity location, and to discriminate between different scattering processes. Knowing these dependencies will be crucial for further optimization of intersubband detectors, emitters, and modulators.

The authors are grateful to M. Maier (Freiburg) for SIMS measurements and to P. Koidl (Freiburg) and M. Helm (Dresden) for helpful discussions. HCL thanks the Alexander von Humboldt foundation for the Bessel Award and the renewed research stay in Dresden.

[1] H. Schneider and H. C. Liu, *Quantum Well Infrared Photodetectors: Physics and Applications*, Springer Series in Optical Sciences Vol. 126 (Springer, Heidelberg, 2006).
[2] C. Sirtori and R. Teissier, in *Intersubband Transitions in Quantum Structures*, edited by R. Paiella (McGraw-Hill, New York, 2006), Chap. 1, pp. 1–44.
[3] T. Unuma, M. Yoshita, T. Noda, H. Sakaki, and H. Akiyama, J. Appl. Phys. **93**, 1586 (2003).
[4] M. Helm, in *Intersubband Transition in Quantum Wells: Physics and Device Applications I*, Semiconductors and Semimetals Vol. 62, edited by H. C. Liu and F. Capasso (Academic, New York, 2000), Chap. 1, p. 199.
[5] J. Faist, F. Capasso, C. Sirtori, D. L. Sivco, and A. Y. Cho, in *Intersubband Transition in Quantum Wells: Physics and Device Applications I*, Semiconductors and Semimetals Vol. 62, edited by H. C. Liu and F. Capasso (Academic, New York, 2000), Chap. 2, pp. 101–128.
[6] C. Schönbein, H. Schneider, and M. Walther, Phys. Rev. B **60**, R13993 (1999).
[7] C. Sirtori, F. Capasso, D. L. Sivco, and A. Y. Cho, in *Intersubband Transition in Quantum Wells: Physics and Device Applications I*, Semiconductors and Semimetals Vol. 66, edited by H. C. Liu and F. Capasso (Academic, New York, 2000), Chap. 2, pp. 85–125.
[8] J. Hamazaki, H. Kunugita, K. Ema, A. Kikuchi, and K. Kishino, Phys. Rev. B **71**, 165334 (2005).
[9] C. V.-B. Tribuzy, S. Ohser, S. Winnerl, J. Grenzer, H. Schneider, M. Helm, J. Neuhaus, T. Dekorsy, K. Biermann, and H. Künzel, Appl. Phys. Lett. **89**, 171104 (2006).
[10] R. A. Kaindl, K. Reimann, M. Woerner, T. Elsaesser, R. Hey, and K. H. Ploog, Phys. Rev. B **63**, 161308(R) (2001).
[11] T. Elsaesser, in *Intersubband Transitions in Quantum Structures*, edited by R. Paiella (McGraw-Hill, New York, 2006), Chap. 4, pp. 135–180.
[12] H. Schneider, T. Maier, H. C. Liu, M. Walther, and P. Koidl, Opt. Lett. **30**, 287 (2005).
[13] T. Maier, H. Schneider, H. C. Liu, M. Walther, and P. Koidl, Infrared Phys. Technol. **47**, 182 (2005).
[14] S. Ehret and H. Schneider, Appl. Phys. B: Lasers Opt. **66**, 27 (1998).
[15] T. Maier, H. Schneider, H. C. Liu, M. Walther, and P. Koidl, Appl. Phys. Lett. **88**, 051117 (2006).
[16] W. Nessler, S. Ogawa, H. Nagano, H. Petek, J. Shimoyama, Y. Nakayama, and K. Kishio, J. Electron Spectrosc. Relat. Phenom. **88**, 495 (1998).
[17] G. Bastard, Phys. Rev. B **24**, 4714 (1981).
[18] D. Stehr, C. Metzner, M. Helm, T. Roch, and G. Strasser, Phys. Rev. Lett. **95**, 257401 (2005).
[19] R. Ferreira and G. Bastard, Phys. Rev. B **40**, 1074 (1989).

APPLIED PHYSICS LETTERS **91**, 191121 (2007)

Intersubband relaxation dynamics in single and double quantum wells based on strained InGaAs/AlAs/AlAsSb

C. V.-B. Grimm,[a] M. Priegnitz, S. Winnerl, H. Schneider, and M. Helm
Institute of Ion Beam Physics and Materials Research, Forschungszentrum Dresden Rossendorf, P.O. Box 510119, 01314 Dresden, Germany

K. Biermann and H. Künzel
Fraunhofer Institute for Telecommunications (Heinrich Hertz Institut), 10587 Berlin, Germany

(Received 24 September 2007; accepted 22 October 2007; published online 9 November 2007)

Intersubband relaxation dynamics in single and coupled double quantum well (QW) structures based on strained InGaAs/AlAs/AlAsSb are studied by femtosecond pump probe spectroscopy at wavelengths around 2 μm. For single QWs, the transient transmission was observed to decay exponentially with a time constant of 2 ps, showing that side valleys have negligible influence on the intersubband relaxation dynamics for strained InGaAs QWs. For double QWs, the pump-probe signal at the intersubband energy involving the two electronic levels located at the wider QW exhibits an induced absorption component attributed to the population of the second subband (associated with the narrow QW) by hot electrons. © *2007 American Institute of Physics*.
[DOI: 10.1063/1.2809409]

In recent years intersubband transitions (ISBT) in quantum wells (QW) have found applications in quantum cascade lasers.[1] Due to the associated relaxation times in the picosecond and subpicosecond regimes, intersubband transitions also appear promising for ultrafast all-optical switches.[2] In particular, for applications at short wavelengths, where high conduction band offsets are required, promising material systems include strained InGaAs/AlAs on InP (Ref. 3) and GaAs (Ref. 4) substrates, $In_{0.53}Ga_{0.47}As/AlAs_{0.56}Sb_{0.44}$ lattice matched to InP,[5,6] strain compensated InGaAs/AlAs/AlAsSb controlling either the quantum well[7] or the barrier[8] composition, InAs/AlSb on GaSb,[9] nitrides such as InGaN/AlGaN,[10] and II-VI compounds such as ZnSe/BeTe.[11] Although InP (Refs. 12 and 13) or GaSb (Ref. 9) based systems appear more promising for application in quantum cascade emitters, approaching wavelengths as short as the telecom range requires special considerations. One aspect is related to the presence of energy levels of indirect valleys located above the upper lasing state. This has been shown to inhibit sufficient population inversion and lasing in GaAs/AlGaAs quantum cascade letters.[14] On the other hand, the inefficiency of intervalley transfer was recently pointed out for ISBT wavelengths as short as 2.3 μm (Ref. 6) in $In_{0.53}Ga_{0.47}As/AlAs_{0.56}Sb_{0.44}$, when in principle the Γ-X or L crossover already took place ($\lambda \leqslant 3.7$ μm). In addition, quantum cascade lasers with wavelength around 3.0 μm, using the same material, were demonstrated.[15] The other aspect is the inherent difficulty to grow very thin QW where the interface imperfections become very important. Cristea *et al.*[16] have demonstrated a lower limit of 1.76 μm for ISBT achieved in strain compensated InGaAs/AlAs/AlAsSb single QW (SQW). With the aim to achieve even shorter wavelengths, coupled quantum wells have been employed since their band configuration gives rise to four subbands and transitions between all of them are possible. The relaxation dynamics involving specifically the transition between the most apart subbands was studied,[17] aiming at the realization of ultrafast all-optical switches at communication wavelengths.[18] Also in quantum cascade lasers, one takes an advantage of coupled QWs states, permitting transport along the cascaded structure. A detailed knowledge of the relaxation dynamics in these systems is very important.

In this work, we present a study of the intersubband relaxation dynamics of an asymmetric coupled double quantum well (DQW) sample (with two different QW thicknesses) based on strained InGaAs/AlAs/AlAsSb through degenerate pump-probe measurements. The relaxation dynamics is found to be more complex than for a SQW sample used as a reference, where the usual induced transmission is observed. The DQW sample shows an induced absorption due to the presence of different intersubband transitions. In addition, we point out the negligible influence of side valleys on the intersubband relaxation dynamics when strained InGaAs QW are employed.

The samples were grown by molecular beam epitaxy at a temperature of 480 °C on InP substrate. More details about the growth conditions are published elsewhere.[19] Both structures contain two monolayers of AlAs at each InGaAs/AlAsSb interface with the intention to reduce the diffusion and segregation effects.[19] In order to compensate the thus generated tensile strain, the QWs are grown with a higher In content and are compressively strained. The DQW sample consists of 40 periods of 2.35 and 1.76 nm wide $In_{0.82}Ga_{0.18}As$ QWs separated by a 1.14 nm (4 ML) AlAs central barrier (nominal thicknesses). The outer barriers are 5.9 nm lattice matched AlAsSb. Both QWs are doped with Si yielding a total areal electron concentration of 1.6×10^{12} cm^{-2} per period. The SQW sample consists of 40 periods of 2.35 nm $In_{0.78}Ga_{0.22}As$ QWs and 5.9 nm lattice matched $AlAs_{0.56}Sb_{0.44}$ barriers. The QWs are also doped with Si yielding an areal electron concentration of 8.7×10^{11} cm^{-2} per period. The geometry of the samples for the optical measurements is consisted of short trapezoidal waveguides with 38° polished facets.

[a]Tel.: ++49 351 260 2494. Fax: ++49 351 260 12342. Electronic mail: c.grimm@fzd.de

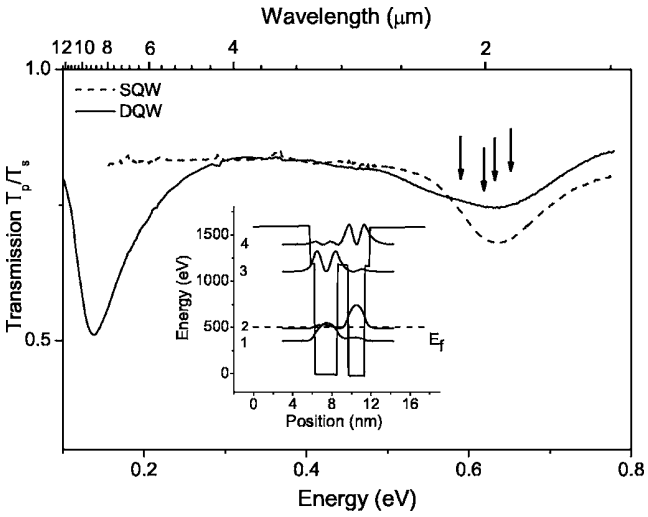

FIG. 1. Ratios between *p*- and *s*-polarized transmission spectra of the investigated samples obtained by Fourier transform infrared spectroscopy (FTIR) at 300 K. The arrows indicate the excitation wavelengths. The inset shows the self-consistent conduction band edge profile at the Γ point for the DQW sample. The probability densities of the subband states are also shown.

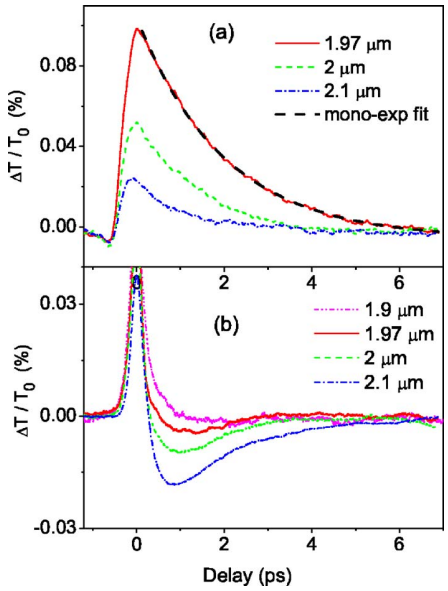

FIG. 2. (Color online) Relative probe transmission change $\Delta T/T_0$ as a function of the delay between the pump and probe pulses for different pulse wavelengths of the SQW (a) and DQW (b) samples. The monoexponential fit was done for the curve measured with an excitation wavelength equal to 1.97 μm.

Figure 1 shows the ratios between *p*- and *s*-polarized transmission spectra of the investigated samples obtained by Fourier transform infrared spectroscopy (FTIR) at 300 K. The DQW sample shows a very strong absorption at low energy (139 meV ≙ 8.9 μm) coming from the 1–2 transition (see inset). We will not focus our attention to this transition. The absorption occurring at higher energies arises from the 1–3 transition (see inset). Its maximum of absorption coincides with that from the SQW sample (around 1.95 μm) but appears much broader toward the low energy side. This fact will be discussed later in more detail.

The pump-probe measurements were performed using femtosecond optical pulses of about 240 fs duration generated at 78 MHz repetition rate by an optical parametric oscillator tunable from 1.3 to 3.2 μm. A small angle between the pump and probe beams, which were polarized parallel to the growth direction, was used in order to separate both beams. For the measurements a scanning delay generator (shaker) between the pump and probe beams was operated at a frequency of 48 Hz and the signal, detected by an InGaAs detector, was accumulated with a fast analog to digital converter (fast-scanning technique). The measurements were performed at room temperature. The pump-pulse energy was about 105 pJ at wavelengths varying from 1.9 to 2.1 μm.

Figure 2 shows the relative probe transmission change $\Delta T/T_0$ of the SQW (a) and DQW (b) samples at different excitation wavelengths as a function of the delay between the pump and probe pulses. The excitation wavelengths are within the intersubband absorption line of interest as indicated by the arrows in Fig. 1. The SQW sample shows an induced transmission due to the bleaching of the transition. The change of the transmission with delay time follows a single exponential, as shown in Fig. 2(a), for the measurement performed at a wavelength of 1.97 μm (central spectral position of the linear absorption). For this curve the decay time is 2 ps.

We note that for the present QW material ($In_{0.82}Ga_{0.18}As$ and $In_{0.78}Ga_{0.22}As$, respectively), the energy difference between Γ and side valley minima is expected to be more than 100 meV larger than for (unstrained) $In_{0.53}Ga_{0.47}As$.[20] Therefore, the side valleys have negligible influence on the intersubband relaxation dynamics in the present experiments, giving rise to single-exponential behavior. This is in contrast to $In_{0.53}Ga_{0.47}As$ QWs, where intervalley scattering gives rise to biexponential relaxation of the pump-probe signal at similar excitation wavelengths.[6]

For the DQW sample, we observed an induced absorption instead of an induced transmission even for an excitation wavelength at the central spectral position of the linear absorption. With increasing wavelength we observe further enhancement of the induced absorption. The wider QW of the DQW sample being of the same thickness as the SQW, one should not expect such drastic change of the relaxation dynamics since the 1–3 transition of the DQW essentially corresponds to the intersubband transition of the SQW. The sharp peak occurring around 0 ps is attributed to a coherent artifact,[6] which will not be discussed here further.

One possible explanation for the induced absorption observed could be associated with the large nonparabolicity present in such thin QWs,[21] and with the effective mass associated with excited subbands being larger than those of the lowest one. In fact, the intersubband energy thus decreases with increasing in-plane momentum, such that longer excitation wavelengths are absorbed by electrons which have relaxed to the Fermi sea but are thermalized at a temperature above the lattice temperature. This would result in an induced absorption of the probe which increases with excitation wavelength. This effect was already observed before, e.g., in GaN/AlN multiple QWs.[10] However, if this mechanism is effective, the same behavior should occur for the SQW sample, which is not observed in our experiments.

We thus suggest a different mechanism which relies on the specific subband structure of our DQW structure. To this end, let us first discuss its conduction band edge profile, which was calculated at the Γ minimum by a self-consistent solution of the Schrödinger and Poisson equations, including

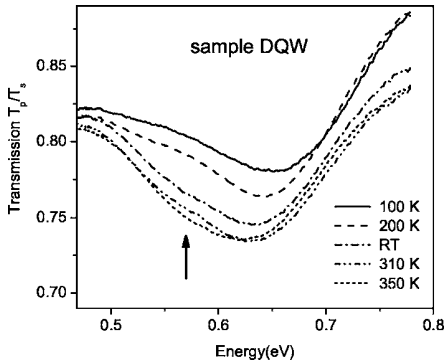

FIG. 3. Transmission spectra as a function of temperature for the DQW sample. The arrow indicates a shoulder at the lower energy side corresponding to the 2–3 transition energy.

nonparabolicity as described in Ref. 22. The result is shown in the inset on Fig. 1, as well as the squared moduli of the four subband wavefunctions. The Fermi level, indicated by the dashed line, is only about 13 meV above level 2. By calculation, only about 6% of the electrons are thus located in level 2 at room temperature. Drawing our attention back to the FTIR spectrum of the DQW sample in Fig. 1, the shoulder of the linear absorption at around 2.5 μm provides an evidence that the 2–3 transition in fact contributes to the absorption.

Our proposed mechanism relies on the increase in electron temperature which is present after the bleaching of the 1–3 transition and intersubband relaxation. The elevated electron temperature increases the population of level 2, thus inducing absorption of the probe beam via the 2–3 transition. This mechanism is dominant when competing with transmission due to the 1–3 transition, and therefore a negative component of the probe transmission change is observed. By increasing the wavelength, the excitation matches better the 2–3 transition and the induced absorption is higher. For shorter excitation wavelengths ($\lambda = 1.9$ μm) we access the lower energy region of the $n=1$ subband, and there some induced transmission can be observed. For the pump-probe curve that shows maximum induced absorption, a monoexponential decay with time constant of 1.6 ps is found for the relaxation of this component. Similar induced absorption has been observed recently in GaAs/AlGaAs superlattices[23] enabled by the large spectral spreading of the interminiband absorption and its temperature dependence.

As complementary evidence that another transition takes place when carriers have temperature higher than the lattice temperature, we show in Fig. 3 FTIR measurements as a function of temperature performed at the DQW sample. The figure highlights the region where the absorption between levels 1 and 3 occurs. The increase of the temperature gives rise to a shoulder (indicated by the arrow) at the lower energy side, which corresponds to the 2–3 transition energy in accordance with the band structure calculations.

In conclusion, degenerate pump-probe measurements were carried out in single and coupled double well samples based on strained InGaAs/AlAs/AlAsSb. In the single QW, we observed a single-exponential decay of the transient transmission showing that, in contrast to lattice matched InGaAs QWs, side valleys have negligible influence on the intersubband relaxation dynamics for the strained material. In the double QW, for the transition involving the two electronic levels inside the wider QW, we observed an induced absorption rather than transmission due to the population of level 2, localized inside the narrower QW, by hot electrons as a result of the location of the Fermi level slightly above this level. The possibility of having not only bleaching but also induced absorption opens up another degree of freedom for the design of ultrafast optical switches at telecommunication wavelengths.

C.V.-B.G. acknowledges support from the Alexandervon Humboldt Foundation.

[1] *Intersubband Transitions in Quantum Wells: Physics and Device Applications, Semiconductors and Semimetals*, Vols. 62 and 66, edited by H. C. Liu and F. Capasso (Academic, San Diego, 2000).
[2] R. Akimoto, B. S. Li, K. Akita, and T. Hasama, Appl. Phys. Lett. **87**, 181104 (2005).
[3] N. Georgiev, T. Dekorsy, F. Eichhorn, M. Helm, M. P. Semtsiv, and W. T. Masselink, Appl. Phys. Lett. **83**, 210 (2003).
[4] G. Ghislotti, E. Riedo, D. Ielmini, and M. Martinelli, Appl. Phys. Lett. **75**, 3626 (1999).
[5] T. Mozume, J. Kasai, N. Georgiev, T. Simoyama, A. V. Gopal, and H. Yoshida, Jpn. J. Appl. Phys., Part 1 **42**, 5500 (2003).
[6] C. V.-B. Tribuzy, S. Ohser, S. Winnerl, J. Grenzer, H. Schneider, M. Helm, J. Neuhaus, T. Dekorsy, K. Biermann, and H. Künzel, Appl. Phys. Lett. **89**, 171104 (2006).
[7] J. Kasai and T. Mozume, J. Cryst. Growth **278**, 183 (2005).
[8] M. Nagase, T. Mozume, T. Simoyama, T. Hasama, and H. Ishikawa, J. Cryst. Growth **301/302**, 240 (2007).
[9] D. Barate, R. Teissier, Y. Wang, and A. N. Baranov, Appl. Phys. Lett. **87**, 051103 (2005).
[10] J. Hamazaki, H. Kunugita, K. Ema, A. Kikuchi, and K. Kishino, Phys. Rev. B **71**, 165334 (2005).
[11] R. Akimoto, K. Akita, F. Sasaki, and T. Hasama, Appl. Phys. Lett. **81**, 2998 (2002).
[12] M. P. Semtsiv, M. Ziegler, S. Dressler, W. T. Masselink, N. Georgiev, T. Dekorsy, and M. Helm, Appl. Phys. Lett. **85**, 1478 (2004).
[13] Q. Yang, C. Manz, W. Bronner, K. Köhler, and J. Wagner, Appl. Phys. Lett. **88**, 121127 (2006).
[14] L. R. Wilson, D. A. Carder, J. W. Cockburn, R. P. Green, D. G. Revin, M. J. Steer, M. Hopkinson, G. Hill, and R. Airey, Appl. Phys. Lett. **81**, 1378 (2002).
[15] D. G. Revin, J. W. Cockburn, M. J. Steer, R. J. Airey, M. Hopkinson, A. B. Krysa, L. R. Wilson, and S. Menzel, Appl. Phys. Lett. **90**, 021108 (2007).
[16] P. Cristea, Y. Fedoryshyn, J. F. Holzman, F. Robin, H. Jäckel, E. Müller, and J. Faist, J. Appl. Phys. **100**, 116104 (2006).
[17] T. Akiyama, N. Georgiev, T. Mozume, H. Yoshida, A. V. Gopal, and O. Wada, Electron. Lett. **37**, 129 (2001).
[18] H. Yoshida, T. Simoyama, A. V. Gopal, J. Kasai, T. Mozume, and H. Ishikawa, IEICE Trans. Electron. **E87C**, 1134 (2004).
[19] K. Biermann, H. Künzel, C. V.-B. Tribuzy, S. Ohser, H. Schneider, and M. Helm, Proceedings of the 19th International Conference on Indium Phosphide and Related Materials (IPRM'07), Matsue, Japan, 2007, p. 498.
[20] D. G. Revin, J. W. Cockburn, M. J. Steer, R. J. Airey, M. Hopkinson, A. B. Krysa, L. R. Wilson, and S. Menzel, Appl. Phys. Lett. **90**, 151105 (2007).
[21] H. Ishikawa, H. Tsuchida, K. S. Abedin, T. Simoyama, T. Mozume, M. Nagase, R. Akimoto, T. Miyazaki, and T. Hasama, Jpn. J. Appl. Phys. **46**, L157 (2007).
[22] P. Harrison, *Quantum Wells, Wires and Dots—Theoretical and Computational Physics of Semiconductor Nanostructures*, 2nd ed. (Wiley-Interscience, Chichester, England, 2005).
[23] D. Stehr, S. Winnerl, M. Helm, T. Dekorsy, T. Roch, and G. Strasser, Appl. Phys. Lett. **88**, 151108 (2006).

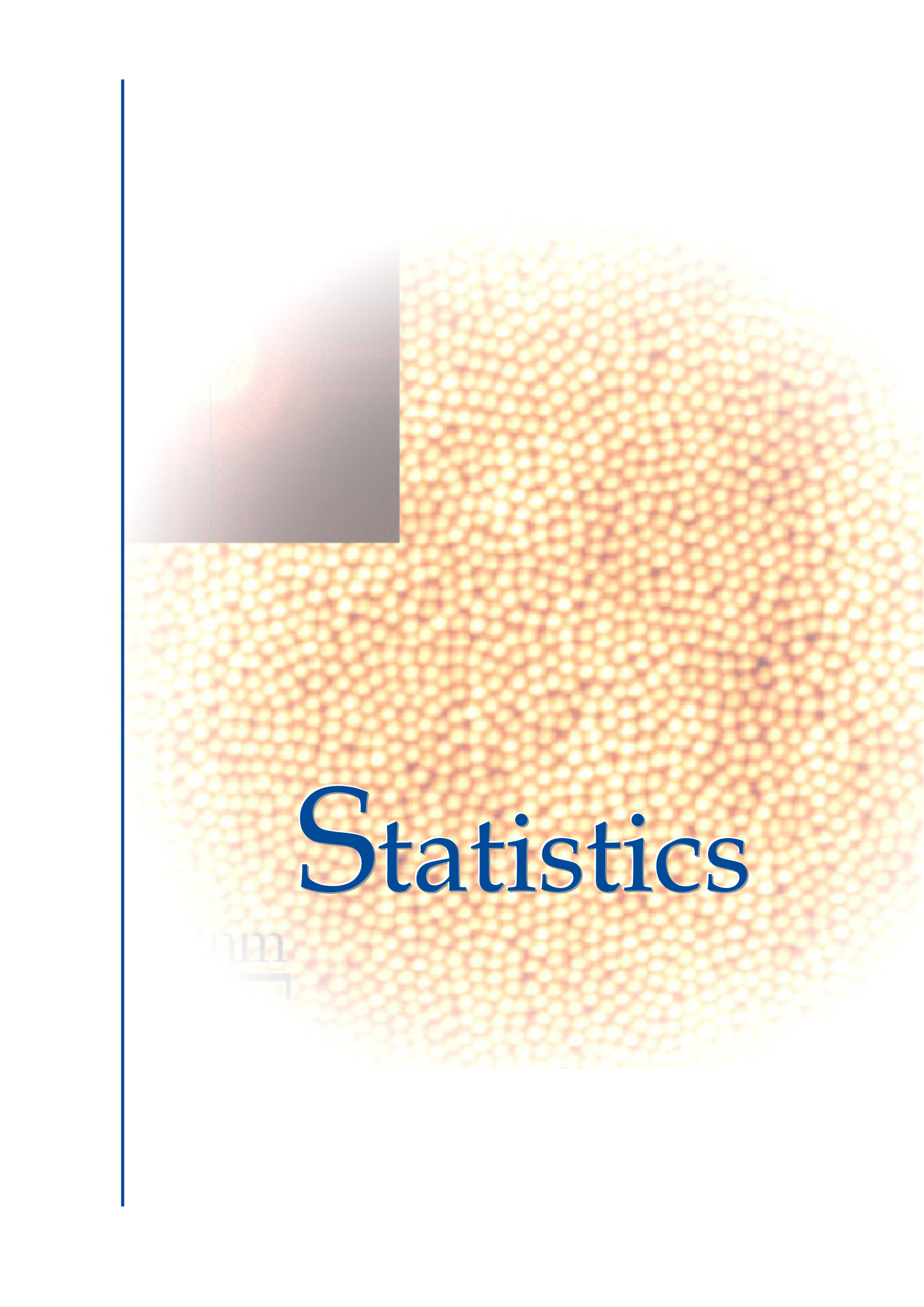
Statistics

Monographs & Book Chapters

1. Gemming, S.; Schreiber, M.; Suck, J.-B. (Editors)
Materials for Tomorrow
Berlin - Heidelberg - New York: Springer, 2007, 978-3-540-47970-3, 212 pages

2. Enyashin, A. N.; Gemming, S.; Seifert, G.
Simulation of inorganic nanotubes
in S. Gemming, M. Schreiber, J.-B. Suck, Materials for Tomorrow, Berlin - Heidelberg - New York: Springer, 2007, 978-3-540-47970-3, pp. 33-57

3. Gemming, S.; Schreiber, M.
Theoretical investigation of interfaces
in S. Gemming, M. Schreiber, J.-B. Suck, Materials for Tomorrow, Berlin - Heidelberg - New York: Springer, 2007, 978-3-540-47970-3, pp. 91 - 122

Publications

Ion-Solid-Interaction

1. Facsko, S.; Kost, D.; Keller, A.; Möller, W.; Pesic, Z.; Stolterfoht, N.
Interaction of highly charged ions with the surface of insulators
Radiation Physics and Chemistry ***76****, 387 (2007).*

2. Grambole, D.; Herrmann, F.; Heera, V.; Meijer, J.
Study of crystal damage by ion implantation using micro RBS/Channeling
Nuclear Instruments and Methods in Physics Research B ***260****, 276 (2007).*

3. Grynszpan, R. I.; Brauer, G.; Anwand, W.; Malaquin, L.; Saudé, S.; Vickridge, I.; Briand, E.
Radiation damage in zirconia investigated by positively charged particles
Nuclear Instruments and Methods in Physics Research B ***261****, 888 (2007).*

4. Güttler, D.; Grötzschel, R.; Möller, W.
Lateral variation of target poisoning during reactive magnetron sputtering
Applied Physics Letters ***90****, 263502 (2007).*

5. Kost, D.; Facsko, S.; Möller, W.; Hellhammer, R.; Stolterfoht, N.
Channels of potential energy dissipation during multiply charged argon ion bombardment of copper
Physical Review Letters ***98****, 225503 (2007).*

6. Kost, D.; Röder, F.; Möller, W.
Deposition and re-emission of potential energy - extended dynamical COB simulation
Journal of Physics: Conference Series ***58****, 343 (2007).*

7. Möller, W.; Güttler, D.
Modeling of plasma-target interaction during reactive magnetron sputtering of TiN
Journal of Applied Physics ***102****, 094501 (2007).*

8. Shiryaev, A. A.; Grambole, D.; Rivera, A.; Herrmann, F.
On the interaction of molecular hydrogen with diamonds: An experimental study using nuclear probes and thermal desorption
Diamond and Related Materials ***16****, 1479 (2007).*

9. Zschornack, G.; Grossmann, F.; Heller, R.; Kentsch, U.; Kreller, M.; Landgraf, S.; Ovsyannikov, V. P.; Schmidt, M.; Ullmann, F.
Production of highly charged ions for ion-surface interaction studies
Nuclear Instruments and Methods in Physics Research B ***258****, 205 (2007).*

Thin Films

10. Abd El-Rahman, A. M.; Maitz, M. F.; Kassem, M. A.; El-Hossary, F.; Prokert, F.; Reuther, H.; Pham, M. T.; Richter, E.
Surface improvement and biocompatibility of TiAl24Nb10 intermetallic alloy using rf plasma nitriding
Applied Surface Science ***253****, 9067 (2007).*

11. Abendroth, B.; Jäger, H. U.; Möller, W.; Bilek, M.
Binary-collision modeling of ion-induced stress relaxation in cubic BN and amorphous C thin films
Applied Physics Letters ***90****, 181910 (2007).*

12. Abrasonis, G.; Krause, M.; Mücklich, A.; Sedlackova, K.; Radnoczi, G.; Kreissig, U.; Kolitsch, A.; Möller, W.
Growth regimes and metal enhanced 6-fold ring clustering of carbon in carbon-nickel composite thin films
Carbon ***45****, 2995 (2007).*

13. Beckers, M.; Schell, N.; Martins, R. M. S.; Mücklich, A.; Möller, W.; Hultman, L.
Nucleation and growth of Ti_2AlN thin films deposited by reactive magnetron sputtering onto MgO(111)
Journal of Applied Physics ***102****, 074916 (2007).*

14. Blomqvist, M.; Bongiorno, G.; Podesta, A.; Serin, V.; Abrasonis, G.; Kreissig, U.; Möller, W.; Coronel, E.; Wachtmeister, S.; Csillag, S.; Cassina, V.; Piseri, P.; Milani, P.
Structural and tribological properties of cluster-assembled CN_x films
Applied Physics A ***87****, 767 (2007).*

15. Borras, A.; Lopez, C.; Rico, V.; Gracia, F.; Gonzalez-Elipe, A.; Richter, E.; Battiston, G.; Gerbasi, R.; McSporran, N.; Sauthier, G.; Gyorgy, E.; Figueras, A.
Effect of visible and UV illumination on the water contact angle of TiO_2 thin films with incorporated nitrogen
Journal of Physical Chemistry C ***111****, 1801 (2007).*

16. Cizek, J.; Prochazka, I.; Danis, S.; Melikhova, O.; Vlach, M.; Zaludova, N.; Brauer, G.; Anwand, W.; Mücklich, A.; Gemma, R.; Nikitin, E.; Kirchheim, R.; Pundt, A.
Positron annihilation study of hydrogen trapping at open-volume defects: Comparison of nanocrystalline and epitaxial Nb thin films
Journal of Alloys and Compounds ***446****, 484 (2007).*

17. Cizek, J.; Prochazka, I.; Danis, S.; Vlach, M.; Zaludova, N.; Brauer, G.; Anwand, W.; Mücklich, A.; Gemma, R.; Nikitin, E.; Kirchheim, R.; Pundt, A.
Defect studies of hydrogen loaded Nb: Bulk metals and thin films
Physica Status Solidi (C) ***4****, 3485 (2007).*

18. Donchev, A.; Richter, E.; Schütze, M.; Yankov, R.
Improvement of the oxidation resistance of TiAl-alloys with fluorine
Intermetallics ***14****, 1168 (2007).*

19. Gago, R.; Abendroth, B.; Cerda, J. I.; Jimenez, I.; Möller, W.
Detection of intrinsic stress in cubic boron nitride films by x-ray absorption near-edge structure: Stress relaxation mechanisms by simultaneous ion implantation during growth
Physical Review B ***76****, 174111 (2007).*

20. Grynszpan, R. I.; Anwand, W.; Brauer, G.; Coleman, G.
Positron depth profiling in solid surface layers
Annales de Chimie - Science des Matériaux ***32****, 365 (2007).*

21. Höglund, C.; Beckers, M.; Schell, N.; Borany, J. von; Birch, J.; Hultman, L.
Topotaxial growth of Ti_2AlN by solid state reaction in AlN/Ti(0001)multilayer thin films
Applied Physics Letters ***90****, 174106 (2007).*

22. Jagielski, J.; Piatkowska, A.; Merstallinger, A.; Librant, Z.; Aubert, P.; Grötzschel, R.; Suszko, T.
Friction properties of implanted alumina for vacuum applications
Vacuum ***81****, 1357 (2007).*

23. Krause, M.; Abrasonis, G.; Kolitsch, A.; Mücklich, A.; Kreissig, U.; Möller, W.
Nickel catalysed sixfold ring clustering and graphitisation in C:Ni nanocomposites: A Raman analysis
Physica Status Solidi (B) ***244****, 4236 (2007).*

24. Krause, M.; Ziegs, F.; Popov, A. A.; Dunsch, L.
Entrapped bonded hydrogen in a fullerene - The five atomic cluster Sc_3CH in C_{80}
ChemPhysChem ***8****, 537 (2007).*

25. Lifshitz, Y.; Edrei, R.; Hoffman, A.; Grossman, E.; Lempert, G. D.; Berthold, J.; Schultrich, B.; Jäger, H. U.
Surface roughness evolution and growth mechanism of carbon films from hyperthermal species
Diamond and Related Materials ***16****, 1771 (2007).*

26. Mandumpal, J.; Gemming, S.; Seifert, G.
Curvature effects of nitrogen on graphitic sheets: Structures and energetics
Chemical Physics Letters ***447****, 115 (2007).*

27. Manova, D.; Eichentopf, I.; Heinrich, S.; Mandl, S.; Richter, E.; Neumann, H.; Rauschenbach, B.
Interplay of cold working and nitrogen diffusion in austenitic stainless steel
Nuclear Instruments and Methods in Physics Research B ***257****, 442 (2007).*

28. Manova, D.; Hirsch, D.; Richter, E.; Mandl, S.; Neumann, H.; Rauschenbach, B.
Microstructure of nitrogen implanted stainless steel after wear experiment
Surface and Coatings Technology ***201****, 8329 (2007).*

29. Martins, R. M. S.; Schell, N.; Silva, R. J. C.; Pereira, L.; Mahesh, K. K.; Fernandes, F. M. B.
In-situ study of Ni-Ti thin film growth on a TiN intermediate layer by X-ray diffraction
Sensors and Actuators B ***126****, 332 (2007).*

30. Michel, K. H.; Verberck, B.; Hulman, M.; Kuzmany, H.; Krause, M.
Superposition of quantum and classical rotational motions in $Sc_2C_2@C_{84}$ fullerite
Journal of Chemical Physics ***126****, 64304 (2007).*

31. Niskanen, A.; Kreissig, U.; Leskelä, M.; Ritala, M.
Radical enhanced atomic layer deposition of tantalum oxide
Chemistry of Materials ***19****, 2316 (2007).*

32. Peter, S.; Graupner, K.; Grambole, D.; Richter, F.
A comparative experimental analysis of the a-C:H deposition processes using CH_4 and C_2H_2 as precursors
Journal of Applied Physics ***102****, 53304 (2007).*

33. Piekoszewski, J.; Kempinski, W.; Andrzejewski, B.; Trybula, Z.; Kaszynski, J.; Stankowski, J.; Stanislawski, J.; Barlak, M.; Jagielski, J.; Werner, Z.; Grötzschel, R.; Richter, E.
Formation of superconducting regions of MgB_2 by implantation of magnesium ions into boron substrate followed by intense pulsed plasma treatment
Surface and Coatings Technology ***201****, 8175 (2007).*

34. Piekoszewski, J.; Kempinski, W.; Barlak, M.; Kaszynski, J.; Stanislawski, J.; Anduejewski, B.; Werner, Z.; Plekara-Sady, L.; Richter, E.; Stankowskic, J.; Grötzschel, R.; Lo, S.
Superconducting and electrical properties of Mg-B structures formed by implantation of magnesium ions into the bulk boron followed by pulse plasma treatment
Vacuum ***81****, 1398 (2007).*

35. Ram Mohan Rao, K.; Mukherjee, S.; Roy, S. K.; Richter, E.; Möller, W.; Manna, I.
Plasma immersion ion implantation of nitrogen on austenitic stainless steel at variable energy for enhanced corrosion resistance
Surface and Coatings Technology ***201****, 4919 (2007).*

36. Riviere, J. P.; Templier, C.; Declémy, A.; Redjdal, O.; Chumlyakov, Y.; Abrasonis, G.
Microstructure of expanded austenite in ion-nitrided AISI 316L single crystals
Surface and Coatings Technology ***201****, 8210 (2007).*

37. Rogozin, A.; Vinnichenko, M.; Shevchenko, N.; Vazquez, L.; Mücklich, A.; Kreissig, U.; Yankov, R. A.; Kolitsch, A.; Möller, W.
Effect of elevated substrate temperature on growth, properties, and structure of indium tin oxide films prepared by reactive magnetron sputtering
Journal of Materials Research ***22****, 2319 (2007).*

38. Seppänen, T.; Hultman, L.; Birch, J.; Beckers, M.; Kreissig, U.
Deviations from Vegard's rule in $Al_{1-x}In_xN$ (0001) alloy thin films grown by magnetron sputter epitaxy
Journal of Applied Physics ***101****, 043519 (2007).*

39. Silva, M. M.; Ueda, M.; Pichon, L.; Reuther, H.; Lepienski, C. M.
Surface modification of Ti6Al4V alloy by PIII at high temperatures: Effects of plasma potential
Nuclear Instruments and Methods in Physics Research B **257***, 722 (2007).*

40. Tan, I. H.; Ueda, M.; Oliveira, R. M.; Dallaqua, R. S.; Reuther, H.
Plasma immersion ion implantation in arc and glow discharge plasmas submitted to low magnetic fields
Surface and Coatings Technology ***201****, 4826 (2007).*

41. Tan, I. H.; Ueda, M.; Rossi, J. O.; Diaz, B.; Abramof, E.; Reuther, H.
Nitrogen plasma ion implantation in silicon using short pulse high voltage glow discharges
Journal of Physics D ***40****, 5196 (2007).*

42. Tsyganov, I. A.; Maitz, M. F.; Richter, E.; Reuther, H.; Mashina, A. I.; Rustichelli, F.
Hemocompatibility of titanium-based coatings prepared by metal plasma immersion ion implantation and deposition
Nuclear Instruments and Methods in Physics Research B **257***, 122 (2007).*

43. Ueda, M.; Silva, M. M.; Lepienski, C. M.; Soares, P. C. Jr.; Gonçalves, J. A. N.; Reuther, H.
High-temperature plasma immersion ion implantation
Surface and Coatings Technology ***201****, 4953 (2007).*

44. Vinnichenko, M.; Shevchenko, N.; Rogozin, A.; Grötzschel, R.; Mücklich, A.; Kolitsch, A.; Möller, W.
Structure and dielectric function of two- and single-domain ZnO epitaxial films
Journal of Applied Physics ***102****, 113505 (2007).*

45. Yankov, R. A.; Shevchenko, N.; Rogozin, A.; Maitz, M. F.; Richter, E.; Möller, W.; Donchev, A.; Schütze, M.
Reactive plasma immersion ion implantation for surface passivation
Surface and Coatings Technology ***201****, 6752 (2007).*

Nanoscale Magnetism

46. Gemming, S.; Janisch, R.; Schreiber, M.; Spaldin, N. A.
Density functional investigation of the (113)[-110] twin grain boundary in TiO_2 anatase and its influence on magnetism in diluted magnetic semiconductors
Physical Review B ***76****, 045204 (2007).*

47. Küpper, K.; Bischoff, L.; Akhmadaliev, C.; Fassbender, J.; Stoll, H.; Chou, K. W.; Puzic, A.; Fauth, K.; Dolgos, D.; Schütz, G.; van Waeyenberge, B.; Tyliszczak, T.; Neudecker, I.; Woltersdorf, G.; Back, C. H.
Vortex dynamics in permalloy disks with artificially point defects: Suppression of the gyrotropic mode
Applied Physics Letters ***90****, 062506 (2007).*

48. Küpper, K.; Buess, M.; Raabe, J.; Quitmann, C.; Fassbender, J.
Dynamic vortex − antivortex interaction in a single cross-tie wall
Physical Review Letters ***99****, 167202 (2007).*

49. Liedke, M. O.; Liedke, B.; Keller, A.; Hillebrands, B.; Mücklich, A.; Facsko, S.; Fassbender, J.
Induced anisotropies in exchange coupled systems on rippled substrates
Physical Review B ***75****, 220407 (2007).*

50. Mattern, N.; Zhang, W. X.; Roth, S.; Reuther, H.; Bähtz, C.; Richter, M.
Structural and magnetic properties of non-stoichiometric Fe_2Zr
Journal of Physics: Condensed Matter ***19****, 376202 (2007).*

51. Patra, A. K.; Neu, V.; Fähler, S.; Grötzschel, R.; Bedanta, S.; Kleemann, W.; Schultz, L.
Crystal structure and its correlation to intrinsic and extrinsic magnetic properties of epitaxial hard magnetic Pr-Co films
Physical Review B ***75****, 184417 (2007).*

52. Potzger, K.; Anwand, W.; Reuther, H.; Zhou, S.; Talut, G.; Fassbender, J.; Brauer, G.; Skorupa, W.
The effect of flash lamp annealing on Fe implanted ZnO single crystals
Journal of Applied Physics ***101****, 033906 (2007).*

53. Potzger, K.; Zhou, S.; Reuther, H.; Küpper, K.; Talut, G.; Helm, M.; Fassbender, J.; Denlinger, J. D.
Suppression of secondary phase formation in Fe implanted ZnO single crystals
Applied Physics Letters ***91****, 062107 (2007).*

54. Som, T.; Ghosh, S.; Mäder, M.; Grötzschel, R.; Roy, S.; Paramanik, D.; Gupta, A.
Temperature-dependent changes in structural and magnetic properties of heavy ion irradiated nanoscale Co/Pt multilayers
New Journal of Physics ***9****, 164 (2007).*

55. Talut, G.; Reuther, H.; Stromberg, F.; Zhou, S.; Potzger, K.; Eichhorn, F.
Ferromagnetism in GaN induced by Fe ion implantation
Journal of Applied Physics ***102****, 083909 (2007).*

56. Xu, Q.; Hartmann, L.; Schmidt, H.; Hochmuth, H.; Lorenz, M.; Spemann, D.; Grundmann, M.
s-d exchange interaction induced magnetoresistance in magnetic ZnO
Physical Review B ***76****, 134417 (2007).*

57. Zhou, S.; Potzger, K.; Mücklich, A.; Eichhorn, F.; Schell, N.; Grötzschel, R.; Schmidt, B.; Skorupa, W.; Helm, M.; Fassbender, J.; Geiger, D.
Structural and magnetic properties of Mn-implanted Si
Physical Review B ***75****, 085203 (2007).*

58. Zhou, S.; Potzger, K.; Reuther, H.; Skorupa, W.; Helm, M.; Fassbender, J.
Absence of ferromagnetism in V-implanted ZnO single crystals
Journal of Applied Physics ***101****, 09H109 (2007).*

59. Zhou, S.; Potzger, K.; Reuther, H.; Talut, G.; Eichhorn, F.; Borany, J. von; Skorupa, W.; Helm, M.; Fassbender, J.
Crystallographically oriented magnetic $ZnFe_2O_4$ nanoparticles synthesized by Fe implantation into ZnO
Journal of Physics D ***40****, 964 (2007).*

Nanostructures

60. Beyer, V.; Borany, J. von; Klimenkov, M.
A transient electrical model of charging for Ge nanocrystal containing gate oxides
Journal of Applied Physics ***101****, 094507 (2007).*

61. Bischoff, L.; Akhmadaliev, Ch.; Schmidt, B.
Defect induced nanowire growth by FIB implantation
Microelectronic Engineering ***84****, 1459 (2007).*

62. Brauer, G.; Anwand, W.; Grambole, D.; Skorupa, W.; Hou, Y.; Andreev, A.; Teichert, C.; Tam, K. H.; Djurisic, A. B.
Non-destructive characterization of vertical ZnO nanowire arrays by slow positron implantation spectroscopy, atomic force microscopy, and nuclear reaction analysis
Nanotechnology ***18****, 195301 (2007).*

63. Enyashin, A. N.; Gemming, S.
$TiSi_2$-nanostructures - Enhanced conductivity at nanoscale?
Physica Status Solidi (B) ***244****, 3593 (2007).*

64. Enyashin, A. N.; Gemming, S.; Seifert, G.
DNA-wrapped carbon nanotubes
Nanotechnology ***18****, 245702 (2007).*

65. Enyashin, A. N.; Gemming, S.; Seifert, G.
Nanosized allotropes of molybdenum disulfide
European Physical Journal - Special Topics ***149****, 103 (2007).*

66. Enyashin, Andrey N.; Gemming, S.; Bar-Sadan, M.; Popovits-Biro, R.; Hong, Sung Y.; Prior, Y.; Tenne, R.; Seifert, G.
Structure and stability of molybdenum sulfide fullerenes
Angewandte Chemie ***119****, 631 (2007).*

67. Gemming, S.; Seifert, G.
Nanocrystals: Catalysts on the edge
Nature Nanotechnology ***2****, 21 (2007).*

68. Ghicov, A.; Schmidt, B.; Kunze, J.; Schmuki, P.
Photoresponse in the visible range from Cr doped TiO_2 nanotubes
Chemical Physics Letters ***433****, 323 (2007).*

69. Grenzer, J.; Mücklich, A.; Grigorian, S.; Pietsch, U.; Datta, D.; Chini, T. K.; Hazra, S.; Sanyal, M. K.
High-temperature induced nanocrystal formation in ion-beam-induced amorphous silicon ripples
Physica Status Solidi (A) ***204****, 2555 (2007).*

70. Kim, D. S.; Ji, R.; Fan, H. J.; Bertram, F.; Scholz, R.; Dadgar, A.; Nielsch, K.; Krost, A.; Christen, J.; Gösele, U.; Zacharias, M.
Laser interference lithography tailored for highly symmetric arranged ZnO nanowire arrays
Small ***3****, 76 (2007).*

71. Oates, T. W. H.; Christalle, E.
Real-time spectroscopic ellipsometry of silver nanoparticle formation in poly(vinyl alcohol) thin films
Journal of Physical Chemistry C ***111****, 182 (2007).*

72. Oates, T. W. H., Keller, A., Facsko, S., Mücklich, A.
Aligned silver nanoparticles on rippled silicon templates exhibiting anisotropic plasmon absorption
Plasmonics **2***, 47 (2007).*

73. Peeva, A.; Kalitzova, M.; Beshkov, G.; Zollo, G.; Vitali, G.; Skorupa, W.
Nanocluster evolution in Ge^+ ion implanted Ta_2O_5 layers
Materials Letters ***61****, 3620 (2007).*

74. Popov, I.; Gemming, S.; Seifert, G.
Structural and electronic properties of a Mo_6S_8 cluster deposited on a Au(111) surface
Physical Review B **75***, 245436 (2007).*

75. Popov, I.; Kunze, T.; Gemming, S.; Seifert, G.
Self-assembly of Mo_6S_8 clusters on the Au(111) surface
European Physical Journal D ***45****, 439 (2007).*

76. Popov, Alexey A.; Krause, M.; Yang, S.; Wong, J.; Dunsch, L.
C_{78} cage isomerism defined by trimetallic nitride cluster size: A computational and vibrational spectroscopic study
Journal of Physical Chemistry B ***111****, 3363 (2007).*

77. Radke de Cuba, M. H.; Emmerich, H.; Gemming, S.
Finding polymorphic structures during vicinal surface growth
European Physical Journal - Special Topics ***1****, 43 (2007).*

78. Rangelow, I. W.; Ivanov, T.; Ivanova, K.; Volland, B. E.; Grabiec, P.; Sarov, Y.; Persaud, A.; Gotszalk, T.; Zawierucha, P.; Zielony, M.; Dontzov, D.; Schmidt, B.; Zier, M.; Nikolov, N.; Kostic, I.; Engl, W.; Sulzbach, T.; Mielczarski, J.; Kolb, S.; Latimier, Du P.; Pedreau, R.; Djakov, V.; Huq, S. E.; Edinger, K.; Fortagne, O.; Almansa, A.; Blom, H. O.
Piezoresistive and self-actuated 128-cantilever arrays for nanotechnology applications
Microelectronic Engineering ***84****, 1260 (2007).*

79. Röntzsch, L.; Heinig, K.-H.; Schuller, Jon A.; Brongersma, M. L.
Thin film patterning by surface-plasmon-induced thermocapillarity
Applied Physics Letters ***90****, 044105 (2007).*

80. Salh, R.; Fitting, L.; Kolesnikova, E. V.; Sitnikova, A. A.; Zamoryanskaya, M. V.; Schmidt, B.; Fitting, H.-J.
Si and Ge nanocluster formation in silica matrix
Semiconductors ***41****, 397 (2007).*

81. Schmidt, B.
Nanocluster memories by ion beam synthesis of Si in SiO_2
Materials Science ***25****, 1213 (2007).*

82. Schmidt, B.
Nanostructures by ion beams
Radiation Effects and Defects in Solids ***162****, 171 (2007).*

83. Schmidt, B.; Mücklich, A.; Röntzsch, L.; Heinig, K.-H.
How do high energy heavy ions shape Ge nanoparticles embedded in SiO_2?
Nuclear Instruments and Methods in Physics Research B ***257****, 30 (2007).*

84. Schöndorfer, C.; Lugstein, A.; Bischoff, L.; Hyun, Y. J.; Pongratz, P.; Bertagnolli, E.
FIB induced growth of antimony nanowires
Microelectronic Engineering ***84****, 1440 (2007).*

85. Schöndorfer, Ch.; Lugstein, A.; Hyun, Y.-J.; Bertagnolli, E.; Bischoff, L.; Nellen, P. M.; Callegari, V.; Pongratz, P.
Focused ion beam induced synthesis of a porous antimony nanowire network
Journal of Applied Physics ***102****, 044308 (2007).*

86. Stepina, N. P.; Dvurechenskii, A. V.; Armbrister, V. A.; Kesler, V. G.; Novikov, P. L.; Gutakovskii, A. K.; Kirienko, V. V.; Smagina, Zh. V.; Grötzschel, R.
Pulsed ion-beam induced nucleation and growth of Ge nanocrystals on SiO_2
Applied Physics Letters ***90****, 33120 (2007).*

87. Takahashi, S.; Dawson, P.; Zayats, A. V.; Bischoff, L.; Angelov, O.; Dimova-Malinovska, D.; Tsvetkova, T.; Townsend, P. D.
Optical contrast in ion-implanted amorphous silicon carbide nanostructures
Journal of Physics D ***40****, 7492 (2007).*

Doping and Defects of Semiconductors

88. Beyer, R.; Schmidt, B.
Scanning capacitance microscopy and the role of localized charges in dielectric films: Infering or challenging?
Microelectronic Engineering ***84****, 376 (2007).*

89. Beyer, V.; Borany, J. von; Heinig, K.-H.
Dissociation of Si^+ ion implanted and as-grown thin SiO_2 layers during annealing in ultra-pure neutral ambient by emanation of SiO
Journal of Applied Physics ***101****, 053516 (2007).*

90. Brauer, G.; Anwand, W.; Skorupa, W.; Kuriplach, J.; Melikhova, O.; Cizek, J.; Prochazka, I.; Moisson, C.; Wenckstern, H. von; Schmidt, H.; Lorenz, M.; Grundmann, M.
Comparative characterization of differently grown ZnO single crystals by positron annihilation and Hall effect
Superlattices and Microstructures ***42****, 259 (2007).*

91. Brauer, G.; Anwand, W.; Skorupa, W.; Kuriplach, J.; Melikhova, O.; Cizek, J.; Prochazka, I.; Wenckstern, H. von; Brandt, M.; Lorenz, M.; Grundmann, M.
Defects in N^+ ion-implanted ZnO single crystals studied by positron annihilation and Hall effect
Physica Status Solidi (C) ***4****, 3642 (2007).*

92. Brauer, G.; Kuriplach, J.; Anwand, W.; Becvar, F.; Skorupa, W.
Characterization of various crystalline structures at the SiO_2/Si interface by positrons
Radiation Physics and Chemistry ***76****, 195 (2007).*

93. Brauer, G.; Kuriplach, J.; Cizek, J.; Anwand, W.; Melikhova, O.; Prochazka, I.; Skorupa, W.
Positron lifetimes in ZnO single crystals
Vacuum ***81****, 1314 (2007).*

94. Danesh, P.; Pantchev, B.; Schmidt, B.; Grambole, D.
Molecular hydrogen in amorphous silicon with high internal stress
Japanese Journal of Applied Physics ***46****, 5050 (2007).*

95. Diaz, B.; Abramof, E.; Castro, R. M.; Ueda, M.; Reuther, H.
Strain profile of (001) silicon implanted with nitrogen by plasma immersion
Journal of Applied Physics ***101****, 103523 (2007).*

96. Fitting, H.-J.; Salh, R.; Schmidt, B.
Multimodal electronic-vibronic spectra of luminescence in ion-implanted silica layers
Journal of Luminescence ***122****, 743 (2007).*

97. Fitting, H.-J.; Salh, R.; Schmidt, B.
Multimodal luminescence spectra of ion-implanted silica
Semiconductors ***41****, 453 (2007).*

98. Gao, F.; Du, J.; Bylaska, E. J.; Posselt, M.; Weber, W. J.
Ab-initio atomic simulations of antisite pair recovery in cubic silicon carbide
Applied Physics Letters ***90****, 221915 (2007).*

99. Gao, F.; Zhang, Y.; Devanathan, R.; Posselt, M.; Weber, W. J.
Atomistic simulations of epitaxial recrystallization in 4H-SiC along the [0001] direction
Nuclear Instruments and Methods in Physics Research B ***255****, 136 (2007).*

100. Höhne, R.; Esquinazi, P.; Heera, V.; Weishart, H.
Magnetic properties of ion implanted diamond
Diamond and Related Materials ***16****, 1589 (2007).*

101. Hui, C. W.; Zhang, Z. D.; Taojun, Z.; Ling, C. C.; Beling, C. D.; Fung, S.; Brauer, G.; Anwand, W.; Skorupa, W.
Positron annihilation spectroscopic study of hydrothermal grown n-type zinc oxide single crystal
Physica Status Solidi (C) ***4****, 3672 (2007).*

102. Kögler, R.; Mücklich, A.; Eichhorn, F.; Schell, N.; Skorupa, W.; Christensen, J. S.
Praseodymium compound formation in silicon by ion beam synthesis
Vacuum ***81****, 1318 (2007).*

103. Kögler, R.; Peeva, A.; Mücklich, A.; Kutznetsov, A.; Christensen, J. S.; Svensson, B. G.; Skorupa, W.
Excess vacancies in high energy ion implanted SiGe
Journal of Applied Physics ***101****, 033508 (2007).*

104. Kögler, R.; Mücklich, A.; Vines, L.; Krecar, D.; Kuznetsov, A. Y.; Skorupa, W.
Defect engineering in the initial stage of SIMOX processing
Nuclear Instruments and Methods in Physics Research B ***257****, 161 (2007).*

105. Markwitz, A.; Barry, B.; Eichhorn, F.
X-ray diffraction study of low-energy carbon-ion implanted Si(001)
Surface and Interface Analysis ***39****, 415 (2007).*

106. McMahon, R. A.; Smith, M. P.; Seffen, K. A.; Voelskow, M.; Anwand, W.; Skorupa, W.
Flash-lamp annealing of semiconductor materials - Applications and process models
Vacuum ***81****, 1301 (2007).*

107. Nasdala, L.; Kronz, A.; Grambole, D.; Trullenque, G.
Effects of irradiation damage on the back-scattering of electrons: Silicon-implanted silicon
American Mineralogist ***92****, 1768 (2007).*

108. Nasdala, L.; Grambole, D.
Raman study of irradiation damage in silicon
Mitteilungen der Österreichischen Mineralogischen Gesellschaft ***153****, 85 (2007).*

109. Nazarov, A.; Osiyuk, I.; Sun, J.; Yankov, R.; Skorupa, W.; Tyagulskii, I.; Lysenko, V.; Prucnal, S.; Gebel, T.; Rebohle, L.
Quenching of electroluminescence and charge trapping in high-efficiency Ge-implanted MOS light-emitting silicon diodes
Applied Physics B ***87****, 129 (2007).*

110. Peeva, A.; Dikovska, A. Og.; Atanasov, P. A.; Jimenez de Castro, M.; Skorupa, W.
Rare-earth implanted Y_2O_3 thin films
Applied Surface Science ***253****, 8165 (2007).*

111. Pezoldt, J.; Kups, Th.; Voelskow, M.; Skorupa, W.
Ion beam synthesis of 4H-($Si_{1-x}C_{1-y}$)Ge_{x+y} solid solutions
Physica Status Solidi (A) ***204****, 998 (2007).*

112. Popov, V. P.; Tyschenko, I. E.; Cherkov, A. G.; Pokhil, G. P.; Fridman, V. M.; Voelskow, M.
Advanced heterostructure Si-InSb on insulator formed by bonding of hydrogen transferred Si layer and implanted SiO_2 film
ECS Transactions ***6****, 345 (2007).*

113. Popov, V. P.; Tyschenko, I. E.; Cherkov, A. G.; Pokhil, G. P.; Fridman, V. M.; Voelskow, M.
Nanoscaled silicon-based heterostructures formed by interface mediated endotaxy
ECS Transactions ***6****, 87 (2007).*

114. Prucnal, S.; Sun, J.; Nazarov, A.; Tjagulskii, I.; Osiyuk, I.; Fedaruk, R.; Skorupa, W.
Correlation between defect-related electroluminescence and charge trapping in Gd-implanted SiO_2 layers
Applied Physics B ***88****, 241 (2007).*

115. Prucnal, S.; Sun, J.; Reuther, H.; Skorupa, W.; Buchal, C.
Electronegativity and point defect formation in ion implanted SiO_2 layers
Vacuum ***81****, 1296 (2007).*

116. Salh, R.; Fitting Kourkoutis, L.; Schmidt, B.; Fitting, H.-J.
Luminescence of isoelectronically ion-implanted SiO_2 layers
Physica Status Solidi (A) ***204****, 3132 (2007).*

117. Salh, R.; Fitting-Kourkoutis, L.; Schmidt, B.; Fitting, H.-J.
Cathodoluminescence of ion-implanted silica layers
Microscopy and Microanalysis ***13****, 328 (2007).*

118. Satta, A.; D'Amore, A.; Simoen, E.; Anwand, W.; Skorupa, W.; Clarysse, T.; van Daele, B.; Janssens, T.
Formation of germanium shallow junction by flash annealing
Nuclear Instruments and Methods in Physics Research B ***257****, 157 (2007).*

119. Schmidt, H.; Wiebe, M.; Dittes, B.; Grundmann, M.
Meyer-Neldel rule in ZnO
Applied Physics Letters ***91****, 232110 (2007).*

120. Tyschenko, I. E.; Cherkov, A. G.; Voelskow, M.; Popov, V. P.
Crystallization of InSb phase near the bonding interface of silicon-on-insulator structure
Solid State Phenomena ***131-133****, 137 (2007).*

121. Tyschenko, I. E.; Talochkin, A. B.; Bagaev, E. M.; Cherkov, A. G.; Popov, V. P.; Misiuk, A.; Yankov, R. A.
Formation of a resonant microcavity in hydrogen ion-implanted silicon-on-insulator structures
Journal of Applied Physics ***102****, 074312 (2007).*

122. Tyschenko, I. E.; Voelskow, M.; Cherkov, A. G.; Popov, V. P.
Behavior of germanium ion-implanted into SiO_2 near the bonding interface of a silicon-on-insulator structure
Semiconductors ***41****, 291 (2007).*

123. Vines, L.; Kögler, R.; Kuznetsov, A. Y.
Scanning spreading resistance microscopy of defect engineered low dose SIMOX samples
Microelectronic Engineering ***84****, 547 (2007).*

124. Wenckstern, H. von; Pickenhain, R.; Schmidt, H.; Brandt, M.; Biehne, G.; Lorenz, M.; Grundmann, M.; Brauer, G.
Investigation of acceptor states in ZnO by junction DLTS
Superlattices and Microstructures ***42****, 14 (2007).*

125. Zolnai, Z.; Ster, A.; Khanh, N. Q.; Battistig, G.; Lohner, T.; Gyulai, J.; Kotai, E.; Posselt, M.
Damage accumulation in nitrogen implanted 6H SiC: Dependence on the direction of ion incidence and on the ion fluence
Journal of Applied Physics ***101****, 023502 (2007).*

Optoelectronics

126. Ben Simon, A.; Paltiel, Y.; Jung, G.; Berger, V.; Schneider, H.
Measurements of non-Gaussian noise in quantum wells
Physical Review B ***76****, 235308 (2007).*

127. Grange, T.; Zibik, E. A.; Ferreira, R.; Bastard, G.; Phillips, P. J.; Stehr, D.; Winnerl, S.; Helm, M.; Steer, M. J.; Hopkinson, M.; Cockburn, J. W.; Skolnick, M. S.; Wilson, L. R.
Singlet and triplet polaron relaxation in doubly charged self-assembled quantum dots
New Journal of Physics ***9****, 259 (2007).*

128. Peter, F.; Winnerl, S.; Nitsche, S.; Dreyhaupt, A.; Schneider, H.; Helm, M.
Coherent terahertz detection with a large-area photoconductive antenna
Applied Physics Letters ***91****, 081109 (2007).*

129. Prucnal, S.; Sun, J. M.; Mücklich, A.; Skorupa, W.
Flash lamp annealing vs rapid thermal and furnace annealing for optimized metal-oxide-silicon-based light-emitting diodes
Electrochemical and Solid State Letters ***10****, H50 (2007).*

130. Prucnal, S.; Sun, J. M.; Rebohle, L.; Skorupa, W.
Fourfold increase of the ultraviolet (314 nm) electroluminescence from SiO_2:Gd layers by fluorine co-implantation and flash lamp annealing
Applied Physics Letters ***91****, 181107 (2007).*

131. Prucnal, S.; Sun, J. M.; Reuther, H.; Skorupa, W.; Buchal, Ch.
Strong improvement of the electroluminescence stability of SiO_2:Gd layers by potassium co-implantation.
Electrochemical and Solid State Letters ***10****, 330 (2007).*

132. Prucnal, S.; Sun, J. M.; Skorupa, W.; Helm, M.
Switchable two-color electroluminescence based on a Si metal-oxide-semiconductor structure doped with Eu
Applied Physics Letters ***90****, 181121 (2007).*

133. Schneider, H.; Drachenko, O.; Winnerl, S.; Helm, M.; Maier, T.; Walther, M.
Autocorrelation measurements of free-electron laser radiation using a two-photon QWIP
Infrared Physics and Technology ***50****, 95 (2007).*

134. Schneider, H.; Maier, T.; Walther, M.; Liu, H. C.
Two-photon photocurrent spectroscopy of electron intersubband relaxation and dephasing in quantum wells
Applied Physics Letters ***91****, 191116 (2007).*

135. Schneider, S.; Seidel, J.; Grafström, S.; Eng, L. M.; Winnerl, S.; Stehr, D.; Helm, M.
Impact of optical in-plane anisotropy on near-field phonon polariton spectroscopy
Applied Physics Letters ***90****, 143101 (2007).*

136. Stehr, D.; Helm, M.; Metzner, C.; Wanke, M. C.
Theory of impurity states in coupled quantum wells and superlattices and their infrared absorption spectra
AIP Conference Proceedings ***893****, 243 (2007).*

137. Stehr, D.; Winnerl, S.; Helm, M.; Andrews, A. M.; Roch, T.; Strasser, G.
Relaxation dynamics of interminiband transitions and electron cooling in doped GaAs/AlGaAs superlattices
AIP Conference Proceedings ***893****, 485 (2007).*

138. Villas-Boas Grimm, C.; Priegnitz, M.; Winnerl, S.; Schneider, H.; Helm, M.
Intersubband relaxation dynamics in single and double quantum wells based on strained

InGaAs/AlAs/AlAsSb
Applied Physics Letters ***91****, 191121 (2007).*

Others

139. Bischoff, L.; Pilz, W.; Ganetsos, Th.; Forbes, R.; Akhmadaliev, C.
GaBi liquid metal alloy ion source for the production of ions of interest in microelectronics research
Ultramicroscopy ***107****, 865 (2007).*

140. Bürger, W.; Lange, H.; Petr, V.
A new method of improving the acceleration voltage stability of Van de Graaff accelerators
Nuclear Instruments and Methods in Physics Research A ***586****, 160 (2007).*

141. Chen, X. D.; Ling, C. C.; Djurisic, A. B.; Brauer, G.; Anwand, W.; Skorupa, W.; Reuther, H.
Influence of hydrogen peroxide treatment on Au/n-ZnO contact
Physica Status Solidi (C) ***4****, 3633 (2007).*

142. Cieslak, J.; Dubiel, S. M.; Eichhorn, F.; Menzel, M.; Reuther, H.
Investigation of single-crystals of chromium implanted with ^{119}Sn-ions of various energies
Journal of Alloys and Compounds ***442****, 235 (2007).*

143. Cizek, J.; Prochazka, I.; Danis, S.; Cieslar, M.; Brauer, G.; Anwand, W.; Kirchheim, R.; Pundt, A.
Hydrogen-induced defects in niobium
Journal of Alloys and Compounds ***446****, 479 (2007).*

144. Ganetsos, Th.; Mair, A. W. R.; Bischoff, L.; Akhmadaliev, C.; Aidinis, C. J.
Can direct field-evaporation of doubly-charged ions and post-ionisation from singly-charged state co-exist?
Surface and Interface Analysis ***39****, 128 (2007).*

145. Gemming, S.; Luschtinetz, R.; Chaplygin, I.; Seifert, G.; Loppacher, C.; Eng, Lukas M.; Kunze, T.; Olbrich, C.
Polymorphism in ferroic functional elements - Bridging length and time scales
European Physical Journal - Special Topics ***149****, 145 (2007).*

146. Gemming, S.; Popov, I.; Lehmann, M.
Polymorphism in liquid crystals from star-shaped mesogens
Philosophical Magazine Letters ***87****, 883 (2007).*

147. Grynszpan, R. I.; Saude, S.; Mazerolles, L.; Anwand, W.; Brauer, G.
Positron depth profiling in ion-implanted zirconia stabilized with trivalent cations
Radiation Physics and Chemistry ***76****, 333 (2007).*

148. Gu, Q. L.; Ling, C. C.; Chen, X. D.; Cheng, C. K.; Ng, A. M. C.; Beling, C. D.; Fung, S.; Djurišić, A. B.; Brauer, G.; Ong, H. C.
Hydrogen peroxide treatment induced rectifying behavior of Au/n-ZnO contact
Applied Physics Letters ***90****, 122101 (2007).*

149. Kubarev, O. L.; Komlev, V. S.; Maitz, M. F.; Barinov, S. M.
Bioactive composite ceramics in the hydroxyapatite-tricalcium phosphate system
Doklady Chemistry ***413****, 72 (2007).*

150. Kuriplach, J.; Melikhova, O.; Brauer, G.
Basic positron properties of oxides: A computational study
Radiation Physics and Chemistry ***76****, 101 (2007).*

151. Melikhova, O.; Kuriplach, J.; Cizek, J.; Prochazka, I.; Anwand, W.; Brauer, G.; Konstantinova, T. E.; Danilenko, I. A.
Positron annihilation in three zirconia polymorphs
Physica Status Solidi (C) ***4****, 3831 (2007).*

152. Röhnert, D.; Phillipp, F.; Reuther, H.; Weber, T.; Wessel, E.; Schütze, M.
Initial stages in the metal-dusting process on alloy 800
Oxidation of Metals ***68****, 271 (2007).*

153. Salavcova, L.; Spirkova, J.; Ondracek, F.; Mackova, A.; Vacik, J.; Kreissig, U.; Eichhorn, F.; Grötzschel, R.
Study of anomalous behaviour of $LiTaO_3$ during the annealed proton exchange process of optical waveguide's formation - Comparison with $LiNbO_3$
Optical Materials ***29****, 913 (2007).*

154. Walther, K.; Frischbutter, A.; Scheffzük, C.; Kenkmann, T.; Eichhorn, F.
Diffraction measurements with synchrotron radiation on superimposed deformed composite of quartzite

and dunite
Zeitschrift für Geologische Wissenschaften ***35****, 17 (2007).*

155. Wang, T. S.; Grambole, D.; Herrmann, F.; Peng, H. B.; Wang, S. W.
Hydrogen 3D-distribution and the kinetics in a Ti/H system studied by micro-ERDA, NRA and XRD
Surface and Interface Analysis ***39****, 52 (2007).*

156. Zeimer, U.; Grenzer, J.; Korn, D.; Döring, S.; Zorn, M.; Pittroff, W.; Pietsch, U.; Saas, F.; Weyers, M.
X-ray diffraction spot mapping – A tool to study structural properties of semiconductor disk laser devices
Physica Status Solidi (A) ***204****, 2753 (2007).*

157. Zen, A.; Pingel, P.; Neher, D.; Grenzer, J.; Zhuang, W.; Rabe, J. P.; Bilge, A.; Galbrecht, F.; Nehls, B.; Farrell, T.; Scherf, U.; Abellons, R. D.; Grozema, F. C.; Siebbeles, L. D. A.
Organic field-effect transistors utilising oligothiophene based swivel cruciform
Chemistry of Materials ***19****, 1267 (2007).*

Invited Conference Talks

1. Abrasonis, G.
Fullerene-like alloyed carbon films
15th International Summer School on Vacuum, Electron and Ion Technologies (VEIT-2007), 17.-21.09.2007, Sozopol, Bulgaria

2. Bischoff, L.
Ion beam synthesis of nanoclusters and nanowires
Symposium on Vacuum based Science and Technology, 05.-07.09.2007, Greifswald, Germany

3. Bischoff, L.
Application of mass-separated focused ion beams in nano-technology
18th International Conference on Ion Beam Analysis, 23.-28.09.2007, Hyderabad, India

4. Bischoff, L.
FIB Anwendungen mit Legierungs-Flüssigmetall-Ionenquellen
Crossbeam Workshop, 24.-25.10.2007, Halle/Saale, Germany

5. Bischoff, L.
Nanostrukturen
VDE YoungNet Convention 2007, 15.10.2007, Dresden, Germany

6. Brauer, G.
Characterization of ZnO by positron annihilation
37th Polish Seminar on Positron Annihilation, 03.-07.09.2007, Ladek Zdroj, Poland

7. Cizek, J.; Prochazka, I.; Brauer, G.; Anwand, W.; Gemma, R.; Nikitin, E.; Kirchheim, R.; Pundt, A.
Hydrogen interaction with vacancies in electron irradiated niobium
37th Polish Seminar on Positron Annihilation, 03.-07.09.2007, Ladek Zdroj, Poland

8. Fassbender, J.
Ion beam induced magnetic property modifications
Workshop on "Ion beam Processing and Magnetic Properties of Semiconductors", 13.02.2007, Leuven, Belgium

9. Fassbender, J.
Ionenmodifizierte Oberflächen für die Magnetsensorik
Workshop "Funktionalisierte Oberflächen", 22.11.2007, Augsburg, Germany

10. Gago, R.; Jiménez, I.; Vinnichenko, M.; Jäger, H. U.; Belov, A. Yu.
Bonding network in filtered-arc-deposited carbon films: Simulation and characterization
International Conference on Metallurgical Coatings and Thin Films (ICMCTF 2007), 23.-27.04.2007, San Diego, California, USA

11. Gemming, S.
Modelling ferroic functional elements
SFB 484 - Kooperative Phänomene im Festkörper, 16.10.2007, Augsburg, Germany

12. Gemming, S.; Seifert, G.; Enyashin, A.; Popov, I.; Tamuliene, J.
From clusters to wires - DFT investigations of molybdenum sulfide nanostructures
iNANO-Seminar, 08.08.2007, Aarhus, Denmark

13. Heinig, K.-H.
Driving forces of surface patterning and nanocluster tailoring with ion and laser beams
2007 MRS Fall Meeting, Symposium on Nanoscale Pattern Formation, 26.-29.11.2007, Boston, United States

14. Helm, M.
THz sources: From the large to the small
4th meeting of GDR-E THz: Semiconductor Sources and Detectors for THz Radiation, 01.-02.06.2007, Bombannes, France

15. Krause-Rehberg, R.; Brauer, G.; Jungmann, M.; Krille, A.; Rogov, A.; Noack, K.
Progress of the intense positron beam project EPOS
11th International Workshop on Slow Positron Beam Techniques for Solids and Surfaces (SLOPOS-11), 09.-13.07.2007, Orleans, France

16. Krause-Rehberg, R.; Brauer, G.; Jungmann, M.; Krille, A.; Rogov, A.; Noack, K.
Progress of the intense positron beam project EPOS
37th Polish Seminar on Positron Annihilation, 03.-07.09.2007, Ladek Zdroj, Poland

17. Ling, C. C.; Cheung, C. K.; Gu, Q. L.; Dai, X. M.; Xu, S. J.; Zhu, C. Y.; Luo, J. M.; Tam, K. H.; Djurisic, A. B.; Beling, C. D.; Fung, S.; Lu, L. W.; Brauer, G.; Anwand, W.; Skorupa, W.; Ong, H. C.
Defect study in ZnO related structures - a multi-spectroscopic approach
11th International Workshop on Slow Positron Beam Techniques for Solids and Surfaces (SLOPOS-11), 09.-13.07.2007, Orleans, France

18. Möller, W.
Target poisoning during reactive magnetron sputtering
15th International Summer School on Vacuum, Electron, and Ion Technologies (VEIT 2007), 19.09.2007, Sozopol, Bulgaria

19. Möller, W.
Plasma-target interaction in reactive magnetron sputtering
Master Class: Physics and Technology of Plasma-Enhanced CVD Methods, 06.-13.10.2007, Bad Honnef, Germany

20. Potzger, K.; Zhou, S.; Reuther, H.; Helm, M.; Brauer, W.; Fassbender, J.; Arenholz, E.; Denlinger, J. D.; Zeitz, W.-D.; Imielski, P.
Transition metal doping of semiconductors by ion beams - Diluted vs. granular magnetism
Eastmag 2007, 23.-26.08.2007, Kazan, Russia

21. Quitmann, C.; Raabe, J.; Buess, M.; Back, C.; Perzelmaier, K.; Küpper, K.; Fassbender, J.
The dance of the domains: Excitations in magnetic microstructures
6th International Symposium on Atomic Level Characterizations for New Materials and Devices 2007 (ALC'07), 28.10.-02.11.2007, Kanazawa, Japan

22. Rebohle, L.; Prucnal, S.; Sun, J. M.; Helm, M.; Skorupa, W.
Switchable multi-color light emitter based on Eu implanted SiO_2 layers confined in a MOS structure
Silicon to Light & Light to Silicon - Materials, Characterisation and Applications, 09.-10.07.2007, Halle, Germany

23. Satta, A.; Simoen, E.; van Daele, B.; Clarysse, T.; Nicholas, G.; Vandervorst, W.; Anwand, W.; Skorupa, W.; Peaker, T.; Markevich, V.
Junction formation in Ge by ion implantation
International Workshop on INSIGHT in Semiconductor Device Fabrication, Metrology and Modeling (INSIGHT-2007), 06.-09.05.2007, Napa, USA

24. Schmidt, B.
Fabrication of nanostructures by FIB: Cobalt disilicide nanowires in silicon
Ion Beam Nanofabrication, NANO 2007 AAMU/Huntsville Nanotechnology Meeting, 21.-22.05.2007, Huntsville, Alabama, USA

25. Schneider, H.
High performance thermal imaging using quantum well infrared photodetector arrays
March Meeting of the American Physical Society, 05.-09.03.2007, Denver, CO, USA

26. Schneider, H.; Drachenko, O.; Winnerl, S.; Helm, M.; Walther, M.
Autocorrelation measurements of the FELBE free-electron laser and photocurrent saturation study in two-photon QWIPs
SPIE Photonics West, 11th Conference on Ultrafast Phenomena in Semiconductors and Nanostructure Materials, 20.-25.01.2007, San Jose, CA, USA

27. Skorupa, W.
Silicon-based MOS light emitters using rare earth implantation
Silicon to Light & Light to Silicon - Materials, Characterisation and Applications, 09.-10.07.2007, Halle, Germany

28. Skorupa, W.; Anwand, W.; Posselt, M.; Prucnal, S.; Rebohle, L.; Voelskow, M.; Zhou, S.; McMahon, R. A.; Smith, M.; Gebel, T.; Hentsch, W.; Fendler, R.; Lüthge, T.; Satta, A.; Moe Børseth, T.; Kuznetsov, A. Yu.; Svensson, B. G.
Millisecond processing beyond chip technology: From electronics to photonics
15th IEEE International Conference on Advanced Thermal Processing of Semiconductors (IEEE RTP 2007), 02.-07.10.2007, Catania, Italy

29. Sort, J.; Menendez, E.; Liedke, M. O.; Strache, T.; Fassbender, J.; Gemming, T.; Weber, A.; Heyderman, Laura J.; Surinach, S.; Concustell, A.; Rao, K. V.; Deevi, S. C.; Baro, Maria D.; Nogues, J.
Micro- and nanoscale magnetic patterning of paramagnetic FeAl alloys by means of nanoindentation or selective ion irradiation
1st Workshop on Nanolithography and Their Applications, 23.-26.10.2007, Zaragoza, Spain

Conference Contributions

1. Abrasonis, G.; Mücklich, A.; Küpper, K.; Krause, M.; Kreissig, U.; Kolitsch, A.; Möller, W.; Sedlackova, K.; Radnoczi, G.; Torres, R.; Jimenez, I.; Gago, R.
Morphology and bonding structure of fullerene-like nanocomposite C:Ni (~30 at%.) thin films grown by ion beam sputtering
XXIst International Winterschool on Electronic Properties of Novel Materials 2007, 10.-17.03.2007, Kirchberg, Austria

2. Akhmadaliev, S.; Bischoff, L.
High intensity capillary gas ion source for accelerator applications
9th European Conference on Accelerators in Applied Research and Technology (ECAART-9), 03.-07.09.2007, Florence, Italy

3. Anwand, W.; Skorupa, W.; Schumann, Th.; Posselt, M.; Schmidt, B.; Grötzschel, R.; Brauer, G.
Defect profiles in B or P implanted Ge after flash lamp annealing probed by slow positron implantation spectroscopy
3rd CADRES Ge Workshop, 23.01.2007, Gent, Belgium

4. Anwand, W.; Skorupa, W.; Schumann, Th.; Posselt, M.; Schmidt, B.; Grötzschel, R.; Brauer, G.
Defect profiles in B or P implanted Ge after flash lamp annealing probed by slow positron implantation spectroscopy
11th International Workshop on Slow Positron Beam Techniques for Solids and Surfaces (SLOPOS-11), 09.-13.07.2007, Orleans, France

5. Anwand, W.; Skorupa, W.; Schumann, Th.; Posselt, M.; Schmidt, B.; Grötzschel, R.; Brauer, G.
Implantation-caused open volume defects in Ge after flash lamp annealing (FLA) probed by slow positron implantation spectroscopy (SPIS)
11th Workshop on Positron Beam Techniques for Solids and Surfaces, 09.-13.07.2007, Orleans, France

6. Anwand, W.; Xiong, S. Z.; Wu, C. Y.; Gebel, Th.; Schumann, Th.; Brauer, G.; Skorupa, W.
Structural changes in flash lamp annealed amorphous Si layers probed by slow positron implantation spectroscopy
37th Polish Seminar on Positron Annihilation, 03.-07.09.2007, Ladek Zdroj, Poland

7. Baumgart, C.; Abendroth, B.; Abrasonis, G.; Kolitsch, A.; Möller, W.
Growth and optical characterization of dielectric/metal nanocomposites
15th International Summer School on Vacuum, Electron and Ion Technologies (VEIT-2007), 17.-21.09.2007, Sozopol, Bulgaria

8. Benayoun, S.; Grynszpan, R. I.; Hantzpergue, J. J.; Anwand, W.; Eichhorn, F.; Brauer, G.
Phase transition and internal stresses in tungsten coatings
11th International Workshop on Slow Positron Beam Techniques for Solids and Surfaces (SLOPOS-11), 09.-13.07.2007, Orleans, France

9. Beyer, V.; Heinig, K.-H.; Schmidt, B.; Stegemann, K.-H.; Dimitrakis, P.
Memory and luminescence properties of Si nanocrystals fabricated by ion beam mixing
3rd International Workshop on Semiconductor Nanostructures (SEMINANO'07), 13.-16.06.2007, Bad Honnef, Germany

10. Biermann, K.; Kuenzel, H.; Tribuzy, C. V.-B.; Ohser, S.; Schneider, H.; Helm, M.
Impact of interface formation on intersubband transtitions in MBE GaInAs:Si/AlAsSb multiple coupled DQWs
19th International Conference on Indium Phosphide and Related Materials (IPRM'07), 14.-18.05.2007, Matsue, Japan

11. Biermanns, A.; Grenzer, J.; Facsko, S.; Grigorian, S.; Pietsch, U.
Ion-induced surface ripples in silicon
DPG Jahrestagung und DPG Frühjahrstagung des Arbeitskreises Festkörperphysik, 26.-30.03.2007, Regensburg, Germany

12. Biermanns, A.; Grigorian, S.; Pietsch, U.; Hanisch, A.; Facsko, S.; Grenzer, J.
X-ray study of ion-beam induced amorphous-crystalline ripples in silicon
Workshop on Nanopatterning via Ions, Photon Beam and Epitaxy, 23.-27.09.2007, Sestri Levante, Italy

13. Bischoff, L.; Heera, V.
Graphite nanostructures in diamond produced by focused ion beam
E-MRS Spring Meeting, Symposium L, 28.05.-01.06.2007, Strasbourg, France

14. Bischoff, L.; Schmidt, B.; Akhmadaliev, Ch.
Ion beam synthesis and patterning by FIB
RUBion Workshop "Ionenstrahlen und Nanotechnologie", 10.-11.05.2007, Bochum, Germany

15. Borany, J. von; Cantelli, V.; Christalle, E.; Mücklich, A.; Talut, G.; Grenzer, J.
Fabrication of self-assembled $L1_0$ ordered FePt nanoislands by conventional DC magnetron sputtering
E-MRS Spring Meeting (E-MRS 2007), Session K: Nanoscale Self-Assembly and Patterning, 28.05.-01.06.2007, Strasbourg, France

16. Borany, J. von; Gerbeth, G.; Rogozin, A.; Shevchenko, N.; Schmidt, B.
Photovoltaics related research activities at the Forschungszentrum Dresden-Rossendorf
WE-Heraeus-Seminar on Photon Management in Solar Cells, 28.10.-01.11.2007, Bad Honnef, Germany

17. Brauer, G.; Schmidt, M.; Wenckstern, H. von; Anwand, W.; Skorupa, W.; Helm, M.; Grundmann, M.
Geplante PLEPS-Messungen an ZnO-Dünnfilmen
2nd User Meeting at NEPOMUC, 30.10.2007, Garching, Germany

18. Cantelli, V.; Borany, J. von; Grenzer, J.
Self-assembly FePt nanoislands: Surface studies and magnetic properties
7th Autumn School on X-ray Scattering from Surfaces and Thin Layers, 04.-06.10.2007, Smolenice, Slovakia

19. Cantelli, V.; Borany, J. von; Grenzer, J.
Fabrication of self-assembled $L1_0$ ordered FePt nanoislands by conventional DC magnetron sputtering
International Conference on Nanoscale Magnetism - ICNM-2007, 25.-29.06.2007, Istanbul, Turkey

20. Cizek, J.; Prochazka, I.; Vlach, M.; Zaludova, N.; Danis, S.; Dobron, P.; Chmelik, F.; Brauer, G.; Anwand, W.; Mücklich, A.; Nikitin, E.; Gemma, R.; Kirchheim, R.; Pundt, A.
Hydrogen-induced buckling of Pd films studied by positron annihilation
11th International Workshop on Slow Positron Beam Techniques for Solids and Surfaces (SLOPOS-11), 09.-13.07.2007, Orleans, France

21. Cizek, J.; Prochazka, I.; Vlach, M.; Zaludova, N.; Danis, S.; Brauer, G.; Anwand, W.; Mücklich, A.; Gemma, R.; Kirchheim, R.; Pundt, A.
Defect studies of hydrogen-loaded nanocrystalline Gd films
11th International Workshop on Slow Positron Beam Techniques for Solids and Surfaces (SLOPOS-11), 09.-13.07.2007, Orleans, France

22. Dai, X. M.; Gu, Q. L.; Ling, C. C.; Xu, S. J.; Brauer, G.; Anwand, W.; Skorupa, W.
New red luminescence defects in nitrogen-implanted ZnO crystals
4th International Conference on Materials for Advanced Technologies (ICMAT 2007), 01.-06.07.2007, Singapore, Singapore

23. Donchev, A.; Kolitsch, A.; Schütze, M.; Yankov, R.
Fluorine surface treatment of TiAl alloys for aerospace applications
European Congress on Advanced Materials and Processes (EUROMAT-2007), 10.-13.09.2007, Nürnberg, Germany

24. Enyashin, A. N.; Gemming, S.; Seifert, G.
Theory of DNA-wrapped Carbon Nanotubes
E-MRS 2007 Spring Meeting, 27.05.-01.06.2007, Strasbourg, France

25. Fassbender, J.
Ionenstrahlmodifikationen magnetischer Schichten
Workshop "Ionenstrahlphysik und Nanotechnologie", 10.-11.05.2007, Bochum, Germany

26. Frank, A.; Zöllner, J.-P.; Sarov, Y.; Ivanov, Tz.; Rangelow, I. W.; Swiatkowski, M.; Gotszalk, T.; Nikolov, N.; Zier, M.; Schmidt, B.
SPICE simulations of self-actuated piezoresistive cantilever arrays
33rd International Conference on Micro- and Nano-Engineering (MNE07), 23.-26.09.2007, Copenhagen, Denmark

27. Ganetsos, Th.; Bischoff, L.; Pilz, W.; Akhmadaliev, Ch.; Kotsos, B.; Laskaris, N.
Energy distribution measurements with a BiGa liquid metal alloy ion source
XXIII IUPAP International Conference on Statistical Physics, 09.-13.07.2007, Genova, Italy

28. Geissler, A.; Merroun, M.; Geipel, G.; Reuther, H.; Selenska-Pobell, S.
Bacterial responses to uranyl and sodium nitrate treatments and fate of the added U(VI) in uranium mining waste piles
9th Symposium on Bacterial Genetics and Ecology (BAGECO-9), 23.-27.06.2007, Wernigerode, Germany

29. Gemming, S.; Emmerich, H.; Radke de Cuba, M. H.; Kundin, J.
A hybrid method for the structural evolution of stepped surfaces
EUROMAT 2007, 10.-14.09.2007, Nürnberg, Germany

30. Geßner, H.; Posselt, M.
Equilibrium concentration and diffusivity of vacancies and self-diffusion in Ge: An atomistic study
CADRES Ge Workshop, 23.01.2007, Ghent, Belgium

31. Grenzer, J.; Mücklich, A.; Grigorian, S.; Biermanns, A.; Chini, T. K.; Sanyal, M. K.; Pietsch, U.
Ripple structures at top surfaces and underlying crystalline layers induced by ion beam erosion in silicon
12th International Conference on Defects-Recognition, Imaging and Physics in Semiconductors (DRIP), 09.-13.09.2007, Berlin, Germany

32. Grimm, C. V.-B.; Ohser, S.; Winnerl, S.; Grenzer, J.; Schneider, H.; Helm, M.; Neuhaus, J.; Dekorsy, T.; Biermann, K.; Künzel, H.
Intersubband relaxation dynamics in short-wavelength InGaAs/AlAsSb quantum well structures
PHOTONICS WEST 2007, Symposium on Physics and Simulation of Optoelectronic Devices XV, 20.-25.01.2007, San José, CA, USA

33. Gu, Q. L.; Ling, C. C.; Brauer, G.; Anwand, W.; Skorupa, W.
Electrical characterization of deep levels in N^+-implanted ZnO single crystal
4th International Conference on Materials for Advanced Technologies (ICMAT 2007), 01.-06.07.2007, Singapore, Singapore

34. Heinig, K.-H.
Exotisches Verhalten von Grenzflächen unter Ionenbestrahlung
Workshop „Ionenstrahlphysik und Nanotechnologie“, 10.-11.05.2007, Bochum, Germany

35. Heinig, K.-H.; Röntzsch, L.
Driving forces of ion-beam-induced nanopatterning
Workshop on Nanopatterning via Ions, Photon Beam and Epitaxy, 23.-27.09.2007, Sestri Levante, Italy

36. Heinig, K.-H.; Röntzsch, L.; Schuller, J. A.; Brongersma, M. L.
Thin film patterning by surface-plasmon-induced thermocapillarity
Workshop on Nanopatterning via Ions, Photon Beam and Epitaxy, 23.-27.09.2007, Sestri Levante, Italy

37. Hanisch, A.; Grenzer, J.; Facsko, S.; Biermanns, A.; Pietsch, U.; Metzger, T. H.; Carbone, G.
Ion-induced ripple structures on silicon, X-ray measurements and TEM
7th Autumn School on X-ray scattering from Surfaces and Thin Layers, 04.-06.10.2007, Smolenice, Slovakia

38. Hofmann, M.; Kambor, S.; Schmidt, C.; Grambole, D.; Rentsch, J.; Glunz, S.; Preu, R.
Firing stable surface passivation using all-PECVD stacks of SiO_x:H and SiN_x:H
22nd European Photovoltaic Solar Energy Conference and Exhibition, 03.-07.09.2007, Milano, Italy

39. Hofmann, M.; Schmidt, C.; Kohn, N.; Grambole, D.; Rentsch, J.; Glunz, S.; Preu, R.
Detailed analysis of amorphous silicon passivation layers deposited in industrial in-line and laboratory-type PECVD reactors
22nd European Photovoltaic Solar Energy Conference and Exhibition, 03.-07.09.2007, Milano, Italy

40. Hou, Y.; Andreev, A.; Teichert, C.; Brauer, G.; Djurisic, A.
Characterization of ZnO nanorods by AFM
Materials Today Asia, 03.-05.09.2007, Beijing, China

41. Hou, Y.; Andreev, A.; Teichert, C.; Brauer, G.; Djurisic, A.
Characterization of ZnO nanorods by AFM
E-MRS 2007 Spring Meeting, SYMPOSIUM M, 28.05.-01.06.2007, Strasbourg, France

42. Jungmann, M.; Krause-Rehberg, R.; Brauer, G.
Construction and timing system of the EPOS beam system
11th International Workshop on Slow Positron Beam Techniques for Solids and Surfaces (SLOPOS-11), 09.-13.07.2007, Orleans, France

43. Keller, A.; Facsko, S.; Möller, W.
Evolution of ion induced ripple patterns on silicon surfaces
Workshop on Nanopatterning via Ions, Photon Beam and Epitaxy, 23.-27.09.2007, Sestri Levante, Italy

44. Keller, A.; Rossbach, S.; Facsko, S.; Möller, W.
Simultaneous formation of two ripple modes on ion sputtered silicon
International Workshop on SEMIconductor NANOstructures 2007, 13.-16.06.2007, Bad Honnef, Germany

45. Kögler, R.; Mücklich, A.; Anwand, W.; Eichhorn, F.; Skorupa, W.
Defect engineering for SIMOX processing
Gettering and Defect Engineering in Semiconductor Technology (GADEST'07), 14.-19.10.2007, Erice, Italy

46. Küpper, K.; Buess, M.; Raabe, J.; Quitmann, C.; Fassbender, J.
Dynamic vortex-antivortex interaction in a single cross-tie wall
6th International Symposium on Metallic Multilayers, 15.-19.10.2007, Perth, Australia

47. Küpper, K.; Marko, D.; Buess, M.; Raabe, J.; Quitmann, C.; Fassbender, J.
Magnetization dynamics of a single cross-tie wall
DPG Jahrestagung und DPG Frühjahrstagung des AKF, 26.-30.03.2007, Regensburg, Germany

48. Kups, Th.; Tonisch, K.; Voelskow, M.; Skorupa, W.; Konkin, A. L.; Pezoldt, J.
Structure and lattice location of Ge implanted 4H-SiC
International Conference on Silicon Carbide and Related Materials 2007 (ICSCRM2007), 14.-19.10.2007, Otsu, Japan

49. Krause, M.; Abrasonis, G.; Kolitsch, A.; Mücklich, A.; Möller, W.
Nickel nanoparticle catalysed formation of fullerene like carbon nanostructures - A Raman analysis
XXIst International Winterschool Molecular Nanostructures, 10.-17.03.2007, Kirchberg, Austria

50. Loppacher, Ch.; Zerweck, U.; Eng, L. M.; Gemming, S.; Seifert, G.; Olbrich, C.; Morawetz, K.; Schreiber, M.
Simulation and AFM-measurement of PTCDA on Ag-supported KBr films
E-MRS 2007 Spring Meeting, 27.05.-01.06.2007, Strasbourg, France

51. Martinavičius, A.; Abrasonis, G.; Möller, W.; Templier, C.; Declemy, A.
Orientation dependant nitrogen diffusion in single crystalline austenitic stainless steel during ion beam nitriding
15th International Summer School on Vacuum, Electron and Ion Technologies (VEIT-2007), 17.-21.09.2007, Sozopol, Bulgaria

52. Martins, R. M. S.; Schell, N.; Borany, J. von; Braz Fernandes, F. M.
In-situ study of the ion bombardment of Ni-Ti thin films
ESRF Users' Meeting 2007, 07.02.2007, Grenoble, France

53. Martins, R. M. S.; Schell, N.; Reuther, H.; Pereira, L.; Silva, R. J. C.; Mahesh, K. K.; Braz Fernandes, F. M.
Characterization of Ni-Ti (Shape Memory Alloy) thin film by in-situ XRD and complementary ex-situ techniques
4th International Materials Symposium (Materials 2007), 01.-04.04.2007, Porto, Portugal

54. Martins, R. M. S.; Beckers, M.; Mücklich, A.; Schell, N.; Silva, R. J. C.; Mahesh, K. K.; Braz Fernandes, F. M.
The interfacial diffusion zone in magnetron sputtered Ni-Ti thin films deposited on different Si substrates studied by HR-TEM
4th International Materials Symposium (Materiais 2007), 01.-04.04.2007, Porto, Portugal

55. Martins, R. M. S.; Schell, N.; Zhou, S.; Beckers, M.; Silva, R. J. C.; Mahesh, K. K.; Braz Fernandes, F. M.
Sputter deposition of high-temperature NiTiHf shape memory thin films
4th International Materials Symposium (Materiais 2007), 01.-04.04.2007, Porto, Portugal

56. Martins, R. M. S.; Mücklich, A.; Schell, N.; Silva, R. J. C.; Mahesh, K. K.; Braz Fernandes, F. M.
Characterization of sputtered Shape Memory Alloy Ni-Ti films by cross-sectional TEM and SEM
International Conference on Microscopy and Microanalysis (INCOMAM-07) - XLII Congress of the Portuguese Microscopy Society, 06.-07.12.2007, Coimbra, Portugal

57. McCord, J.; Fassbender, J.
Hybrid soft-magnetic films with novel functionality created by magnetic property patterning
6th International Symposium on Metallic Multilayers, 15.-19.10.2007, Perth, Australia

58. Möller, W.
Materials research using ion beams at the Dresden Ion Beam Centre
Workshop on Small-Scale Accelerator Facilities, 08.09.2007, Aghios Nikolaos, Greece

59. Möller, W.; Güttler, D.; Abendroth, B.; Grötzschel, R.
Mechanismen und Modellierung der Targetvergiftung beim reaktiven Magnetron- Sputtern
13. Fachtagung Plasmatechnologie, 06.03.2007, Bochum, Germany

60. Möller, W.; Güttler, D.; Cornelius, S.
Puzzling energy and angle distributions of atoms ejected during reactive magnetron sputtering: Effects of target texture?
Symposium on Reactive Sputter Deposition, 06.-07.12.2007, Leoben, Austria

61. Müller, C.; Leonhardt, A.; Elefant, D.; Reuther, H.; Büchner, B.
New aspects about the growth of metal-filled CNT on structured substrates and the tuning of their magnetic properties
8th International Conference on the Science and Application of Nanotubes, 24.-29.06.2007, Ouro Preto, Brasil

62. Munnik, F.; Grambole, D.; Bischoff, L.; Grötzschel, R.
Micro channeling study of crystal damage in ZnO by ion implantation
18th International Conference on Ion Beam Analysis, 23.-28.09.2007, Hyderabad, India

63. Nasdala, L.; Grambole, D.
Raman study of irradiation damage in silicon
Tagung der Österreichischen Mineralogischen Gesellschaft gemeinsam mit dem Geologischen Dienst der Autonomen Provinz Bozen (MinPet 2007), 16.-21.09.2007, Meran, Italy

64. Nasdala, L.; Kronz, A.; Tichomirowa, M.; Grambole, D.; Trullenque, G.
Effects of radiation damage in minerals on their electron back-scatter coefficient
Frontiers in Mineral Sciences, 26.-28.06.2007, Cambridge, UK

65. Novak, P.; Chaplygin, I.; Seifert, G.; Gemming, S.; Laskowski, R.
Ab-initio calculation of exchange interactions in $YMnO_3$
ICMAT07, 01.-06.07.2007, Singapore, Singapore

66. Pankoke, V.; Gemming, S.
Magnetic properties of Pd-films on piezoelectric substrates
EUROMAT 2007, 11.-13.09.2007, Nürnberg, Germany

67. Peter, F.; Nitsche, S.; Winnerl, S.; Dreyhaupt, A.; Schneider, H.; Helm, M.
Terahertz radiation from a large-area photoconductive device
DPG-Frühjahrstagung, 26.-30.03.2007, Regensburg, Germany

68. Popov, A. A.; Dunsch, L.; Krause, M.; Yang, S.; Kalbac, M.
Vibrational spectroscopic and DFT studies of the metal-nitride clusterfullerenes: Cluster-cage interactions and molecular structures
211th ECS Meeting, 06.-10.05.2007, Chicago, USA

69. Posselt, M.; Schmidt, B.; Anwand, W.; Grötzschel, R.; Skorupa, W.; Heera, V.; Gennaro, S.; Bersani, M.; Giubertoni, D.
N-doping by P implantation into pre-amorphized Ge and subsequent annealing: P diffusion, solid-phase-epitaxial regrowth and P activation
CADRES Ge Workshop, 23.01.2007, Ghent, Belgium

70. Posselt, M.; Schmidt, B.; Anwand, W.; Grötzschel, R.; Heera, V.; Wündisch, C.; Skorupa, W.; Hortenbach, H.; Gennaro, S.; Bersani, M.; Giubertoni, D.; Möller, A.; Bracht, H.
P implantation into pre-amorphized germanium and subsequent annealing: Solid phase epitaxial regrowth, P diffusion and activation
International Workshop on INSIGHT in Semiconductor Device Fabrication, Metrology and Modeling (INSIGHT-2007), 06.-09.05.2007, Napa, USA

71. Posselt, M.
Dependence of the correlation factor for self-diffusion by vacancies and self-interstitials on the migration mechanism: An atomistic study
12th International Autumn Meeting Gettering and Defect Engineering in Semiconductor Technology (GADEST 2007), 14.-19.10.2007, Erice, Sicily, Italy

72. Posselt, M.; Bischoff, L.; Grambole, D.; Herrmann, F.
Competition between damage buildup and dynamic annealing in ion implantation into Ge
12th International Autumn Meeting Gettering and Defect Engineering in Semiconductor Technology (GADEST 2007), 14.-19.10.2007, Erice, Sicily, Italy

73. Posselt, M.; Schmidt, B.; Anwand, W.; Grötzschel, R.; Heera, V.; Wündisch, C.; Skorupa, W.; Hortenbach, H.; Gennaro, S.; Bersani, M.; Giubertoni, D.; Möller, A.; Bracht, H.
P-Implantation in voramorphisiertes Ge und anschließende Temperung: Festphasen-Epitaxie, P-Diffusion und -Aktivierung
38. Treffen der Nutzergruppe Ionenimplantation, 09.11.2007, Dresden, Germany

74. Potzger, K.; Anwand, W.; Reuther, H.; Zhou, S.; Talut, G.; Fassbender, J.; Brauer, G.; Skorupa, W.
The effect of flash lamp annealing on Fe implanted ZnO single crystals
71. Jahrestagung der Deutschen Physikalischen Gesellschaft und DPG Frühjahrstagung des Arbeitskreises Festkörperphysik, 26.-30.03.2007, Regensburg, Germany

75. Prinz, M.; Takacs, A. F.; Küpper, K.; Postnikov, A. V.; Scheurer, A.; Saalfrank, R. W.; Sperner, S.; Prince, K. C.; Neumann, M.
Electronic structure study of the "ferric star" single molecule magnet
15th International Conference on Vacuum Ultraviolet Radiation Physics (VUV- XV), 29.07.-03.08.2007, Berlin, Germany

76. Prinz, M.; Voget, S.; Damnik, N.; Raekers, M.; Küpper, K.; Chaudhuri, P.; George, S.; Coldea, M.; Neumann, M.
Magnetism of the single molecule magnet system $[(Mn^{II}L_2)_3Mn^{II}](BF_4)_2$
DPG Jahrestagung und DPG Frühjahrstagung des AKF, 26.-30.03.2007, Regensburg, Germany

77. Prochazka, I.; Cizek, J.; Brauer, G.; Anwand, W.
Slow-positron implantation spectroscopy in nanoscience
Nanostructured Materials for Functional, Structural and Bio-Applications (NANO'07), 08.-10.10.2007, Brno, Czech Republic

78. Quitmann, C.; Back, C.; Buess, M.; Fassbender, J.; Küpper, K.; Raabe, J.
Magnetization dynamics investigated by X-ray microscopy
15th International Conference on Vacuum Ultraviolet Radiation Physics (VUV XV), 29.07.-03.08.2007, Berlin, Germany

79. Raekers, M.; Bartkowski, S.; Küpper, K.; Zhou, S.; Potzger, K.; Postnikov, A.; Uecker, R.; Neumann, M.
Investigation of high-k materials $RScO_3$ (R=Sm, Gd, Dy) by XPS and band structure calculations
DPG Jahrestagung und DPG Frühjahrstagung des AKF, 26.-30.03.2007, Regensburg, Germany

80. Raff, J.; Pollmann, K.; Scholz, A.
Novel photocatalytic nanomaterials for environmental purposes based on bacterial cells and S-layer proteins
1st International Workshop Aquatic Nanosciences and Nanotechnology, 09.-11.12.2007, Wien, Austria

81. Rebohle, L.; Prucnal, S.; Sun, J. M.; Helm, M.; Skorupa, W.
Switchable multi-color light emitter based on Eu-implanted SiO_2 layers confined in a MOS structure
3rd International Workshop on Semiconductor Nanostructures (SEMINANO'07), 13.-16.06.2007, Bad Honnef, Germany

82. Schmidt, B.
Formung von Ge Nanopartikeln mit MeV Ionen
Workshop „Ionenstrahlphysik und Nanotechnologie“, 10.-11.05.2007, Bochum, Germany

83. Schneider, H.; Drachenko, O.; Winnerl, S.; Helm, M.; Walther, M.
Quadratic autocorrelation and photocurrent saturation study in two-photon QWIPs
9th International Conference on Intersubband Transitions in Quantum Wells, 09.-14.09.2007, Ambleside, Cumbria, UK

84. Shengqiang, Z.; Potzger, K.; Talut, G.; Borany, J. von; Skorupa, W.; Helm, M.; Fassbender, J.
Using X-ray diffraction to identify precipitates in transition metal doped semiconductors
52nd Conference on Magnetism and Magnetic Materials and Intermag Conference, 05.-09.11.2007, Tampa, USA

85. Shevchenko, N.; Weber, J.; Kolitsch, A.
Formation and morphology control of nanostructures produced by PIII
Workshop “Beschichtung für Biotechnologie und Medizintechnik”, 16.-17.10.2007, Dresden, Germany

86. Shevchenko, N.; Weber, J.; Kolitsch, A.
Nanostructured metal surfaces by plasma immersion ion implantation
EuroNanoForum 2007, 19.-21.06.2007, Düsseldorf, Germany

87. Shevchenko, N.; Weber, J.; Kolitsch, A.
Nanoporous metal surfaces produced by plasma immersion ion implantation

15th International Summer School on Vacuum, Electron and Ion Technologies (VEIT-2007), 17.-21.09.2007, Sozopol, Bulgaria

88. Shevchenko, N.; Weber, J.; Reuther, H.; Kolitsch, A.
Formation and morphology control of nanostructures produced by PIII
9th International Workshop on Plasma Based Ion Implantation and Deposition (PBII&D '07), 02.-06.09.2007, Leipzig, Germany

89. Skorupa, W.; Rossner, M.; Neelmeijer, C.; Eichhorn, F.; Borany, J. von; Werner, H.; Eule, A.-C.; Schucknecht, T.; Klemm, V.; Rafaja, D.
A new casting technique for the restoration of lead pipes in old organs
E-MRS 2007 Spring Meeting, Workshop: Science & Technology of Cultural Heritage Materials: Art Conservation and Restoration, 28.05.-01.06.2007, Strasbourg, France

90. Stehr, D.; Wagner, M.; Winnerl, S.; Helm, M.; Andrews, A. M.; Roch, T.; Strasser, G.
Picosecond electron dynamics in doped superlattices studied by two-color infrared pump-probe spectroscopy
15th International Conference on Nonequilibrium Carrier Dynamics in Semiconductors, 22.-27.07.2007, Tokyo, Japan

91. Strivay, D.; Ramboz, C.; Gallien, J.-P.; Grambole, D.; Sauvage, T.
Micro-crystalline inclusions analysis by PIXE/RBS
9th European Conference on Accelerators in Applied Research and Technology, 03.-07.09.2007, Florence, Italy

92. Talut, G.; Reuther, H.; Stromberg, F.; Zhou, S.; Potzger, K.; Eichhorn, F.
Ferromagnetism in GaN induced by Fe ion implantation
2nd International Conference on Nanospintronic Design and Realization 2007, 21.-25.05.2007, Dresden, Germany

93. Talut, G.; Reuther, H.; Stromberg, F.; Zhou, S.; Potzger, K.; Eichhorn, F.
Ferromagnetism in GaN induced by Fe ion implantation
International Conference on the Applications of the Mössbauer Effect, 14.-19.10.2007, Kanpur, India

94. Talut, G.; Reuther, H.; Zhou, S.; Potzger, K.
Phase change in Fe implanted rutile TiO_2 after thermal treatment
International Conference on the Applications of the Mössbauer Effect, 14.-19.10.2007, Kanpur, India

95. Talut, G.; Potzger, K.; Mücklich, A.; Zhou, S.
Formation of metallic clusters in oxide insulators by means of ion beam mixing
52nd Conference on Magnetism and Magnetic Materials, 05.-09.11.2007, Tampa, USA

96. Talut, G.; Reuther, H.; Zhou, S.; Potzger, K.
Correlation between magnetic properties and lattice site location of Fe implanted TiO_2 at different temperatures
52nd Magnetism and Magnetic Materials Conference, 05.-09.11.2007, Tampa, Florida, USA

97. Teichert, St.; Muehle, U.; Fachmann, J.; Steinhoff, J.; Kudelka, S.; Wilde, L.; Borany, J. von; Eichhorn, F.
Structural properties of thin HfSiO films
11th International Conference on the Formation of Semiconductor Interfaces (ICFSI), 19.-24.08.2007, Manaus-Amazonas, Brazil

98. Thieme, M.; Gemming, S.
Density functional theory - Investigations of vanadium silicides
DPG-Frühjahrstagung Regensburg, 27.03.2007, Regensburg, Germany

99. Tribuzy, C. V.-B.; Ohser, S.; Sellesk, M.; Winnerl, S.; Schneider, H.; Helm, M.; Neuhaus, J.; Dekorsy, T.; Biermann, K.; Künzel, H.
Inefficiency of intervalley transfer in narrow InGaAs/AlAsSb quantum wells
15th International Conference on Nonequilibrium Carrier Dynamics in Semiconductors (HCIS-15), 23.-27.07.2007, Tokyo, Japan

100. Tribuzy, C. V.-B.; Ohser, S.; Sellesk, M.; Winnerl, S.; Schneider, H.; Helm, M.; Neuhaus, J.; Dekorsy, T.; Biermann, K.; Künzel, K.
Intervally transfer in narrow InGaAS/AlAsSb quantum wells studied by pump-probe spectroscopy
13th International Conference on Narrow Gap Semiconductors, 08.-12.07.2007, Guildford, UK

101. Tribuzy, C. V.-B.; Schneider, H.; Ohser, S.; Sellesk, M.; Winnerl, S.; Grenzer, J.; Helm, M.; Neuhaus, J.; Dekorsy, T.; Biermann, K.; Künzel, H.
Intersubband relaxation dynamics in InGaAs/AlAsSb multiple quantum wells
9th International Conference on Intersubband Transitions in Quantum Wells (ITQW-2007), 14.09.2007, Ambleside, Cumbria, United Kingdom

102. Tyschenko, I. E.; Cherkov, A. G.; Voelskow, M.; Popov, V. P.
Crystallization of InSb phase near the bonding interface of silicon-on-insulator structure
12th GADEST Conference 2007, 14.-19.10.2007, Erice, Italy

103. Tyschenko, I. E.; Cherkov, A. G.; Voelskow, M.; Popov, V. P.
SiGe heterostructures-on-insulator produced by Ge^+-ion implantation and subsequent hydrogen transfer
12th GADEST Conference 2007, 14.-19.10.2007, Erice, Italy

104. Tyschenko, I. E.; Voelskow, M.; Cherkov, A. G.; Popov, V. P.
The properties of the nanometer thick Si/Ge films-on-insulator produced by Ge^+ ion implantation and subsequent hydrogen transfer
3rd International Conference on Micro- Nanoelectronics, Nanotechnology and MEMs (Micro&Nano2007), 18.-21.11.2007, Athen, Greece

105. Tyschenko, I. E.; Voelskow, M.; Cherkov, A. G.; Popov, V. P.
Endotaxial growth of InSb nanocrystals on the bonding interface of silicon-oninsulator structure
3rd International Conference on Micro- Nanoelectronics, Nanotechnology and MEMs (Micro&Nano2007), 18.-21.11.2007, Athen, Greece

106. Vaupel, M.; Vinnichenko, M.
Influence of local plasma flow on optical properties and thickness of ITO-films observed with spectroscopic imaging ellipsometry
4th International Conference on Spectroscopic Ellipsometry, 11.-15.06.2007, Stockholm, Sweden

107. Vinnichenko, M.; Rogozin, A.; Shevchenko, N.; Kolitsch, A.; Möller, W.
Effect of As incorporation on ZnO film structure and dielectric function
13th International Conference on II-VI Compounds, 10.-14.09.2007, Jeju, Korea

108. Vinnichenko, M.; Rogozin, A.; Kolitsch, A.; Möller, W.
Effect of elevated temperature on optical properties of Al-doped polycrystalline ZnO films
Woollam-Ellipsometrie-Seminar, 24.10.2007, Darmstadt, Germany

109. Vinnichenko, M.; Rogozin, A.; Shevchenko, N.; Kolitsch, A.; Möller, W.
Real-time evolution of tin-doped indium oxide film properties during growth and crystallization studied by spectroscopic ellipsometry
4th International Conference on Spectroscopic Ellipsometry, 11.-15.06.2007, Stockholm, Sweden

110. Wagner, M.; Stehr, D.; Schneider, H.; Winnerl, S.; Helm, M.; Andrews, M.; Roch, T.; Strasser, G.
Intersubband-dephasing in an undoped multi-quantum well
71. Jahrestagung der Deutschen Physikalischen Gesellschaft und DPG Frühjahrstagung des Arbeitskreises Festkörperphysik, 26.-30.03.2007, Regensburg, Germany

111. Wagner, M.; Stehr, D.; Winnerl, S.; Helm, M.; Andrews, M.; Roch, T.; Strasser, G.
Two-color pump-probe spectroscopy of electron dynamics in doped superlattices
9th International Conference on Intersubband Transitions in Quantum Wells (ITQW'2007), 09.-14.09.2007, Ambleside, UK

112. Winnerl, S.; Nitsche, S.; Peter, F.; Drachenko, O.; Schneider, H.; Helm, M.; Köhler, K.
Easy-to-use scalable antennas for coherent detection of THz radiation
13th International Conference on Narrow Gap Semiconductors, 08.-12.07.2007, Guildford, UK

113. Winnerl, S.; Peter, F.; Nitsche, S.; Dreyhaupt, A.; Drachenko, O.; Schneider, H.; Helm, M.; Köhler, K.
Coherent detection of terahertz radiation with scalable antennas
Joint 32nd International Conference on Infrared and Millimeter Waves and 15th International Conference on Terahertz Electronics, 02.-09.09.2007, Cardiff, UK

114. Yankov, R. A.; Kolitsch, A.; Steinert, M.; Donchev, A.; Schütze, M.
Oxidation-resistant TiAl alloys produced by plasma immersion ion implantation of fluorine
9th International Workshop on Plasma-Based Ion Implantation & Deposition, 02.-06.09.2007, Leipzig, Germany

115. Yankov, R. A.; Kolitsch, A.; Rogozin, A.; Steinert, M.; Donchev, A.; Schütze, M.
Oxidation-resistant γ-TiAl alloys produced by ion implantation of fluorine
E-MRS Spring Meeting, 28.05.-01.06.2007, Strasbourg, France

116. Zelenetskaya, K.; Jähne, E.; Adler, H.-J.; Loppacher, C.; Eng, L.; Grenzer, J.; Scholz, A.
Investigation on thin films of new substituted quarterthiophene films of new substituted quarterthiophene
DPG Jahrestagung und DPG Frühjahrstagung des AK Festkörperphysik, 26.-30.03.2007, Regensburg, Germany

117. Zhou, S.; Potzger, K.; Borany, J. von; Skorupa, W.; Helm, M.; Fassbender, J.
Structural investigations of magnetic nanocrystals embedded in semiconductors using synchrotron

radiation x-ray diffraction
17th ESRF Users Meeting, 05.-08.02.2007, Grenoble, France

118. Zhou, S.; Potzger, K.; Reuther, H.; Skorupa, W.; Helm, M.; Fassbender, J.
Absence of ferromagnetism in V-implanted ZnO single crystals
71. Jahrestagung der Deutschen Physikalischen Gesellschaft und DPG Frühjahrstagung des AK Festkörperphysik, 26.-30.03.2007, Regensburg, Germany

119. Zhou, S.; Potzger, K.; Skorupa, W.; Helm, M.; Fassbender, J.
Thermal phase transformation and perpendicular exchange coupling of Co nanocrystals embedded in ZnO
71. Jahrestagung der Deutschen Physikalischen Gesellschaft und DPG Frühjahrstagung des AK Festkörperphysik, 26.-30.03.2007, Regensburg, Germany

120. Zhou, S.; Potzger, K.; Borany, J. von; Skorupa, W.; Helm, M.; Fassbender, J.
Structural investigations of magnetic nanocrystals embedded in semiconductors using synchrotron radiation X-ray diffraction
2nd International Conference on Nanospintronic Design and Realization 2007, 21.-25.05.2007, Dresden, Germany

121. Zhou, S.; Potzger, K.; Borany, J. von; Skorupa, W.; Helm, M.; Fassbender, J.
Probing the phase separation in transition metal implanted semiconductors using synchrotron radiation x-ray diffraction
Workshop on Ion Beam Processing and Magnetic Properties of Semiconductors, 13.02.2007, Leuven, Belgium

Lectures

1. Bischoff, L.
Ion beam synthesis of nanoclusters and nanowires by FIB
Indian Association for the Cultivation of Science, 01.10.2007, Kalkutta, India

2. Brauer, G.
Slow positron implantation spectroscopy – A tool to characterize vacancy-type damage in solids
Seminar at Nuclear Physics Institute, 15.06.2007, Rez, Czech Republic
3. *Seminar at Institute of Experimental and Applied Physics, 19.06.2007, Praha, Czech Republic*

4. Brauer, G.; Anwand, W.
Positron annihilation spectroscopy – Its basics and application to ZnO single crystals
Seminar at Institute of Physics, Opole University, 25.10.2007, Opole, Poland
5. *Seminar at Institute of Experimental Physics, Wroclaw University, 26.10.2007, Wroclaw, Poland*

6. Borany, J. von
Nanostrukturen - Neue Konzepte und Verfahren für die Photovoltaik
Gründerimpuls-Veranstaltung "Nanotechnologie", 10.10.2007, Dresden, Germany

7. Cantelli, V.; Grenzer, J.; von Borany, J.
Dual-magnetron sputtering deposition of ferromagnetic FePt layers: In-situ X-ray investigations
Seminar „Neue Entwicklungen in Röntgendiffraktometrie und –topographie“, 24.04.2007, Frankfurt (Oder), Germany

8. Donchev, A.; Kolitsch, A.; Möller, W.; Schütze, M.; Yankov, R.
Implantation of halogens to improve TiAl-components for high temperature applications,
2nd Meeting of the International Advisory Committee of the Ion Beam Centre at FZD, 01.10.2007, Dresden, Germany

9. Fassbender, J.
Tailoring and imaging the magnetization dynamics in microstructures
Seminar, 2. Physikalisches Institut der RWTH Aachen, 12.02.2007, Aachen, Germany
10. *Seminar, Institut für Festkörperforschung des FZ Jülich, 14.02.2007, Jülich, Germany*

11. Fassbender, J.
Ions hit magnetism - New challenges for the design of artificial nanostructures
Seminar, University of Sydney, 09.10.2007, Sydney, Australia
12. *Seminar, Australian National University, 11.10.2007, Canberra, Australia*
13. *Physikalisches Kolloquium, Universität Chemnitz, 14.11.2007, Chemnitz, Germany*
14. *Seminar, Universität Augsburg, 21.11.2007, Augsburg, Germany*

15. Helm, M.
Festkörperspektroskopie bei Terahertz-Frequenzen mit dem Freie-Elektronenlaser
Physikalisches Kolloquium, Universität Konstanz (invited), 26.06.2007, Konstanz, Germany
16. *Physikalisches Kolloquium, Universität Linz (invited), 28.06.2007, Linz, Austria*

17. *Physikalisches Kolloquium, Universität Leipzig (invited), 10.07.2007, Leipzig, Germany*

18. Helm, M.
THz physics at the Research Center Dresden-Rossendorf: From scalable photoconductive THz antennas to near-field microscopy of ferroelectrics using a free-electron laser
Seminar at Physics Department der Kyoto University, Japan, 30.07.2007, Kyoto, Japan

19. Helm, M.
Neuartige Lichtemitter und Nanosonden für zukünftige Optoelektronik und Nanotechnologie
Seminarvortrag, TU Wien, 05.12.2007, Wien, Austria

20. Küpper, K.
Nanomagnetism at the Forschungszentrum Dresden-Rossendorf
MSD Seminar, Argonne National Lab., Argonne, USA, 17.01.2007, Argonne, USA

21. Küpper, K.; Buess, M.; Raabe, J.; Quitmann, C.; Fassbender, J.
Dynamic vortex-antivortex interaction in a single cross-tie wall
Seminar at Université Paris Sud, 30.11.2007, Orsay, France

22. Möller, W.
Nanostructures by ion-driven self-organisation
Seminar, 02.02.2007, GANIL-CIRIL Caen, France
23. *Seminar, 20.03.2007, University of Aarhus, Denmark*
24. *Materials Modelling Seminar, 24.10.2007, Loughborough University, UK*

25. Möller, W.
Nanostrukturen durch Ionen-getriebene Selbstorganisation
Physikalisches Kolloquium der Ruhr-Universität, 22.10.2007, Bochum, Germany

26. Peter, F.; Nitsche, S.; Winnerl, S.; Dreyhaupt, A.; Schneider, H.; Helm, M.
THz Strahlung von einem skalierbaren photoleitenden Emitter
THz – Frischlinge - Meeting, 01.-04.04.2007, Freiburg, Germany

27. Potzger, K.; Zhou, S.; Zhang, G.; Reuther, H.; Talut, G.; Mücklich, A.; Eichhorn, F.; Schell, N.; Grötzschel, R.; Skorupa, W.; Helm, M.; Anwand, W.; Brauer, G.; Fassbender, J.
Diluted magnetic semiconductors created by non-equilibrium processing -new challenges for ion beams
Fachbereichsseminar der AG B.K. Meyer, Universität Giessen, 2.2.2007, Giessen, Deutschland

28. Schneider, H.
Semiconductor spectroscopy with free-electron and tabletop pulsed lasers at FZD
Seminar, 30.01.2007, Santa Barbara, CA, USA

29. Schneider, H.
Time-resolved semiconductor spectroscopy at FZD
Seminar, 07.09.2007, Nottingham, UK

30. Schneider, H.
Time-resolved semiconductor spectroscopy in the mid-infrared and Terahertz regimes
Seminar, 30.11.2007, Palaiseau, France

31. Skorupa, W.
Short time thermal processing of materials - beyond electronics and photonics to pipe organ materials
Seminar, Planck Institut für Mikrostrukturphysik, 05.12.2007, Halle/Saale, Germany

32. Talut, G.
Ionen in der Materialforschung und verdünnte magnetische Halbleiter
Vortrag im Rahmen der Vorlesung zur Oberflächentechnik, 04.05.2007, Wildau, Germany

33. Talut, G.; Reuther, H.; Stromberg, F.; Zhou, S.; Potzger, K.; Grenzer, J.; Mücklich, A.; Eichhorn, F.
Search of the origin of ferromagnetism in DMS
Condensed Matter Seminar, University of Central Florida, 12.11.2007, Orlando, Florida, USA

34. Vinnichenko, M.
Fundamentals and applications of ellipsometry
Informal Seminar at Centro de Micro-Analisis de Materiales (CMAM), 29.06.2007, Madrid, Spain

35. Weishart, H.; Heera, V.
Entwicklung hochtemperaturstabiler Kontakte auf SiC
3. NanoHoch-Projekttreffen, 25.05.2007, Dresden, Germany

36. Winnerl, S.
Das Auflösungsvermögen optischer Mikroskope - Wo liegt die Grenze?
Lehrerfortbildung "Bildgebende Verfahren", 16.02.2007, Dresden, Germany

37. Winnerl, S.; Peter, F.; Dreyhaupt, A.; Nitsche, S.; Drachenko, O.; Schneider, H.; Helm, M.; Köhler, K.
Coherent detection of terahertz radiation with non-resonant antennas
French Russian Seminar: Sources and Detectors of Terahertz Radiation based on Semiconductur Nanostructures, 05.06.2007, Toulouse, France

PhD Theses

1. Kost, D.
Energieeintrag langsamer hochgeladener Ionen in Festkörperoberflächen
TU Dresden, 26.04.2007

2. Röntzsch, L.
Shape evolution of nanostructures by thermal and ion beam processing
TU Dresden, 14.08.2007

3. Stehr, D.
Infrared studies of impurity states and ultrafast carrier dynamics in semiconductor quantum structures
TU Dresden, 11.07.2007

Master & Diploma Theses

1. Kunze, T.
Numerical solution of the equations of motion of a rigid body in an n-dimensional periodic potential
TU Chemnitz, 31.12.2007

2. Nauert, D.
Untersuchungen modifizierter Glasoberflächen
TU Bergakademie Freiberg, 31.03.2007

3. Sellesk, M.
Zeitaufgelöste Intersubbandspektroskopie an InGaAs/AlAsSb-Quantenstrukturen
TU Bergakademie Freiberg, 30.06.2007

4. Silze, A.
Elektronenstoß-Ionisationsquerschnitte hochgeladener Ionen aus zeitaufgelösten Röntgen- und Ionenextraktionsspektren
TU Dresden, 30.11.2007

5. Strache, T.
Magnetische Eigenschaften von ionenstrahlmodifizierten Filmen und Mikrostrukturen
TU Dresden, 12.11.2007

Patents

1. Schütze, M.; Donchev, A.; Yankov, R.; Richter, E.
Erhöhung der Oxidationsbeständigkeit von TiAl-Legierungen durch die kombinierte Implantation von Fluor und Silizium
DE 10 2006 043 436 B3

2. Voelskow, M.; Anwand, W.; Skorupa, W.
Verfahren zur Behandlung von Halbleitersubstraten, die mittels intensiven Lichtimpulsen ausgeheilt werden
DE 10 2005 036 669 A1

3. Voelskow, M.; Skorupa, W.; Anwand, W.
Verfahren zur Behandlung von Halbleiter-Substratoberflächen, die mittels intensiven Lichtimpulsen kurzzeitig aufgeschmolzen werden
DE 10 2005 036 669 A1
EP 06 013 986

Organization of Workshops

1. Borany, J. von, Brauer, G., Skorupa, W.
   22. Treffen der Nutzergruppe RTP
   08.-09.11.2007, Dresden, Germany

2. Grötzschel, R.
   International Workshop on High-Resolution Depth Profiling
   17.-21.06.2007, Radebeul, Germany

3. Heinig, K.-H.
   International Workshop on SEMIconductor NANOstructures (SEMI-NANO 2007)
   13.-16.06.2007, Bad Honnef, Germany

4. Möller, W.; Guerassimov, N.
   15th International School on Vacuum, Electron, and Ion Technologies (VEIT 2007)
   17.-21.09.2007, Sozopol, Bulgaria

Laboratory Visits

1. Abrasonis, G.
   ESRF Grenoble, France; 14.-18.05.2007
   Lawrence Berkeley Naional Lab, USA; 21.10.-11.11.2007
   University of Sydney, Australia; 21.06.-23.07.2007

2. Bähtz, C.
   ESRF Grenoble, France; 12.02.-01.03., 25.-30.11.2007

3. Borany, J. von
   ESRF Grenoble, France; 12.-23.02., 18.-23.03., 05.-08.11., 03.-09.12., 13.-17.12.2007

4. Drachenko, O.
   Toulouse High Magnetic Field Lab, France; 01.01.-11.02.2007
   University of Kiew, Ukraine; 14.06.-02.07.2007
   Institute for Physics of Microstructures Nizhny Novgorod, Russia; 05.-12.10.2007

5. Facsko, S.
   ESRF Grenoble, France; 05.-08.12.2007

6. Grenzer, J.
   ESRF Grenoble, France; 20.-28.02., 12.-19.03., 30.04.-05.05., 25.09.-04.10., 05.-08.11., 04.-11.12.2007

7. Hanisch, A.
   ESRF Grenoble, France; 30.04.-08.05., 15.-19.05., 04.-11.12.2007

8. Heller, R.
   Jagellonian University Krakow, Poland; 03.-14.12.2007

9. Jeutter, N.
   ESRF Grenoble, France, 25.-30.11.2007

10. Keller, A.
    ESRF Grenoble, France; 20.-28.02., 01.-07.05., 03.-11.12.2007

11. Küpper, K.
    Lawrence Berkeley National Laboratory, USA; 05.-20.02., 04.-15.09.2007
    Swiss Light Source, PSI Villigen, Switzerland; 06.-10.03., 22.-26.06., 09.-15.08., 07.-12.12.2007

12. Markó, D.
    Swiss Light Source, PSI Villigen, Switzerland, 06.-10.03.2007
    Lawrence Berkeley National Laboratory, USA; 11.10.-04.11.2007

13. Martinavicius, A.
    University of Poitiers, France; 03.-14.07.2007

14. Martins, R. M. S.
    ESRF Grenoble, France; 21.-24.02.2007

15. Potzger, K.
Lawrence Berkeley National Laboratory, USA; 13.–20.02., 04.-15.09.2007

16. Rogozin, A.
ESRF Grenoble, France; 09.-17.07.2007

17. Shalimov, A.
ESRF Grenoble, France; 23.-30.08.2007

18. Shevchenko, N.
ESRF Grenoble, France; 09.-17.07.2007
Sibian Physical and Technical Institute, Tomsk, Russia; 23.-26.07.2007

19. Talut, G.
ESRF Grenoble, France; 25.09.-04.10.2007

20. Winnerl, S.
Toulouse High Magnetic Field Lab, France; 04.-08.06.2007

21. Wintz, S.
Swiss Light Source, PSI Villigen, Switzerland; 22.-26.06.,09.-15.08., 06.-11.12.2007
Lawrence Berkeley National Laboratory, USA; 09.-15.09.2007

22. Zhou, S.
ESRF Grenoble, France; 05.-09.02., 05.-08.05., 23.-30.08.2007

Guests

1. Abd El-Rahman, A.-M.
Sohag University, Egypt; 30.07.-25.08.2007

2. Aronzon, B.
Kurchatov Institute Moscow, Russia; 12.-15.08.2007

3. Bilek, M.
University of Sydney, Australia; 08.-12.01., 08.-15.09.2007

4. Bukas, V.-J.
University of Athens, Greece; 25.06.-17.08.2007

5. Cheng, R.
University of Lanzhou, China; 03.12.2007-30.11.2008

6. Dev, B.
University of Bhubaneswar, India; 01.–04.11.2007

7. Eslam, M.-I.
Sohag University, Egypt; 30.07.–11.08.2007

8. Gordillo, N.
Universtidad Autonoma de Madrid, Spain; 05.-31.03.2007

9. Grynszpan, R.
ESRF Grenoble, France; 25.09.–01.10.2007

10. Hultman, L.
Linköping University, Sweden; 12.-18.08.2007

11. Kuriplach, J.
Charles Universtity Prague, Czech Republic; 03.–18.10., 06.-19.12.2007

12. Lasse, V.
University of Oslo, Norway; 07.05-01.06.2007

13. Lyon, S.
Princeton University, USA; 02.-14.07.2007

14. Medhisuwakul, M.
Chiang Mai University, Thailand; 01.10.-31.12.2007

15. Miletic, A.
Universtity of Novi Sad, Serbia; 28.02.-30.04.2007

16. Minniti, M.
Università della Calabria, Italy; 10.02.-31.12.2007

17. Muzalkova, M.
University of Lipetsk, Russia; 04.02.-04.03.2007

18. Nazarov, A.
Academy of Science, Ukraina; 09.07.-22.08.2007

19. Odor , G.
KEKI Budapest, Hungary; 06.-14.09.2007

20. Peng, H.
University of Lanzhou, China; 03.12.2007–30.11.2008

21. Polmann, A.
FOM Amsterdam, Netherlands; 30.09.-01.10.2007

22. Polyakov, A.
University of Lipetsk, Russia; 09.11.-08.12.2007

23. Priolo, F.
University of Catania, Italy; 30.09.-01.10.2007

24. Prochazka, I.
Charles Universtity Prague, Czech Republic; 15.–23.10., 29.10.-18.11.2007

25. Prucnal, S.
University Marie-Sklodovska-Curie, Poland; 04.03.-04.04., 01.– 31.10.2007

26. Ricardi, P.
Università della Calabria, Italy; 05.-07.11.2007

27. Stolterfoht, N.
University of Florida, USA; 08.-10.10.2007

28. Sun ,J.
Nankai University, China; 01.11.-31.12.2007

29. Stritzker, B.
Universität Augsburg, Germany; 30.09.-01.10.2007

30. Tsyganov, I.
University of Lipetsk, Russia; 01.03.-01.09.2007

31. Tyagulskyy, I.
Academy of Science, Ukraina; 09.07.-22.08.2007

32. Vasilyeva, E.
University of Lipetsk, Russia; 15.03.-15.04.2007

33. Vredenberg, A.
University of Utrecht, Netherlands; 16.–19.01., 27.-30.08.2007

34. Wang, T.
Lanzhou University, China; 20.-29.06.2007

35. Weber, E.
Fraunhofer ISE Freiburg, Germany; 30.09.-01.10.2007

36. Ziemann, P.
Universität Ulm, Germany; 30.09.-01.10.2007

AIM Visitors

1. Arab, Z.
   University of Poitiers, France; 05.–12.02., 25.06.–06.07.2007
2. Boycheva, T.
   University of Sofia, Bulgaria; 07.–20.10.2007
3. Bugoi, R.
   Institute of Atomic Physics Bukarest, Romania; 01.–08.07.2007
4. Constantinescu, B.
   Institute of Atomic Physics Bukarest, Romania; 01.–08.07.2007
5. Cordillo, N.
   Universidad de Madrid, Spain; 18.02.–04.04.2007
6. Danesh, P.
   Institute of Solid State Physics Sofia, 04.11.–03.12.2007
7. Dekov, V.
   University of Sofia, Bulgaria; 07.–20.10.2007
8. Depla, D.
   University of Ghent, Belgium; 20.–26.05.2007
9. Duquenne, C.
   Université de Nantes, France; 26.02.–23.03., 18.–29.06.2007
10. Gomez, P.
    Universidad de Sevilla, Spain; 10–29.09.2007
11. Jagielski, J.
    ITME Warschau Poland; 18.–24.03.2007
12. Mahieu, S.
    University of Ghent, Belgium; 20.–26.05.2007
13. Menendez, E.
    Universidad de Barcelona, Spain; 10.–18.09.2007
14. Niklaus, M.
    ETH Lausanne, Switzerland; 16.–21.04.2007
15. Pagowska, K.
    ITME Warschau, Poland; 25.02.–03.03., 13.–18.05., 11.–16.06., 09.–15.12.2007
16. Palmero, A.
    Universidad de Sevilla, Spain; 10.–28.09.2007
17. Pantchev, B.
    Institute of Solid State Physics Sofia, Bulgaria; 04.11.–03.12.2007
18. Prucnal, S.
    University of Lublin, Poland; 14.05.–30.06.2007
19. Ratajczak, R.
    ITME Warschau, Poland; 18.–24.03., 15.–21.04., 15.–18.05., 11.–16.06., 09.–15.12.2007
20. Ritter, R.
    Universität Wien, Austria; 19.–31.08.2007
21. Schoendorfer, C.
    Universität Wien, Austria; 21.–25.05.2007
22. Sherif El-Said, A.
    Universität Wien, Austria; 19.–24.08.2007
23. Stonert, A.
    ITME Warschau, Poland; 18.–24.03., 15.–21.04.2007
24. Sulser, F.
    ETH Zürich, Switzerland; 21.–26.10.2007

25. Tsvetkova, T.
BAS Sofia, Bulgaria; 16.–30.06.2007

26. Turos, A.
ITME Warschau, Poland; 25.02.–03.03., 11.–16.06., 09.–15.12.2007

27. Vaczi, T.
Universität Wien, Austria; 04.-10.11.2007

28. Wirth, E.
University of Lei, Lithuania; 01.–09.12.2007

IA-SFS Visitors

1. Carpenter, B.
University of Sheffield, UK; 05.-10.02.2007

2. Ceponkus, J.
University of Vilnius, Poland; 18.-25.02., 21.-28.04.2007

3. Fromherz, T.
Universität Linz, Austria; 18.-25.11.2007

4. Jobson, K.
University of Sheffield, UK; 18.-24.02.2007

5. Khalil, G. E.
University of Sheffield, UK; 18.-24.02.2007

6. Porter, N.
University of Sheffield, UK; 26.-30.11.2007

7. Sablinskas, V.
University of Vilnius, Poland; 18.-25.02., 21.-28.04.2007

8. Wilson, L.
University of Sheffield, UK; 24.-29.09., 26.-28.11.2007

9. Zibik, E.
University of Sheffield, UK; 05.-11.02.2007

ROBL-MRH Visitors

1. Beckers, M.
Thin Film Physics Division, Linköping University, Schweden; 05.–10.04., 07.–13.11.2007

2. Biermans, A.
Fachbereich Festkörperphysik, Universität Siegen, Germany; 14.–20.11.2007

3. Braz Fernandes, F. M.
CENIMAT, Universidade Nova de Lisboa, Monte da Caparica, Portugal; 14.–21.02.2007

4. Brüser, B.
Fachbereich Festkörperphysik, Universität Siegen, Germany; 14.–19.03.2007

5. Caha, O.
Institute of Condensed Matter Physics, University of Brno, Czech Republic; 30.08.–05.09.2007

6. Eriksson, F.
Thin Film Physics Division, Linköping University, Schweden; 07.–13.11.2007

7. Feydt, J.
Department of Electron Microscopy, CÄSAR Research Center, Bonn, Germany; 04.– 08.12.2007

8. Gaca, J.
Institute of Electronic Materials Technology, Warszawa, Poland; 18.–21.07.2007

9. Grigorian, S.
Fachbereich Festkörperphysik, Universität Siegen, Germany; 14.–19.03.2007

10. Keplinger, M.
Institut für Halbleiterphysik, Universität Linz, Austria; 30.08.–05.09.2007

11. Kräußlich, Je
Institut für Optik- und Quantenelektronik, Universität Jena, Germany; 21.–24.07., 08.-11.12.2007

12. Krüger, S.
Institut für Röntgenphysik, Universität Göttingen, Germany, 20.–26.06.2007

13. Krügener, J.
Qimonda Dresden, Dresden, Germany; 14.–17.12.2007

14. Kurtulus, Ö.
Fachbereich Festkörperphysik, Universität Siegen, Germany; 14.–20.11.2007

15. Lauridsen, J.
Thin Film Physics Division, Linköping University, Schweden; 07.–13.11.2007

16. Mazur, K.
Institute of Electronic Materials Technology, Warszawa, Poland; 18.–21.07.2007

17. Meduna, M.
Institute of Condensed Matter Physics, University Brno, Czech Republic; 30.08.–05.09.2007

18. Pietsch, U.
Fachbereich Festkörperphysik, Universität Siegen, Germany; 14.–19.03.2007

19. Rinderknecht, J.
AMD Saxony, Dresden, Germany; 25.04.–01.05., 19.–25.09.2007

20. Prinz, H.
AMD Saxony, Dresden, Germany; 25.04.–01.05, 19.–25.09.2007

21. Salditt, T.
Institut für Röntgenphysik, Universität Göttingen, Germany; 20.–26.06.2007

22. Schell, N.
GKSS, Geesthacht, Germany; 14.–21.02.2007

23. Silva, R. J. C.
Materials Science Department & CENIMAT, Universidade Nova de Lisboa, Monte da Caparica, Portugal, 14.–21.02. 2007

24. Slobodsky, T.
Institut für Synchrotronstrahlung, Forschungszentrum Karlsruhe, Germany; 14.–21.02.2007

25. Teichert, S.
Fraunhofer Center Nanolectronic Technology (CNT), Dresden, Germany; 19.–21.03., 14.–17.12.2007

26. Wilde, L.
Fraunhofer Center Nanolectronic Technology (CNT), Dresden, Germany; 19.-21.03., 14.-17.12.2007

27. Wojcik, M.
Institute of Electronic Materials Technology, Warszawa, Poland; 18.–21.07.2007

28. Uschmann, I.
Institut für Optik- und Quantenelektronik, Universität Jena, Germany; 21.–24.07.2007

29. Zastrau, U.
Institut für Optik- und Quantenelektronik, Universität Jena, Germany; 21.–24.07., 08.–11.12.2007

30. Zienert, I.
AMD Saxony, Dresden, Germany; 25.04.–01.05., 19.–25.09.2007

31. Zotov, N.
Department of Electron Microscopy, CÄSAR Research Center, Bonn, Germany; 04.–08.12.2007

Colloquium

1. Albrecht, M. – Universität Konstanz, Germany
   Magnetische Filme auf selbstorganisierten Partikelmonolage*n*
   08.02.2007

2. Bilek, M. - University of Sydney, Australia
   Linking disciplines: Covalent attachment of bioactive proteins to plasma treated polymeric surfaces
   13.09.2007

3. Boutard, J.-L. – EFDA Close Support Unit Garching, Germany
   Highly irradiated structural materials for fusion reactor: Experimental results and multiscale modelling
   31.08.2007

4. Doebeli, M. – Paul-Scherrer-Institut Zürich, Switzerland
   Beschleunigermassenspektrometrie und ihre Anwendungen in der Materialforschung
   05.07.2007

5. Frey, L. – TU/ Bergakademie Freiberg, Germany
   Lösen neue Materialien die Probleme der Mikro- und Nanoelektronik?
   19.07.2007

6. Gross, R. – Bayerische Akademie der Wissenschaften – TU München, Germany
   Multifunctional oxide thin films and heterostructures
   15.03.2007

7. Hultman, L. – Linköping University, Sweden
   Material science studies of nanostructured functional thin films
   16.08.2007

8. Kutschera, W. – Universität Wien, VERA Laboratory, Austria
   The puzzle of dating the volcanic eruption of Santorini, a crucial time marker for the second Millennium BC
   25.10.2007

9. Lyon, S. - Department of Electrical Engineering, Princeton University, USA
   Electron spin coherence in silicon for quantum computing
   12.07.2007

10. Mücklich, F. –Universität des Saarlandes, Saarbrücken, Germany
    Neue Gefügearchitekturen durch Laser-Interferenz-Metallurgie
    18.01.2007

11. Quitmann, C. – Paul-Scherrer-Institut Villigen, Switzerland
    The dance of the domains: Excitations and switching in magnetic microparticles
    01.02.2007

12. Scheffler, M. – FHI Berlin, Germany
    Get Real! The importance of complexity for understanding the function of materials
    25.01.2007

13. Schneider, R. – MPI für Plasmaphysik Greifswald, Germany
    Plasma-edge physics: A bridge between disciplines
    24.04.2007

Seminars

1. Aeschlimann, M. – Universität Kaiserslautern, Germany
   Time resolved photoemission
   05.07.2007

2. Aharonovich, A.– University of of Melbourne, Australia
   Controlled formation of single photon
   Controlled entres in diamond for quantum applications
   17.01.2007

3. Awazu, K. - University of Tokyo & Centre of Applied Near-Field Optics Research, National Institute of Advanced Industrial Science and Technology, Japan

Three dimensional nano-order fabrications of TiO_2 and SiO_2 by swift heavy ions
26.10.2007

4. Baberschke, K. – FU Berlin, Germany
Why are spin wave excitations all important in nanoscale magnetism?
17.04.2007

5. Conradie, L. – LABS South Africa
The status and new developments at iThemba LABS/ South Africa
10.07.2007

6. Gerasimenko, N. - Moscow Institute for Electronic Technology, Russia
Radiation methods for nanoelectronic technology
20.12.2007

7. Habicht, S. - Arizona State University, Tempe, USA
Moderne Fehleranalyse-Methoden: Untersuchungen zur Wirkung des 1064 / 1320 nm Lasers an ausgewählten Strukturen
21.12.2007

8. Klug, J. – Rubion Bochum, Germany
Bochumer Hochstrom-Heliumionenquelle (Torvis von NEC)
02.02.2007

9. Lenz, K.- FU Berlin, Germany,
Ferromagnetic Resonance – a small tool to study static and dynamic magnetic properties
28.01.2007

10. Maziewski, A. - Institut of Physics, University of Bialystok, Poland
Experimental and theoretical studies of Co nanostructures
12.12.2007

11. Moser, J. – Universität Konstanz, Germany
Magnetoresistive effects in Co/Pd multilayers on self-assembled nanospheres
21.01.2007

12. Muñoz-García, J. - Departamento de Matematicas. Facultad de Ciencias u´ımicas.
Universidad de Castilla-La Mancha Ciudad Real, Spain
Invariance scale and pattern formation on ion-sputtered surfaces: A new theoretical two-field coupled model
16.10.2007

13. Nogues, J. - Institut Català de Nanotechnologia Barcelona/ Spain
Using exchange bias to control magnatic vortices
24.10.2007

14. Numazawa, S. - TU Dresden, Germany
Ein funktionentheoretischer Zugang zu einem "terrainfolgenden" Boussines System für lange Oberflächenwasserwellen
16.11.2007

15. Savchenko, E. – National Academy of Science, Ukraine
Electronically induced defect generation and relaxation processes in atomic solids
25.10.2007

16. Whitlow, H. - University Jyväskylä, Finnland
Ion beam applications in biomedical technology
29.10.2007

Projects

1. 03/2004 – 02/2009 European Union EU
IA-SFS - Integrating activity on synchrotron and free electron laser science
Prof. M. Helm Tel.: 0351 260-2260 m.helm@fzd.de

2. 09/2004 – 08/2007 WTZ with Russia WTZ
Titan im Blutkontakt
Dr. A. Kolitsch Tel.: 0351 260 3348 a.kolitsch@fzd.de

3. 11/2004 – 12/2008 Silicon Sensor Berlin GmbH Industry
Hochenergie-Ionenimplantation für optische Sensoren
Dr. J. von Borany Tel.: 0351 260 3378 j.v.borany@fzd.de

4. 01/2005 – 12/2008 European Union EU
EuroMagNET – A coordinated approach to access, experimental development and scientific exploitation of European large infrastructures for high magnetic fields
Prof. M. Helm Tel.: 0351 260 2260 m.helm@fzd.de

5. 04/2005 – 12/2007 DEGUSSA AG Industry
Untersuchungen zur Blitzlampentemperung beschichteter Substrate
Dr. W. Skorupa Tel.: 0351 260 3612 w.skorupa@fzd.de

6. 04/2005 – 06/2007 Arbeitsgemeinschaft industrieller Forschungsvereinigungen AiF
Oxidationsschutz für neuartige Hochtemperatur-Leichtbauwerkstoffe durch Ionenimplantation (III)
Dr. A. Kolitsch Tel.: 0351 260 3348 a.kolitsch@fzd.de

7. 04/2005 – 03/2010 European Union EU
PRONANO – Technology for the production of massively parallel intelligent cantilever-probe platforms for nanoscale analysis and synthesis
Dr. B. Schmidt Tel.: 0351 260 2726 bernd.schmidt@fzd.de

8. 06/2005 – 06/2008 Deutsche Forschungsgemeinschaft DFG
Mössbauerspektroskopie an ionenimplantierten magnetischen Halbleitern
Dr. H. Reuther Tel.: 0351 260 2898 h.reuther@fzd.de

9. 07/2005 – 06/2007 Robert Bosch GmbH Industry
NanoHoch - Nanostrukturierte Hochtemperatur-Halbleiter für integrierte Abgassensoren in Dieselmotor- und Magermotorapplikationen
Dr. V. Heera Tel.: 0351 260 3343 v.heera@fzd.de

10. 09/2005 – 02/2010 European Union EU
FOREMOST – Fullerene-based opportunities for robust engineering: Making optimised surfaces for tribology
Dr. A. Kolitsch Tel.: 0351 260 3348 a.kolitsch@fzd.de

11. 11/2005 – 10/2007 Eifeler GmbH Industry
Technologietransfer c- BN
Dr. A. Kolitsch Tel.: 0351 260 3348 a.kolitsch@fzd.de

12. 01/2006 – 03/2007 Boston Scientific Scimed Industry
Nitinol II
Dr. A. Kolitsch Tel.: 0351 260 3348 a.kolitsch@fzd.de

13. 01/2006 - 12/2009 European Union EU
ITS-LEIF - Ion technology and spectroscopy at low energy ion beam facilities
Dr. S. Facsko Tel.: 0351 260 2987 s.facsko@fzd.de

14. 02/2006 - 01/2010 European Union EU
AIM - Center for application of ion beams to materials research
Dr. A. Kolitsch Tel.: 0351 260 3348 a.kolitsch@fzd.de

15. 07/2006 - 09/2007 Deutsche Forschungsgemeinschaft DFG
Hybrid-Modell
Dr. S. Gemming Tel.: 0351 260 2470 s.gemming@fzd.de

16. 07/2006 - 10/2009 Deutsche Forschungsgemeinschaft DFG
Magnetschicht (FOR520)
Dr. S. Gemming Tel.: 0351 260 2470 s.gemming@fzd.de

17. 08/2006 - 11/2007 Sächsisches Staatsministerium für Wirtschaft und Arbeit SMWA
Solarmetall - Entwicklung und Optimierung der optisch transparenten und elektrisch leitfähigen Deckschicht
Dr. A. Kolitsch Tel.: 0351 260 3348 a.kolitsch@fzd.de

18. 12/2006 - 11/2008 Qimonda Dresden Industry
Ionenstreu-Analysen an Halbleiter-Materialien
Dr. R. Grötzschel Tel.: 0351 260 3294 r.groetzschel@fzd.de

19. 11/2006 - 12/2007 Qimonda Dresden Industry
Röntgenbeugungs-Analysen an Halbleiter-Materialien
Dr. J. von Borany Tel.: 0351 260 3378 j.v.borany@fzd.de

20. 12/2006 - 11/2007 Sächsisches Staatsministerium für Wirtschaft und Arbeit SMWA
Materialcharakterisierung MUSIGUSS
Dr. W. Skorupa Tel.: 0351 260 3612 w.skorupa@fzd.de

21. 12/2006 - 11/2008 Arbeitsgemeinschaft industrieller Forschungsvereinigungen AiF
Nanomorph - Amorphe Nanostrukturen
Dr. A. Kolitsch Tel.: 0351 260 3348 a.kolitsch@fzd.de

22. 01/2006 – 12/2007 DAAD-Portugal DAAD
Erzeugung und Charakterisierung von Ni-Ti Shape Memory Dünnschicht-Legierungen
Dr. N. Schell Tel.: +33 (0)4.76.88.23.67 schell@esrf.fr

23. 07/2006 – 09/2006 ICT GmbH Industry
Fertigung von PrSi-LAMS Emittern
Dr. B. Schmidt Tel.: 0351 260 2726 bernd.schmidt@fzd.de

24. 11/2006 – 06/2008 SARAD GmbH Industry
Entwicklung und Herstellung von ionenimplantierten Si-Strahlungsdetektoren
Dr. B. Schmidt Tel.: 0351 260 2726 bernd.schmidt@fzd.de

25. 11/2006 – 01/2007 ETH Zürich Industry
Herstellung und Untersuchung von co-implantierten Schichtstrukturen
Dr. B. Schmidt Tel.: 0351 260 2726 bernd.schmidt@fzd.de

26. 12/2006 – 12/2009 VKTA e.V. Dresden Bilateral
Durchführung von REM- bzw. EDX- sowie Mössbauer-spektroskopischen Untersuchungen an Metallproben
Dr. H. Reuther Tel.: 0351 260 2898 h.reuther@fzd.de

27. 01/2007 - 09/2007 Deutsche Forschungsgemeinschaft DFG
Grenz- und Oberflächen von ferroischen Schichten
Dr. S. Gemming Tel.: 0351 260 2470 s.gemming@fzd.de

28. 02/2007 - 12/2007 ICT GmbH Industry
PrSi-Ionenquellen
Dr. B. Schmidt Tel.: 0351 260 2726 bernd.schmidt@fzd.de

29. 02/2007 - 03/2008 Alexander-von-Humboldt-Stiftung AvH
Gastaufenthalt Dr. C. Grimm
Prof. M. Helm Tel.: 0351 260 2260 m.helm@fzd.de

30. 04/2007 - 12/2007 Boston Scientific Scimed Inc. Industry
Nanoporous
Dr. A. Kolitsch Tel.: 0351 260 3348 a.kolitsch@fzd.de

31. 04/2007 - 12/2007 AMD Saxony Industry
ROBL-Röntgenuntersuchungen
Dr. J. von Borany Tel.: 0351 260 3378 j.v.borany@fzd.de

32. 04/2007 - 03/2009 Arbeitsgemeinschaft industrieller Forschungsvereinigungen AiF
Unterdrückung der Sauerstoffversprödung von Titanlegierungen
Dr. A. Kolitsch Tel.: 0351 260 3348 a.kolitsch@fzd.de

33. 04/2007 - 03/2009 Deutsche Forschungsgemeinschaft DFG
Ion-beam induced rippling at the amorphous-crystalline interface in silicon
Dr. J. Grenzer Tel.: 0351 260 3389 j.grenzer@fzd.de

34. 05/2007 - 06/2009 Deutsche Forschungsgemeinschaft DFG
Strukturübergänge eingebetteter magnetischer Nanopartikel
Dr. K. Potzger Tel.: 0351 260 3148 k.potzger@fzd.de

35. 07/2007 - 12/2008 Deutsche Forschungsgemeinschaft DFG
Hybride Magnetische Materialien
Dr. J. Fassbender Tel.: 0351 260 3096 j.fassbender@fzd.de

36. 08/2007 - 07/2009 Arbeitsgemeinschaft industrieller Forschungsvereinigungen AiF
Grenzen des Halogeneffektes für TiAl-Hochtemperaturleichtbaulegierungen unter industriellen Bedingungen
Dr. A. Kolitsch Tel.: 0351 260 3348 a.kolitsch@fzd.de

37. 08/2007 - 11/2010 Deutsche Forschungsgemeinschaft DFG
Nanostrukturierung von Oberflächen mit direkter Extraktion der Ionen aus Plasmaquellen
Dr. S. Facsko Tel.: 0351 260 2987 s.facsko@fzd.de

38. 08/2007 - 10/2010 Deutsche Forschungsgemeinschaft DFG
Selbstorganisierte Nanostrukturen durch niederenergetische Ionenstrahlerosion
Dr. K.-H. Heinig Tel.: 0351 260 3288 k.h.heinig@fzd.de

39. 08/2007 - 08/2008 Bundesministerium für Bildung und Forschung BMBF
Magnetoelektronik ferromagnetischer Traps
Dr. H. Schmidt Tel.: 0351 260 2724 heidemarie.schmidt@fzd.de

40. 08/2007 - 12/2008 Deutsche Forschungsgemeinschaft DFG
Ferromagnetism in transition metal doped ZnO
Dr. H. Schmidt Tel.: 0351 260 2724 heidemarie.schmidt@fzd.de

41. 09/2007 - 08/2009 European Union EU
TEMPUS courses of materials science
Prof. W. Möller Tel.: 0351 260 2245 w.moeller@fzd.de

42. 09/2007 - 02/2008 AMD Saxony Industry
Experimente an ROBL-Beamline
Dr. J. von Borany Tel.: 0351 260 3378 j.v.borany@fzd.de

43. 09/2007 - 10/2010 Deutsche Forschungsgemeinschaft DFG
Infrared scattering near-field optical microscopy near dielectric (polaritonic) resonances using a free-electron laser
Prof. M. Helm Tel.: 0351 260 2260 m.helm@fzd.de

44. 10/2007 - 09/2008 Alexander-von-Humboldt-Stiftung AvH
Gastaufenthalt Dr. A. Kanjilal
Prof. M. Helm Tel.: 0351 260 2260 m.helm@fzd.de

45. 10/2007 - 09/2009 Dechema Dechema
Haifischhaut
Dr. A. Kolitsch Tel.: 0351 260 3348 a.kolitsch@fzd.de

46. 11/2007 - 10/2009 Eifeler GmbH Industry
Technologietransfer c-BN II
Dr. A. Kolitsch Tel.: 0351 260 3348 a.kolitsch@fzd.de

47. 12/2007 - 11/2009 Deutsche Forschungsgemeinschaft DFG
Mössbauerspektroskopie an magnetischen Halbleitern II
Dr. H. Reuther Tel.: 0351 260 2898 h.reuther@fzd.de

Experimental Equipment

1. Accelerators, Ion Implanters and Ion-Assisted-Deposition

⇒	Van de Graaff Accelerator	(VdG)	1,8 MV	*TuR Dresden, DE*
⇒	Tandem Accelerator	(Td)	5 MV	*NIIEFA, RU*
⇒	Tandetron Accelerator	(Tdtr)	3 MV	*HVEE, NL*
⇒	Low-Energy Ion Implanter		0.5 - 50 kV	*Danfysik, DK*
⇒	High-Current Ion Implanter		20 - 200 kV	*Danfysik, DK*
⇒	High-Energy Ion Implanter		40 - 500 kV	*HVEE, NL*
⇒	Plasma Immersion Ion Implantation		5 - 60 keV	*GBR, D / Home-built*
⇒	Focused Ion Beam (15 nm)		30 keV, 10 A/cm²	*Orsay Physics, FR*
⇒	Highly-Charged Ion Facility		25 eV – 25 keV × Q Q = 1…40 (Xe)	*Home-built*
⇒	Dual-Beam Magnetron Sputter Deposition			*Roth & Rau; DE*
⇒	Ion-Beam-assisted Deposition			*Danfysik, DK / Home-built*
⇒	Ion-Beam Sputtering		200 - 2000 V	*Home-built*
⇒	UHV Ion Irradiation (Ar, He, etc.)		0 - 5 keV Scan 10×10 mm²	*VG, USA*

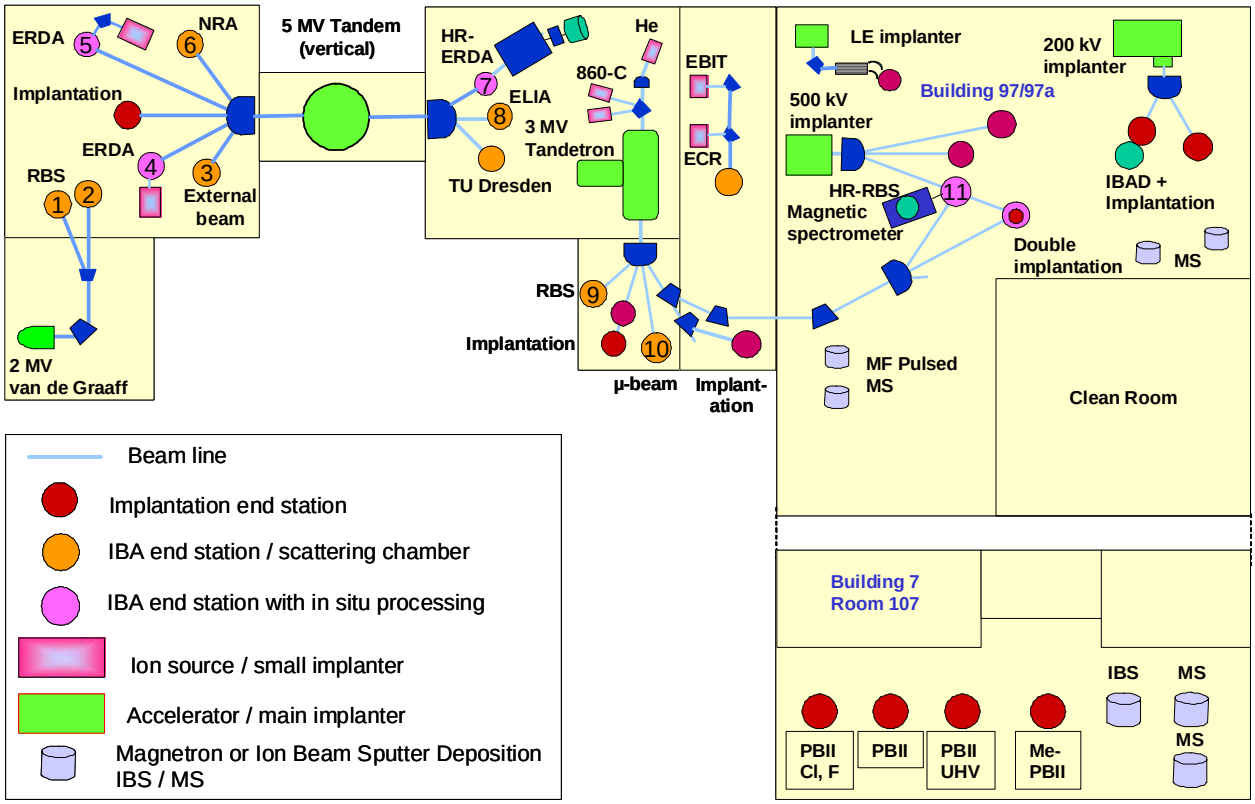

Ion Beam Centre: Schematic Overview of the Installations.

2. Ion Beam Analysis (IBA)

A wide variety of advanced IBA techniques are available at the MeV accelerators (see fig.).

⇒	RBS	Rutherford Backscattering	(1), (2), (3), (9)	*VdG, Td, Tdtr*
⇒	RBS/C	RBS + Channelling	(1), (2), (3), (9)	*VdG, Td, Tdtr*
		High-Resolution RBS/C	(11)	*Tdtr*

⇒	ERDA	Elastic Recoil Detection Analysis	(2), (4), (5)	*VdG, Td*
		High-resolution ERDA	(7), (8)	*Td*
⇒	PIXE	Proton-Induced x-ray Emission	(3)	*Td*
⇒	PIGE	Proton-Induced γ Emission	(3)	*Td*
⇒	NRA	Nuclear Reaction Analysis	(4)	*Td*
⇒	NRRA	Nuclear Resonance Reaction Anal.	(6)	*Td*
⇒		Nuclear Microprobe	(10)	*Tdtr*

Some stations are equipped with additional process facilities which enable *in-situ* IBA investigations during ion irradiation, sputtering, deposition, annealing etc.

3. Other Particle Based Analytical Techniques

⇒	SEM	Scanning Electron Microscope	1 - 30 keV + EDX	*Hitachi, JP*
⇒	TEM	Transmission Electron Microscope (Titan 80-300 with Image Corrector)	80 - 300 keV + EDX, +GIF	*FEI, NL*
⇒	AES	Auger Electron Spectroscopy	+ XPS	*Fisions, GB*
⇒	CEMS	Mössbauer Spectroscopy	^{57}Fe source	*Home-built*
⇒	PAS	Positron Annihilation Spectroscopy	^{22}Na source 30 V - 36 kV	*Home-built*

4. Photon Based Analytical Techniques

⇒	XRD/XRR	X-Ray Diffraction and Reflection	Cu-K_α	*Bruker axs, DE*
	HR-XRD	High-Resolution XRD	Cu-K_α	*GE Inspection, DE*
	XRD/XRR	with Synchrotron Radiation	5 – 35 keV	*ROBL at ESRF, FR*
⇒	SE	Spectroscopic Ellipsometry	250 - 1700 nm	*Woolam, USA*
⇒	FTIR	Fourier-Transform Infrared Spectr.	600 - 7000 cm^{-1}	*Nicolet, USA*
⇒	FTIR	Fourier-Transform Infrared Spectr.	50 - 15000 cm^{-1}	*Bruker, DE*
⇒		Ti:Sapphire Femtosecond Laser		*Spectra Physics, USA*
⇒		Femtosecond Optical Parametric Oscillator		*APE, DE*
⇒		Ti:Sapphire Femtosecond Amplifier		*Femtolasers, AT*
⇒		Femtosecond Optical Parametric Amplifier		*Light Conversion, LT*
⇒	Raman	Raman Spectroscopy	45 cm^{-1} shift	*Jobin-Yvon-Horiba, FR*
⇒	PL	Photoluminescence	300 - 1500 nm	*Jobin-Yvon-Horiba, FR*
⇒	TRPL	Time-Resolved PL	τ = 3 ps - 2 ns	*Hamamatsu Phot., JP*
			τ > 5 ns	*Stanford Research, USA*
⇒	EL	Electroluminescence (10-300 K)	300 - 1500 nm	*Jobin-Yvon-Horiba, FR*
		Optical Split-Coil Supercond. Magnet	7 T	*Oxford Instrum., GB*
⇒	PR	Photomodulated Reflectivity	300 - 1500 nm	*Jobin-Yvon-Horiba, FR*
⇒	PLE	Photoluminescence Excitation	300 - 1500 nm	*Jobin-Yvon-Horiba, FR*

5. Magnetic Thin Film Deposition and Properties Analysis

⇒	MBE	Molecular Beam Epitaxy with in-situ FIB		*CreaTec,DE*
⇒	MBE	Molecular Beam Epitaxy		*Home-built*
⇒	MFM	Magnetic Force Microscope	~ 50 nm resol.	*VEECO / DI, USA*
⇒	SQUID	Supercond. Quantum Interf. Device	± 7 T	*Quantum Design, USA*
⇒	MOKE	Magneto-Optic Kerr Effect (in-plane)	± 0.35 T	*Home-built*
⇒	MOKE	Magneto-Optic Kerr Effect (perp.)	± 2 T	*Home-built*
⇒	SKM	Scanning Kerr Microscope		*Home-built*
⇒	TR-MOKE	Time-Resolved MOKE (Pump-Probe)		*Home-built*

⇒	VNA-FMR Vector Network Analyzer Ferromagnetic Resonance		*Agilent / Home-built*

6. Other Analytical and Measuring Techniques

⇒	Scanning Tunneling Microscope (with AFM-option)		*DME, DK*
⇒	Atomic Force Microscope (tapping mode)		*SIS, DE*
⇒	Atomic Force Microscope (with c-AFM, SCM-module)		*Veeco Instruments, GB*
⇒	In-situ Scanning Tunneling Microscope (variable-Temp.)		*Omicron, DE*
⇒	Dektak Surface Profilometer		*Veeco, USA*
⇒	Micro Indenter / Scratch Tester		*Shimatsu, JP*
⇒	Wear Tester (pin-on disc)		*Home-built*
⇒	Spreading Resistance Profiling		*Sentech, DE*
⇒	Hall Effect Equipment	(2 - 400 K, ≤ 9 T)	*LakeShore, USA*
⇒	DLTS (+ I-U / C-V)	(10 - 300 K, 1 MHz)	*PhysTech, DE*
⇒	I-V and C-V Analyzer		*Keithley, USA*
⇒	I-V and C-V Semi-Automatic Prober	(-60 - 300°C)	*Keithley, USA* *Süss, DE*

7. Processing and Preparation Techniques

⇒	Etching / Cleaning	incl. Anisotropic Selective KOH Etching	
⇒	Photolithography	Mask-aligner, 2 µm-level	*Süss, DE*
⇒	Thermal Treatment	Room Temperature - 2000°C	
		• Furnace	*InnoTherm, DE*
		• Rapid Thermal Annealing	*ADDAX, FR*
		• Flash-Lamp Unit (0.5 – 20 ms)	*Home-built; FHR, DE*
		• RF Heating (Vacuum)	*JIP.ELEC, FR*
⇒	Physical Deposition	Sputtering DC / RF, Evaporation	*Nordiko, GB*
		Electron Beam Evaporation System	*Leybold Optics, DE*
⇒		Thermal Evaporation	*Bal-Tec, FL*
⇒	Dry Etching	Plasma and RIE Mode	*Sentech, DE*
⇒	Bonding Techniques	Ultrasonic Wire Bonding	*Kulicke&Soffa, USA*
⇒	Cutting, Grinding, Polishing		*Bühler, DE*
⇒	TEM Sample Preparation	Plan View and Cross Section	
		incl. Ion Milling Equipment	*Gatan, USA*

Services

The institute serves as a user center and technology transfer point in connection with its many years of experience in the application of ion beams for modification and analysis of solid surfaces and thin films of arbitrary materials.

Ion beam treatment of metallic materials (e.g. light metals like Al, Ti; stainless steel) can be advantageously applied for the improvement of the tribological properties (hardness, wear, corrosion resistance etc.). Using ion beam assisted deposition, hard coatings with special properties are obtained, such as a high adhesive strength and low internal stress. New technologies of high energy ion implantation or focused ion beam techniques result in new applications of electronic devices or microintegrated circuits.

Ion beams are an excellent instrument for the analysis of solid state surfaces. The interaction of the incident ion beam with the surface layer of a material leads to a specific radiation response, which yields information on the elemental composition as function of depth in a quantitative and essentially non-destructive way.

Additional means of preparation and diagnostics are available to fulfill the needs of users from different industrial branches. Do not hesitate to contact our experienced team.

Main Areas of Competence:

- Development and fabrication of sensors and detectors for charged particle spectroscopy
- Deposition of functional coatings using ion-assisted physical vapor deposition
- Fabrication of wear protection layers on metallic materials or alloys
- Deposition of blood compatible layers (i.e. TiO_x) on different materials
- Ion implantation in a broad range of ion energy (~ 200 eV to ~ 50 MeV) and substrate temperature
- Advanced ion beam technologies (high energy ion implantation, focused ion beam) for microelectronic applications
- Application of high energy ion implantation for power devices and laser structures
- Doping of semiconductors, in particular wide bandgap semiconductors
- Surface analysis of solid materials with high energy ion beams
- Computer simulation of ion beam interaction with materials
- Optical characterization of materials (luminescence, FTIR, Raman)

Offers:

- Consultation and problem evaluation for ion beam applications
- Process development for ion beam treatment of different materials (metals, ceramics, semiconductors)
- Process development in ion-assisted deposition of thin films
- Preparation and treatment of material samples, tools or complex parts of devices
- Ion implantation and ion beam analysis services
- Ion implantation into semiconductor materials for applications in microsystems and micro- and power electronics,
- Preparation / fabrication of semiconductors or silicon radiation sensors under clean room conditions
- Structural diagnostics of materials surfaces including e-beam- (SEM, TEM, AES) and X-ray techniques (XRD, XRR with both Cu-K and Synchrotron (5-35 keV) radiation).

Examples:

- Improvement of wear resistance of austenitic stainless steels using plasma immersion ion implantation
- High energy ion implantation for power semiconductor devices,
- Micro- and nano-engineering with focused ion beams
- Non-destructive quantitative hydrogen analysis in materials
- Non-destructive ion beam analysis of art objects

- Doping of wide-bandgap-semiconductors (SiC, diamond)
- Nuclear microprobe for ion beam analysis with high spatial resolution
- Synchrotron radiation analysis of materials at the ROBL Beamline in Grenoble.

Contact:

Please direct your inquiry about the application of ion beams for modification and analysis of materials to one of the following experts:

Field of application	Name	Phone / Fax	E-mail
Ion implantation (metals, ceramics, polymers, biomaterials)	Dr. Andreas Kolitsch	3348 / 2703	a.kolitsch@fzd.de
Ion implantation (semiconductors, in particular high energy)	Dr. Johannes von Borany	3378 / 3438	j.v.borany@fzd.de
Thin film deposition	Dr. Andreas Kolitsch	3348 / 2703	a.kolitsch@fzd.de
High energy ion beam analysis	Dr. Rainer Grötzschel	3294 / 2870	r.groetzschel@fzd.de
Semiconductor preparation Detector / Sensor fabrication	Dr. Bernd Schmidt	2726 / 3285	bernd.schmidt@fzd.de
Focused ion beams	Dr. Lothar Bischoff	2963 / 3285	l.bischoff@fzd.de
Structural diagnostics	Dr. Johannes von Borany	3378 / 3438	j.v.borany@fzd.de
Materials research with Synchrotron radiation at ROBL (ESRF)	Dr. Carsten Bähtz	2367	baehtz@esrf.fr
Optical materials characterization	Dr. Harald Schneider	2880 / 3285	h.schneider@fzd.de

For all phone/ fax-numbers choose the country / local code: +49 351 260 - xxxx (for FZD)
+33 47 688 - xxxx (for ROBL)

The institute also recommends the homepages of its spin-off companies

- "GeSiM mbH" www.gesim.de
- "APT Dresden" www.apt-dresden.de
- "IONServices" www.ions.de

Forschungszentrum Dresden - Rossendorf e.V.

Institute of Ion Beam Physics and Materials Research (IIM)

Postfach 51 01 19
D-01314 Dresden

Tel.: 0351 260 2245
Fax: 0351 260 3285
http://www.fzd.de/FWI

DIRECTORS

Prof. Dr. Wolfhard Möller 2245

Prof. Dr. Manfred Helm 2260

DIVISIONS

ION TECHNOLOGY (FWII)
Dr. Andreas Kolitsch / 3326

- MeV accelerators
- Ion Implanter / PIII operation
- Ion Beam and Plasma Assisted Deposition
- Biotechnological Materials
- Industrial Services and Projects

SEMICONDUCTOR MATERIALS (FWIM)
Dr. Wolfgang Skorupa / 3612

- Semiconductors
- Optoelectronic Applications
- Rapid Thermal Annealing Processes
- Defect Engineering
- Positron Annihilation Spectroscopy

NANOFUNCTIONAL FILMS (FWIN)
Dr. Jürgen Fassbender / 3096

- Modification of Magnetic Materials
- High Anisotropy Nanoparticles
- Magnetic Semiconductors / Spintronics
- Magnetization Dynamics
- Fullerene-like Materials

SEMICONDUCTOR SPECTROSCOPY (FWIH)
Dr. Harald Schneider / 2880

- Semiconductor Quantum Structures
- Terahertz Spectroscopy
- Femtosecond Spectroscopy
- Free Electron Laser at ELBE
- Optical Characterization (PL, FTIR, Raman)

ION BEAM ANALYSIS (FWIA)
Dr. Rainer Grötzschel / 3294

- Ion-Solid-Interaction
- High-Energy Ion Beam Analysis
- Channeling Studies of Crystal Defects
- Non-destructive Analysis of Art Objects
- Composition / Modification of Materials

STRUCTURAL DIAGNOSTICS (FWIS)
Dr. Johannes von Borany / 3378

- Electron Microscopy (TEM, SEM)
- Electron Spectroscopy (AES, XPS)
- Mössbauer Spectroscopy
- X-ray Analysis
- Materials Research with Synchr. Radiation

THEORY (FWIT)
Dr. Matthias Posselt / 3279

- Ion-Beam Synthesis of Nanostructures
- Formation and Evolution of Defects
- Atomistic Simulation of Ion implantation and Ion-Assisted Deposition
- Interatomic Potentials for Solids
- Reaction-Diffusion-Models

PROCESS TECHNOLOGY (FWIP)
Dr. Bernd Schmidt / 2726

- Semiconductor Technology
- Focused Ion Beam Technology
- Thin Film Deposition
- Computer Aided Structure Design
- Electrical Characterization
- Clean Room Operation

List of Personnel 2007

Directors: Prof. M. Helm, Prof. W. Möller

Scientific Staff:

Permanent:

Dr. G. Abrasonis
Dr. C. Akhmadaliev
Dr. C. Bähtz
Dr. L. Bischoff
Dr. J. von Borany
Dr. W. Bürger
Dr. S. Facsko
Dr. J. Faßbender
Dr. M. Friedrich
Dr. S. Gemming
Dr. D. Grambole
Dr. J. Grenzer
Dr. R. Grötzschel
Dr. V. Heera
F. Herrmann
Dr. K.-H. Heinig
Dr. R. Kögler
Dr. A. Kolitsch
Dr. U. Kreißig
Dr. A. Mücklich
Dr. F. Munnik
Dr. C. Neelmeijer
Dr. M. Posselt
Dr. K. Potzger
Dr. L. Rebohle
Dr. H. Reuther
Dr. A. Rogozin
Dr. B. Schmidt
Dr. H. Schneider
Dr. W. Skorupa
Dr. D. Stehr
Dr. M. Voelskow
Dr. S. Winnerl

Post Docs:

Dr. N. Jeutter
Dr. K. Küpper
Dr. M. O. Liedke
Dr. Z. Pesic
Dr. M. Vinnichenko

Projects:

Dr. B. Abendroth
W. Anwand
Dr. G. Brauer
Dr. O. Drachenko
Dr. C. V.-B. Grimm
Dr. A. Kanjilal
Dr. M. Krause
R.S.M. Martins
V. Pankoke
Dr. W. Pilz
Dr. H. Schmidt
Dr. A. Shalimov
Dr. N. Shevchenko
Dr. H. Weishart
Dr. Q. Xu
Dr. R. Yankov
Dr. M. Zier
M. Zschintsch

PhD Students:

M. Berndt
V. Beyer
V. Cantelli
R. Cheng
C. Cherkouk
A. Dreyhaupt
H. Geßner
D. Güttler
A. Hanisch
R. Heller
R. Jacob
A. Keller
M. Kosmata
B. Liedke
R. Mukesh
D. Markó
A. Martinavicius
S. Ohser
X. Ou
H. Peng
F. Peter

Office: I. Heidel, S. Kirch, L. Post

J. Potfajova
H. G. von Ribbeck
L. Röntzsch
C. Scarlat
M. Schmidt
T. Schucknecht
T. Strache
G. Talut
M. Thieme
M. Wagner
C. Wündisch
J. Zhou
S. Zhou

Diploma Students:

C. Baumgart
D. Bürger
S. Cornelius
M. Fritsche
A.-A. Gabriel
O. Kallauch
M. Körner
T. Kunze
D. Nauert
C. Pfau
S. Schreiber
M. Sellesk
A. Silze
S. Wintz
B. Zimmermann

Technical Staff:

Permanent:

Rb. Aniol
Ry. Aniol
G. Anwand
E. Christalle
H. Felsmann
K. Fukarek
B. Gebauer
H.-J. Grahl
D. Hanf
P. Hartmann
J. Haufe
A. Henschke
G. Hofmann
S. Klare
J. Kreher
A. Kunz
H. Lange
U. Lucchesi
F. Ludewig
R. Mester
M. Mißbach
C. Neisser
S. Probst
E. Quaritsch
A. Reichel
M. Roch
B. Scheumann
G. Schnabel
A. Schneider
J. Schneider
A. Scholz
T. Schumann
U. Strauch
K. Thiemig
A. Vetter
R. Weidauer
A. Weise
J. Winkelmann
G. Winkler
I. Winkler
L. Zimmermann
J. Zscharschuch

Projects:

S. Eisenwinder
M. Steinert
I. Skorupa